THE UNIVERSITY OF OKLAHOMA

GRADUATE COLLEGE

TURBULENT BOUNDARY LAYER CHARACTERISTICS OF FLOW OVER A COMPLIANT SURFACE

A DISSERTATION

SUBMITTED TO THE GRADUATE COLLEGE

in partial fulfillment of the requirements for the

degree of

DOCTOR OF PHILOSOPHY

BY

ROBERT R. RAYMOND WALTERS

Norman, Oklahoma

1969

TURBULENT BOUNDARY LAYER CHARACTERISTICS OF FLOW

OVER A COMPLIANT SURFACE

APPROVED BY

E. A. Blick

Raymond Kaser

William N. Hughes

C. W. Bert

D. M. Egle

DISSERTATION COMMITTEE

ACKNOWLEDGMENTS

The work reported herein is part of a project supported by funds from the U.S. Army (ARO-D Project No. 5596-E) under Grant No. DA-31-124-ARO-D-349.

The financial assistance of the National Science Foundation in the form of a graduate traineeship is gratefully recognized.

The author would like to express his gratitude to Dr. E.F. Blick for his guidance during this study and throughout the graduate program. His inspiration and encouragement have been most appreciated. Also, the time and effort of Dr. C.W. Bert, Dr. D.M. Egle, Dr. R.V Kaser, and Dr. W.N. Huff have been sincerely appreciated by the author.

The author is deeply grateful to his family for their role during the years of formal study.

To my wife, Carol, I dedicate this work that she has been so much a part of.

ABSTRACT

A detailed hot-wire anemometer study was made to determine the basic characteristics of the turbulent boundary layer flow with a zero pressure gradient over a compliant surface. The compliant surface was constructed from a 0.001 inch polyvinyl-chloride (PVC) membrane backed by a 3/16 inch damping layer of polyurethane foam (40 P.P.I). The foam was bonded to a 14 foot x 2 foot test plate positioned horizontally in the center of a 2 foot wide, 15 foot 8 inch long test section of a low-turbulence wind tunnel constructed for this investigation. The membrane was stretched across the foam and clamped at the edges. Boundary layer thickening was achieved by bonding a two-foot length of No. 16 sand-paper to the leading edge of the test plate. The tests were run at a constant velocity of 50 fps. The hot-wire anemometer study over the compliant surface revealed little change in the velocity profile, but a reduction of turbulence intensities was recorded, as well as a 25 per cent decrease in the Reynolds stresses, when compared with hard plate data. The spectra of turbulence measurements indicated a decrease in energy at the higher frequencies throughout the boundary layer. As the wall was approached an increase in energy at the low frequencies was measured. Production, dissipation, and convection of turbulent energy were found to decrease over the compliant surface when compared with the hard plate measurements.

TABLE OF CONTENTS

LIST OF TABLES

LIST OF ILLUSTRATIONS

Figure

Page

NOMENCLATURE

The following nomenclature is used throughout this work unless noted otherwise.

A	$1/\kappa$
B	$-(1/\kappa)\ \ln\ \beta$
B.L.D.	boundary layer development
C	capacitance
C'	hot-wire cooling velocity
C_1	$-[(4\delta/5U_1^2X_o)_o\int^{y/\delta}(U/U_1)d(y/\delta)]\frac{d}{d(y/\delta)}\ (\frac{\overline{u^2}+\overline{v^2}+\overline{w^2}}{2})$
c_f	coefficient of skin friction $\tau_o/1/2\rho U_1^2$
e_c	voltage drop across capacitor
e_i	differentiation-circuit input voltage
e_o	differentiation-circuit output voltage
e_R	voltage drop across resistor
f	frequency
$F_u(k_1)$	percent of turbulent energy $\overline{u^2}$ associated with k_1
$f_u(k_1)$	turbulent energy $\overline{u^2}$ associated with k_1
K	sensitivity of wire A and B when $K_A = K_B$
K_A	sensitivity of wire A
K_B	sensitivity of wire B
K_G	amplifier gain factor
K_s	sum and difference unit amplification factor

K_v	rms voltmeter calibration constant
k_1	one-dimensional wave number
M_A	rms voltage of signal from wire A
M_B	rms voltage of signal from wire B
M_{A+B}	rms voltage of sum of signals from wires A and B
M_{A-B}	rms voltage of difference of signals from wires A and B
M_N	rms voltage of amplifier noise signal
P(u/u')	probability density of u/u'
P.P.I.	pores per inch
P_r	production of turbulent energy $\approx (\delta\overline{uv}/U_1^3)(dU/dy)$
p	mean static pressure
$p_{10.5}$	mean static pressure at X = 10.5 feet
$\overline{q^2}$	time mean value of twice energy of turbulence $= \overline{u^2} + \overline{v^2} + \overline{w^2}$
R_e	Reynolds number $[R_e = (U_1 X_0)/\nu]$
R_x	longitudinal space correlation coefficient of u-fluctuation
t	time
T	temperature
U	x-component of mean velocity
U_τ	shear velocity $= \sqrt{\tau_0/\rho}$
U^*	U/U_τ
U_1	mean velocity in free stream
u, v, w	instantaneous turbulent velocity fluctuations in x, y and z directions, respectively
u', v', w'	root mean square values $\sqrt{\overline{u^2}}$, $\sqrt{\overline{v^2}}$ and $\sqrt{\overline{w^2}}$, respectively
$\overline{u^2}$, $\overline{v^2}$, $\overline{w^2}$	mean square values of u, v, and w

$-\overline{\rho uv}$	turbulent shearing stress
V	y-component of mean velocity
W_μ	$(\delta\nu/U_1^3)(dU/dy)$
W_1	$(\delta\nu/U_1^3)[d^2(\overline{u^2} + \overline{v^2} + \overline{w^2}/2)dy\ ]$
W_2'	$(\delta\nu/U_1^3)[\overline{(\partial u/\partial x)^2} + \overline{(\partial v/\partial x)^2} + \overline{(\partial w/\partial x)^2} + \overline{(\partial u/\partial y)^2} + \overline{(\partial u/\partial z)^2}]$
W_2	$(\delta\nu/U_1^3)[\overline{(\partial u/\partial x)^2} + \overline{(\partial v/\partial x)^2} + \overline{(\partial w/\partial x)^2} + \overline{(\partial u/\partial y)^2} + \overline{(\partial u/\partial z)^2} + \overline{(\partial v/\partial y)^2} + \overline{(\partial v/\partial z)^2} + \overline{(\partial w/\partial y)^2} + \overline{(\partial w/\partial z)^2}]$
X	distance along surface of B.L.D. plate from leading edge
X_o	distance along surface of B.L.D. plate from the virtual origin
x	distance from X = 10.5 ft. in direction of flow
x, y, z	Cartesian coordinate system originating at center of tunnel width on B.L.D. plate surface at X = 10.5 ft.
$\Delta x, \Delta y, \Delta z$	intervals in x, y, and z directions, respectively
y	distance normal to surface measured from surface
y^*	$y\ U_\tau/\nu$
z	direction perpendicular to xy plane
κ	empirical constant
δ	boundary layer thickness
ν	kinematic viscosity
ρ	density of air
τ	hot-wire time constant
τ_o	shearing stress at wall
$\overline{(\ )}$	mean value
$U_{A,t}$	$\partial U_A/\partial t$

TURBULENT BOUNDARY LAYER CHARACTERISTICS OF FLOW OVER A COMPLIANT SURFACE

CHAPTER I

INTRODUCTION

In the continuing quest for an effective means of reducing drag on aerodynamic and hydrodynamic bodies, many techniques have been explored. Interest in the technique of utilizing a compliant wall on bodies, i.e., ships and aircraft, was originally generated from the promising experiments of Kramer in 1955 [1 and 2]. Tests on his compliant wall models, designed from observations of dolphins [3], revealed impressive drag reductions of more than 50%.

Benjamin [4], Hains [5], Landahl [6] and Kaplan [7] undertook theoretical analyses of the compliant wall phenomenon. Their work indicated that laminar and low disturbance flow could be stabilized by the presence of an ideally designed compliant boundary.

Experiments under the direction of Laufer and Maestrello [8] on turbulent air flow in channels with flexible walls were inconclusive. They utilized thin aluminum, steel, mylar, and rubberized textile fabric, backed by a variety of different types of rubber for a combination of test specimens. Further work was undertaken by Ritter [9], who measured a 7 to 14 percent drag reduction on compliant coatings, but the scatter of the data was so large that the results have been considered question-

able. Dinkelacker, at the University of Southampton, as reported by Benjamin [9], found no significant skin friction reduction in his experiments on water channels with flexible walls. Smith [10], working with water flow through circular pipes with annular coatings of elastic gell, could find no reduction in skin friction. Gregory and Love [11] conducted several tests on foam sandwich-type structures with thin aluminum or rubber coatings attached to the surface of an airfoil. Their results were inconclusive with regard to skin friction reduction.

Karplus [12], investigating the scale and degree of turbulence for water flow over mylar film with various fluid substrates, measured a slight drop in the amplitude of the fully developed turbulence in the boundary layer for flexible walls as compared to rigid walls. He concluded that turbulence occurred sooner for the flexible wall than for the solid wall but was retarded in its rate of development.

Pelt [13] obtained more promising results in his measurements of pressure drops through lined pipes. He recorded a 32 to 35 percent reduction in pressure drop using polyester-based urethane resin ("Texin" tubes) as pipe liners backed by a damping medium. Von Winkel and Barger [14] found a considerable reduction in intensity of surface pressure fluctuations with a Kramer type compliant skin.

Experiments conducted at the University of Oklahoma have proven to be most promising for substantiating the basic ideas of Kramer. Results published by Fisher and Blick [15], Looney and Blick [16] and Walters and Blick [17] have indicated a significant drop in the amplitube of the turbulence level and an associated reduction of the skin friction coefficient. Turbulent flow over a polyvinyl-chloride (PVC)

membrane with a variety of damping fluid substrates was studied. For certain combinations of streamwise and transverse skin tensions and viscosity of damping fluid, Walters and Looney reported a 20 percent reduction in turbulence intensity and a 45 to 50 percent reduction in skin friction, respectively.

Along with the decrease in turbulence level reported in reference [17] and detailed by the author [18], a decrease in the boundary layer shear stress was measured. From a plot of this Reynolds stress versus y/δ, an extrapolated value for the skin friction coefficient on hard plate and also for compliant plate was calculated by the method utilized by Laufer [19]. These skin friction coefficients coincided extremely well with those directly measured by Looney.

These basic experiments did give credence to the results of theoretical investigators that the compliant wall could indeed influence the boundary layer stability. The mechanism by which the compliant boundary induces the apparent increase in stability and decrease in Reynolds stress is far from being completely understood. However, a recent paper by Blick [20] has developed a theory which explains how a compliant coating can reduce the Reynolds stress in a turbulent boundary layer.

Most of the reported theoretical analyses (i.e. references 4 to 7), have dealt with the problem of laminar boundary layers exposed to compliant walls. This is a logical approach, to gain insight into the less complex, mathematically feasible problem. Gyorgyfalvy [21] has approached the problem by a theoretical analysis of amplification rates and delayed transition with compliant walls, much like Kaplan's initial

work. Gyorgyfalvy listed desirable membrane properties and Reynolds numbers.

This previous work gives some of the basic parameters that might be used in approaching the fully turbulent boundary layer problem over compliant surfaces. However, it is essential first to become aware of the methods of approach to the rigid wall case. Since turbulence by its nature is complex, it would be advantageous to work with the simplest case, that of homogeneous, isotropic turbulence, with zero mean rate of shear. This type of turbulence, which can be described mathematically by probability distributions of velocity fluctuations, has provided some insight into the mechanism of turbulent interactions and prediction of turbulence characteristics. Nevertheless, this statistical approach has made little progress in the area of turbulent shear flow. Therefore, more of the work in the turbulent shear flow area has dealt with advancing the empirical-phenomenological theories. This work has evolved into exhaustive experimental measurements of the turbulent boundary layer characteristics, such as Klebanoff's work [22], and various attempts to visualize turbulence.

One of the best recent attempts to attain a physical interpretation of the mechanism of turbulence has been by Runstadler, Kline, and Reynolds [23]. Their "wall layer hypothesis", can be stated as follows: "The wall layer structure and its interaction with the outer flow plays a dominant role in creating and maintaining the structure of the entire turbulent shear layer." Using a water channel system that included a hot-film anemometer and an elaborate photographic arrangement, they were able to give the following supporting evidence for their hypothesis:

> The dominant mechanism for the transport of turbulence to the outer regions of the flow is through the outwards and downstream convection of small scale turbulence within larger scale eddies which originate near the wall following the break-up of wall layer streaks. The flow in the outer layers is thus proposed to be an integrated or history effect of flow arriving in these layers from upstream. In and near the wall layers, we suppose the flow is primarily determined by the local character of low and high speed streaks, break-ups and ejections, and turbulent interactions. Further from the wall, we conjecture that the flow is governed to a greater and greater extent by upstream wall conditions through the history effect of advected turbulent eddies. In a sense, then, the entire boundary layer flow structure is speculated to be the result of the formation and ejection of eddies from the wall layer. The slow return flow of fluid to the wall we visualize as driven by instantaneous pressure forces resulting from dynamic interactions between eddies and is part of the process by which energy is extracted from the mean flow. This return flow of high momentum fluid supplies energy to the wall layers; the energy there is dissipated into internal thermal energy by the strong viscous forces, with the resultant formation of momentum deficient fluid which apparently takes the form of streaks. We envisage that the ejection of low momentum streaks away from the wall layers results in a strong interaction and production of turbulent energy immediately outside the wall layer and the continued movement of the streaks away from the wall provides a continuous interaction process for the production of finer scaled turbulence within the large scaled eddies. This then becomes the mechanism for the diffusion of turbulence into the outer flow and the net transfer of turbulent energy from the larger scales to the smaller scales of the turbulent motion and eventually to internal thermal energy of the fluid through viscous dissipation. (reference [23], pp. 88-89)

The purpose of this paper is to investigate the characteristics of the turbulent boundary layer exposed to the compliant surface, using the work of Klebanoff [22], Townsend [24] and Runstadler, et al. [23] as a guideline.

Since it was not possible to consider the characteristics of boundary layer turbulence in total, this investigation was concerned primarily with: (1) construction of a system with flow characteristics over a rigid plate similar to previous work [22] for comparison to the compliant plate, (2) obtaining quantitative measurements pertinent to the

energy balance and (3) delineating differences in the spectral distribution of turbulent energy over compliant plate and hard plate. Klebanoff's hard plate work was selected for comparison due to the available laboratory potential.

CHAPTER II

WIND TUNNEL TEST FACILITY

The turbulence investigations recorded in later chapters of this text were conducted at the University of Oklahoma, in the Aerospace and Mechanical Engineering Laboratory. A wind tunnel was constructed primarily for the present investigations, due to the lack of a tunnel with the specific requirements.

Preliminary Tunnel Requirements

In the summer of 1967, initial design and construction were started on a wind tunnel which met these specifications. The initial requirements, formulated to insure proper turbulence investigations and duplication of previous hard plate work, [22], are as follows:

1. Low turbulence in main stream of test section.
2. Fully developed turbulent boundary at beginning of compliant test plate area (X = 9.4 ft.) with a minimum boundary layer thickness of two inches at that point.
3. Zero pressure gradient condition throughout tunnel test section.
4. Sufficiently wide compliant test plate in order to neglect edge effects.
5. Test section height small enough to enable hot-wire anemo-

meter probe to extend to test section floor, that is, the compliant test plate surface.

6. Very small gap around free test plate.
7. Enclosure around test plate support (possible provision for strain gage bar) to stop airflow through gap.
8. Series of pressure taps along tunnel floor or wall to monitor pressure gradient.
9. Double layer ceiling - one for blister effect and one for support and sealing hot-wire probe.
10. Entrance of test section and leading edge of the boundary layer development plate such that a natural transition to a turbulent boundary layer occurs.
11. Ability to remove tunnel from compliant test plate or vice versa. Need leveling screws on tunnel and test plate support.
12. Sufficient access to any point within upper test section region.

After several preliminary designs were completed, a design was selected and developed so that construction could be initiated. The completed design is shown in Fig. 2.1.

The design can be substantiated by enumerating the means incorporated to fulfill the listed requirements.

Main Tunnel Test Section

To satisfy the second requirement, that a fully developed boundary layer exist at the beginning of the flush, inserted test plate

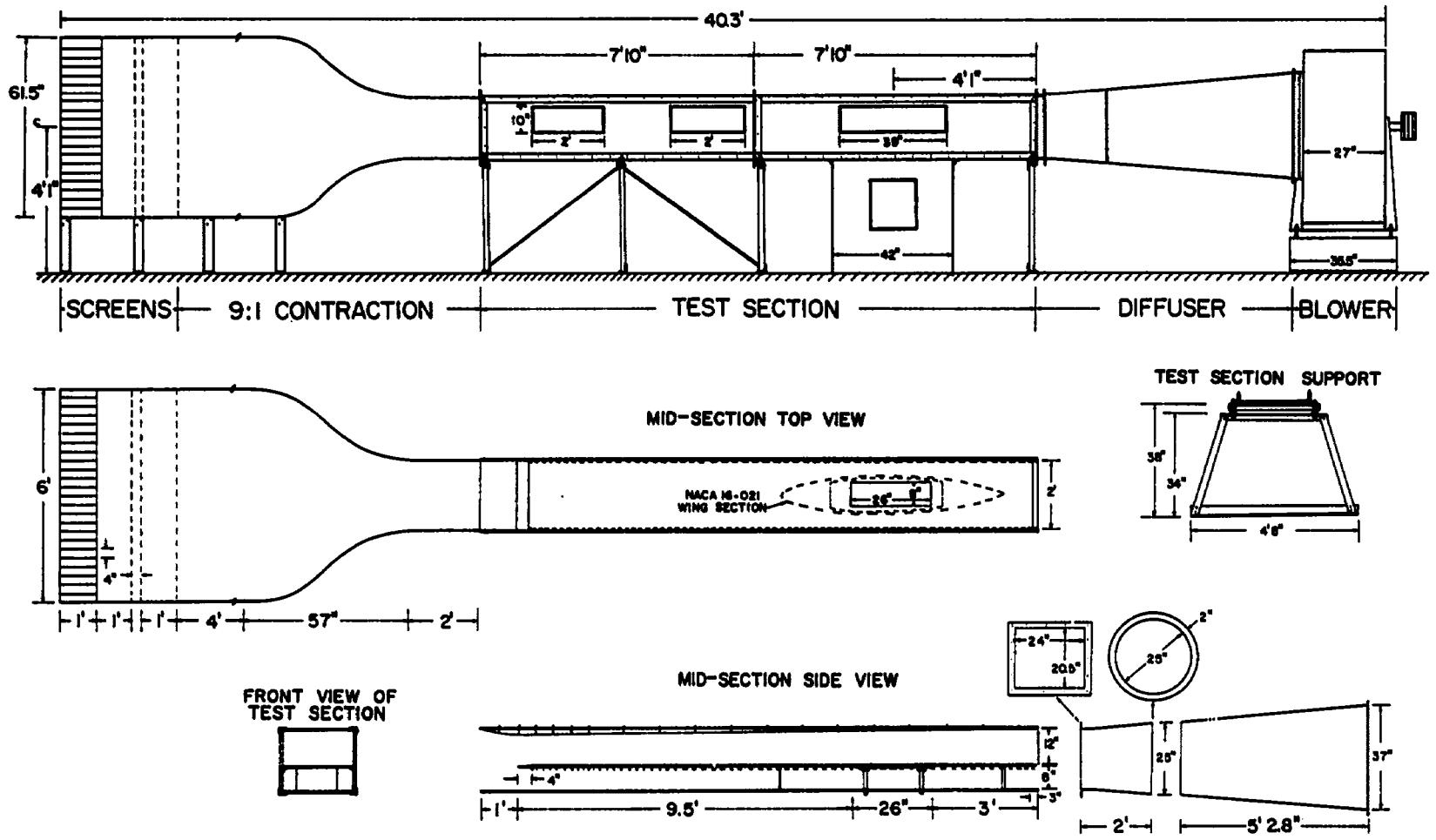

Figure 2.1. Schematic of the wind tunnel.

with a large boundary layer thickness (approximately two inches thick), a long test section was needed. After looking at Klebanoff's work, [22], a smooth, flat plate, fourteen and one half feet (14.5 ft.) long, one half inch thick and 24 inches wide, was selected. On the first 4.5 inches of the flat plate was bonded an aluminum, symmetrically tapered leading edge. The last two inches of the flat plate were tapered to minimize the size of the wake that would enter the diffuser section.

The plate was mounted 12 inches from the top of the tunnel test section, which had cross-sectional dimensions of 20.5 inches high and 24 inches wide. The cross-sectional dimensions of the test section were developed from the fifth and tenth requirements. That is, the compliant test plate, which was flush with the boundary layer development (B.L.D.) plate, should not be more than 12 inches* from the top of the test section. The 8-inch dimension between the B.L.D. plate and the floor of the test section was thought to be adequate to insure that the leading edge of the boundary layer plate would be exposed to an undisturbed flow. The consequent 8-inch x 24-inch area was sufficient to provide equal flow velocity on either side of the leading edge of the B.L.D. plate. This height between the B.L.D. plate and the test section floor was limited by the necessity of inserting the compliant test plate and support through the test section floor until flush with the upper surface of the B.L.D. plate at the 10.5 foot mark. The leading edge of

---

*Determined from available length of hot-wire anemometer probe after insertion in probe holder.

the B.L.D. plate was placed one foot behind the test section entrance to assist in minimizing entrance effects.

Since desirable results were obtained with an 8 inch by 26 inch compliant test plate in previous work [18], the same dimensions were used. Since data measurements were to be made at the X=10.5 foot position as used by Klebanoff [22], the test plate was centered around this position in the B.L.D. plate. Therefore, a rectangular hole was cut in the B.L.D. floor. This rectangular hole was centered in the 24 inch width and extended from X = 9 feet 5 inches to X = 11 feet 7 inches, with a 1/16 inch gap on all sides (requirement number 6).

The main tunnel test section, 15 feet 8 inches long, was constructed of 5/8 inch interior fir plywood held by a frame of 2 inch x 2 inch (3/16 inch thick) steel angles. The frame was supported at four different stations by screw adjustments (requirement No. 11) attached to an A-frame structure anchored to the floor. This enabled the frame to be leveled before insertion of the plywood walls, which had been finished with a sanding lacquer finish and a plastic varnish. All interior walls and the B.L.D. plate were finished in this manner to give an aerodynamically smooth surface.

In order to satisfy the twelfth requirement an imaginary blackboard model was used to determine the most desirable tunnel access window positions and sizes. The resultant access windows were placed at the locations shown in Fig. 2.1. An access window was located on both sides of the compliant test plate area. The windows were constructed of 1/4 inch polymethymethacrylate("Plexiglas") with an aluminum frame and were sealed with 1/2 inch by 5/16 inch Johns-Manville weatherstrip-

ping. Adjustable sash fasteners were used to press the windows into position flush with the tunnel walls and to maintain a desirable air seal.

Test Section Pressure Gradient

In order to maintain a zero pressure gradient condition throughout the upper tunnel test section, as stated in the third requirement, a variable-area test section had to be obtained. This was accomplished by suspending a 1/8 inch thick, 24 inch wide and 16 foot long strip of pressboard from the top of the tunnel test section by means of screws to form a false adjustable ceiling. These screws were attached to the back side of the pressboard and inserted through holes in the top of the tunnel test section. A maximum point of curvature of the false ceiling was positioned at the leading edge of the B.L.D. plate. This was tapered off as X increased to approach asymptotically the top of the tunnel test section. This variation in area offset the decrease in effective flow area due to the boundary layer displacement thickness on all sides.

A series of 1/32 inch diameter holes were drilled midway in the side wall of the upper tunnel test section and also the lower tunnel test section for use as static pressure taps. These were spaced at one foot intervals, starting at the leading edge of the B.L.D. plate. Using Tygon tubing, these taps were connected to a board manometer for coarse readout and the Flow Corporation Model MM-3 micromanometer for fine readout (ten-thousandths of an inch of fluid). After tunnel completion, the false ceiling was adjusted until the pressure gradient, as shown below in Fig. 2.2, was obtained. The largest pressure difference was found to exist at X = 12 feet. At X = 7 feet, 9 feet, and 12 feet, small discontinuities of the tunnel wall existed which were thought to give erroneous

readings at these particular stations.

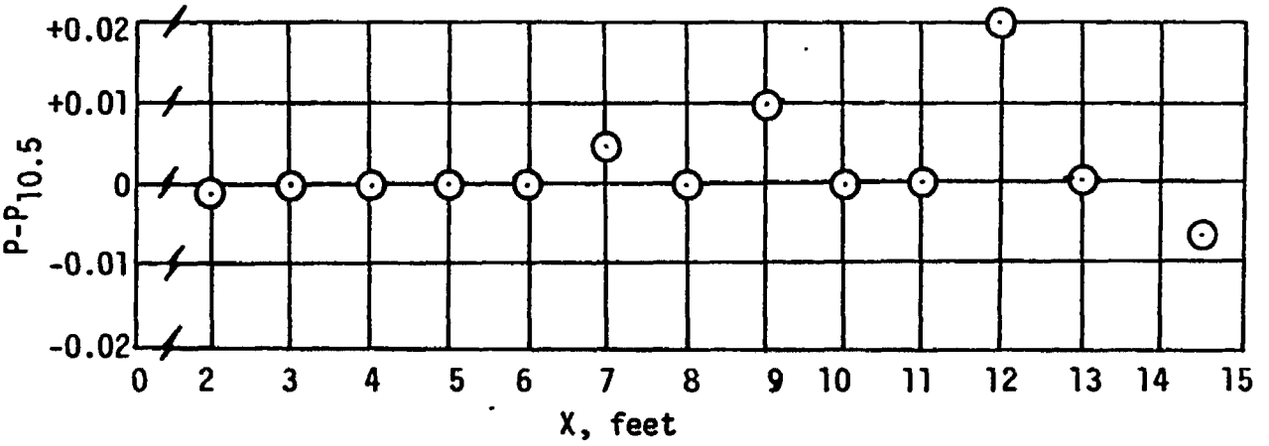

Figure 2.2. Pressure distribution along the flat plate.

At the X = 0 station, a pressure difference was found between the upper and lower pressure taps. A tuft survey indicated a choking condition in the lower flow. The pressure difference was later eliminated by the installation of a fiberglass screen in the upper flow at the trailing edge of the B.L.D. plate.

Sealing Test Plate Support

As found in previous experiments [18], and so stated as requirement number 7, flow through the gap around the test plate was eliminated by sealing the test plate support apparatus from the surrounding air. This was accomplished by means of a sealed plywood box built around a steel frame between the bottom of the wind tunnel and the floor of the test room. The front of the box was removable for access to the test plate support. Also in the removable section was installed a "Plexiglas" door for easy access to the test plate support.

A NASA 16-021 air foil was installed between the bottom of the B.L.D. plate and the test section floor to shield and seal the lower

flow from the test plate support apparatus, since the support extended through this particular region. The air foil had a chord length of 5 feet and a maximum thickness of 12.75 inches. The height of the airfoil was 8 inches. The airfoil was constructed from press board and finished with the plastic varnish, as was the false ceiling.

All of the joints, connections, and bolt holes were sealed with Dow Corning Silastic 892-RTV Adhesive sealant.

Entrance Section

An entrance section of the tunnel was designed to provide a minimum of turbulence in the test section main stream flow (requirement No. 1).

As stated by Pankhurst and Holder [25], the three principal methods used for reducing wind tunnel turbulence of an airstream are screens, a contraction, and honeycomb. All three methods were incorporated into the entrance section design.

After reviewing the work of Uberoi [26], who listed experimental data for 16:1, 9:1, and 4:1 contraction ratios, a 9:1 contraction was selected. The size of the contraction was also limited by available room at the wind tunnel location. From Uberoi's work, this particular contraction ratio gave a favorable decrease in the longitudinal component of turbulence without too large an increase in the lateral component. Also, the two-dimensional contraction was best suited for the rectangular test section geometry.

The contraction, as shown in Figs. 2.1 and 2.3, was fabricated from 1/8 inch x 4 feet x 12 feet pressboard held by a wooden frame built from 2 x 4 inch wood boards. A four foot long pre-contraction pre[illegible]

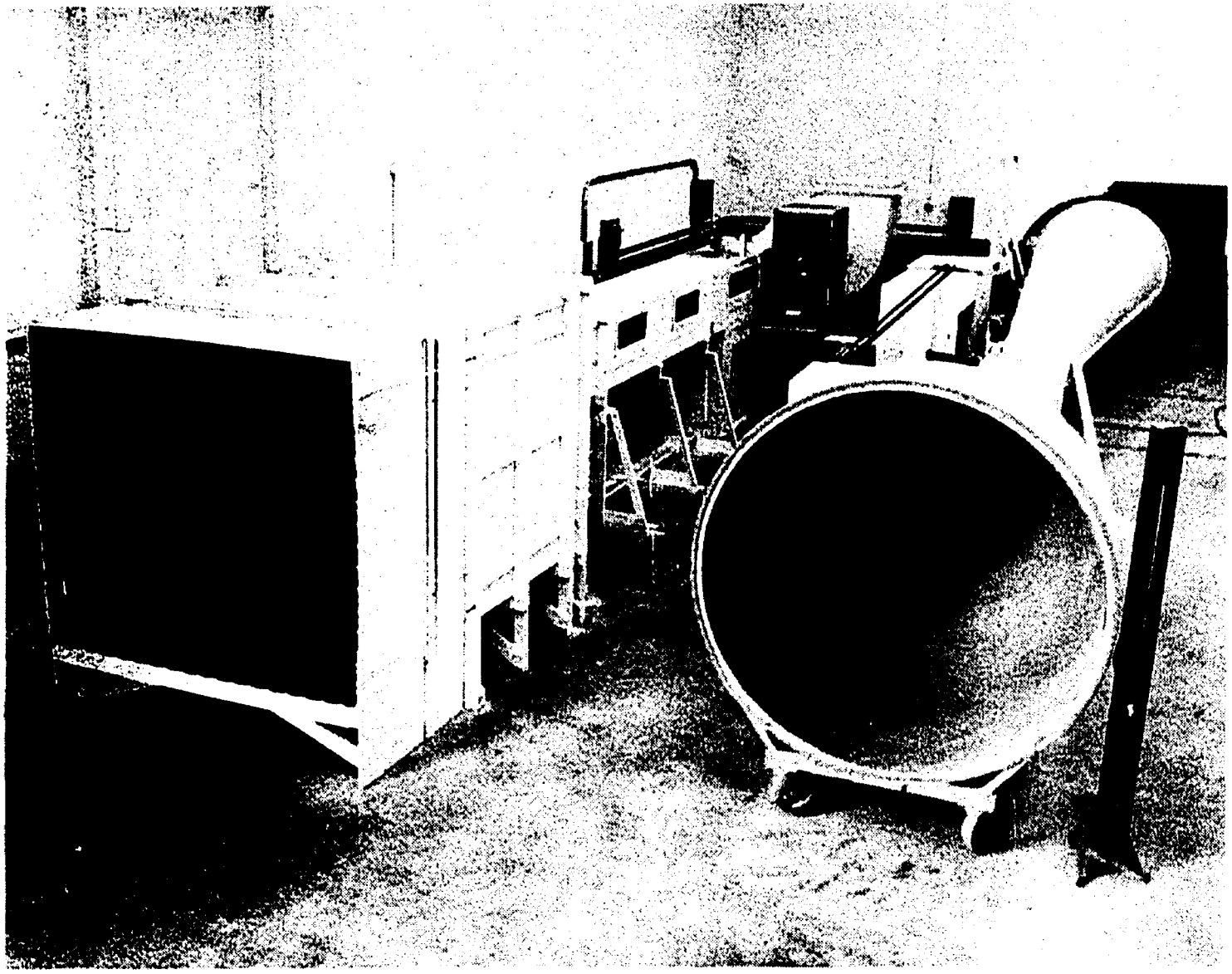

Figure 2.3. Overall view of wind tunnel arrangement.

box, or settling chamber, was used with a two foot post-contraction length. The four foot settling chamber allowed time for honeycomb and screen flow disturbances to dampen considerably before entering the contraction. The two foot post-contraction length assisted in providing fully developed parallel flow before reaching the leading edge of the B.L.D. plate.

From test section turbulence measurements by the author and tabulated experimental data by Dryden and Schubauer [27], three 16 x 18 mesh fiberglass screens, separated by distances of 4.5 inches and 12 inches respectively, measured in the direction of flow, provided the lowest main stream turbulence level.

A honeycomb was constructed from 288 four-inch diameter, one foot long, 24 gage galvanized steel cylinders, stacked vertically rather than offset. The cylinders were fastened in a plywood frame such that the trailing edge of the cylinders was one foot from the first fiberglass screen. This honeycomb arrangement helped to provide proper alignment of air, suppress lateral velocities and eliminate or dampen bursts of air in the test section region (see honeycomb in Fig. 2.3).

The effectiveness of the screens and honeycomb is shown in Table 2-1 below.

Without the honeycomb or screens installed on the entrance section, an 11% level of turbulence was observed. The honeycomb with three screens was a slight improvement over the honeycomb with two screens.

The inside of the contraction was finished with two coats of sanding lacquer sealer and two layers of a hard finish paste wax. The outside corners of the contraction section were sealed with fiberglass

cloth and epoxy resin.

Table 2-1

TEST OF SCREEN AND HONEYCOMB EFFECTIVENESS

Configuration	u'/U_1, percent
Pre-contraction Area Open	11.1
No Honeycomb, one screen installed	4.14
No Honeycomb, two screens installed	2.51
Honeycomb, two screens installed	0.3-0.4
Honeycomb, three screens installed	0.15-0.5

Diffuser Section and Drive Unit

To convert the kinetic energy of the airstream leaving the test section into pressure energy before reaching the driving unit, an efficient expansion section was needed. The total angle of the expansion for most subsonic diffusers has been recommended by Pope [28], and Pankhurst and Holder [25], to be 5 to 7 degrees. However, due to space limitations the author used a 10° total angle.

A fan, built by the New York Blower Company, was purchased for the drive unit. This fan, a type ME No. 330 with a PL wheel, had a wheel diameter of 33 inches, a fan outlet area of 6.28 square feet, and an inlet diameter of 36.5 inches. This fan was set on four 3/4 inch diameter threaded rods welded to a 10 inch steel channel and I-beam frame. Also on this frame was attached a General Electric, 1760 R.P.M., 220 V.A.C., 20 H.P. electric motor for the power source of the drive unit. The drive

unit frame was isolated from the test room by twenty medium-hard rubber disks, about 3/4 inch thick and 1 1/4 inches in diameter. The fan was fixed at 670 R.P.M. with a 2.625 pulley ratio. According to the fan specifications, at 670 R.P.M. and approximately 3/4 inch pressure drop across the inlet-outlet, it could deliver approximately 13,000 CFM. A parallel blade outlet damper was then constructed to provide a fine adjustment of tunnel test section velocity. At the design speed of 50 feet/second the tunnel had a volume flow requirement of approximately 10,000 CFM. The test section now had a velocity range of 0-60 fps and with a pulley ratio of 1.535, a range of 0-175 fps was measured.

Since the test section dimensions corresponded to a hydraulic diameter of 25 inches and the fan inlet diameter and desired diffuser angle were known, the diffuser length could now be determined. The length was 5.7 foot with a two inch straight flange on the aft end for attachment to the blower. A two foot long rectangular-to-round converter section was soldered to the front end of the diffuser. Between the aft end of the test section and the converter section was placed a vibration isolator region made from a vinyl material (see Fig. 2.4). With this isolator section and the rubber disks on the fan-motor frame, the test section vibration due to the drive unit was minimized.

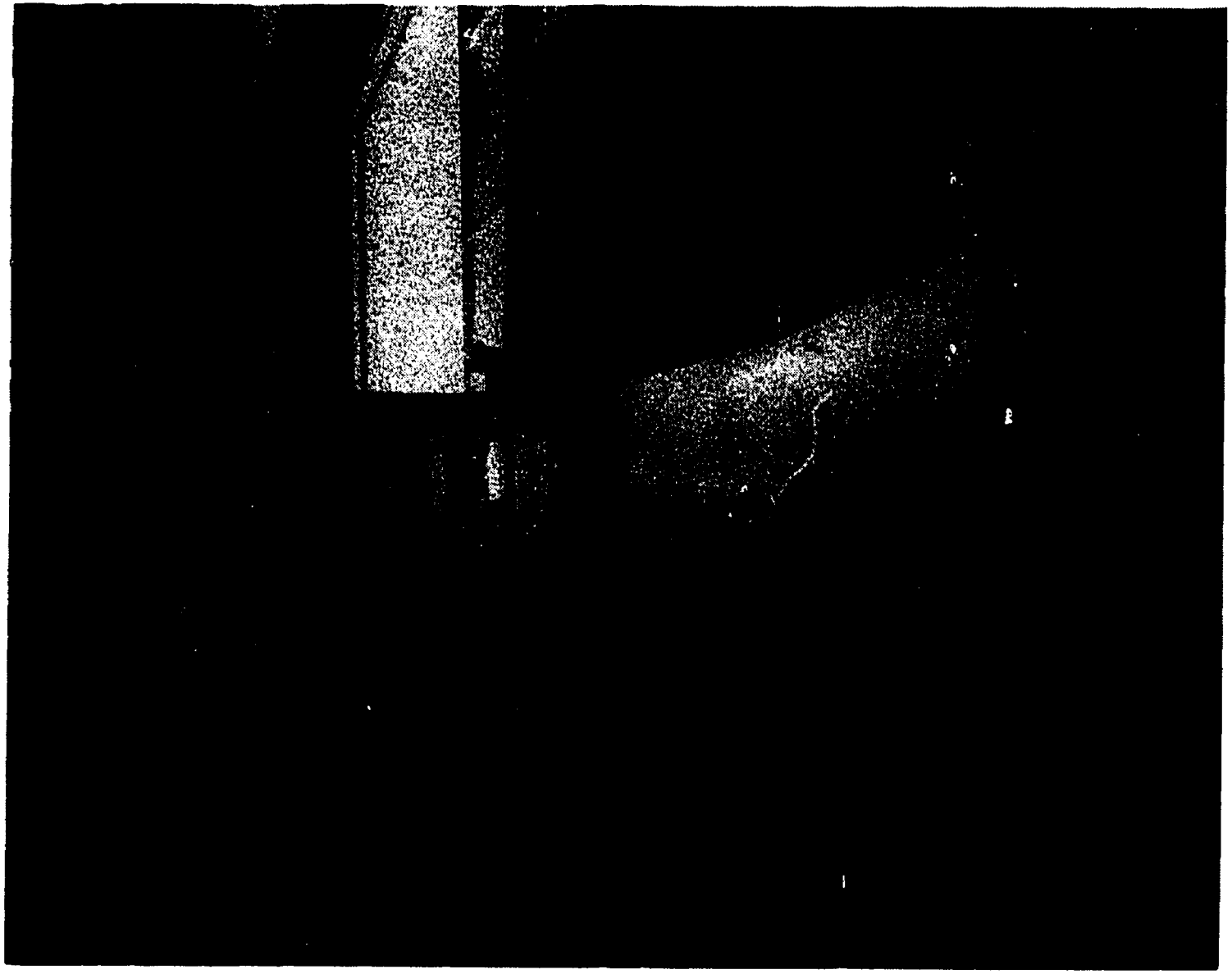

Figure 2.4. View of work area of wind tunnel, showing contraction, test section, and diffuser.

CHAPTER III

EXPERIMENTAL INVESTIGATION

After assembling the wind tunnel components as described in the previous chapter, the major portion of the construction phase was complete. The next phase was initiated by acquiring the necessary instruments, some of which were available from previous experiments [18]. The instrumentation was selected on the basis of the desired measurements, namely, those terms of the turbulent boundary layer energy equation that could be measured with a modern hot-wire anemometer system and associated accessories. The desired measurements are enumerated below.

Delineation of Energy Balance

The energy balance for the turbulence at a given cross section in a two dimensional boundary layer is given by Klebanoff [22] as:

$$\begin{matrix} \text{I} & & \text{II} & & \text{III} \\ \overline{uv}\,\partial U/\partial y + 1/2\,\partial(\overline{u^2}v + \overline{v^3} + \overline{vw^2})/\partial y + (1/\rho)\partial(\overline{p_i}v)/\partial y \\ \text{IV} & & & & \text{V} \\ + 1/2\,U\partial(\overline{u^2} + \overline{v^2} + \overline{w^2})/\partial x + 1/2\,V\,\partial(\overline{u^2} + \overline{v^2} + \overline{w^2})/\partial y \\ & & \text{VI} \\ - \nu(\overline{u\nabla^2 u} + \overline{v\nabla^2 v} + \overline{w\nabla^2 w}) = 0 \end{matrix} \qquad (3.1)$$

The terms listed in the equation have the following physical interpretation:

I. Production of turbulent energy from the mean motion

II. Turbulent energy diffusion

III. Pressure diffusion

IV. Convection of turbulent energy by the x-component of the mean motion

V. Convection of turbulent energy by the y-component of the mean motion

VI. Dissipation of turbulent energy

The two convection terms, IV and V, according to Klebanoff [22], can be transformed into a single nondimensional term.

$$C_1 = -\left[4/5 \frac{\delta}{U_1^2 X_o} \int_0^{y/\delta} \frac{U}{U_1} d(y/\delta)\right] \frac{d\left(\frac{\overline{u^2} + \overline{v^2} + \overline{w^2}}{2}\right)}{d(y/\delta)} \qquad (3.2)$$

The dissipation term (VI) can also be rewritten into a more suitable form for hot-wire anemometer measurements:

$$\nu \frac{d}{dy}\left(\frac{\overline{u^2} + \overline{v^2} + \overline{w^2}}{2}\right) - \nu\left[\overline{\left(\frac{\partial u}{\partial x}\right)^2} + \overline{\left(\frac{\partial v}{\partial x}\right)^2} + \overline{\left(\frac{\partial w}{\partial x}\right)^2} + \overline{\left(\frac{\partial u}{\partial y}\right)^2}\right.$$

$$\left. + \overline{\left(\frac{\partial u}{\partial z}\right)^2} + \overline{\left(\frac{\partial v}{\partial y}\right)^2} + \overline{\left(\frac{\partial v}{\partial z}\right)^2} + \overline{\left(\frac{\partial w}{\partial y}\right)^2} + \overline{\left(\frac{\partial w}{\partial z}\right)^2}\right] \qquad (3.3)$$

Therefore, from (I) of equation (3.1), it is necessary to obtain the distributions of the Reynolds stress ($\overline{-\rho uv}$) and the mean velocity across the boundary layer. The diffusion terms, II and III, do not lend themselves to presently available hot-wire anemometer techniques and would have to be determined by balancing the energy equation for the rigid wall case if all other terms were known. The term in brackets in equation (3.2) can be evaluated by a graphical integration of a mean velocity

distribution plot. The first derivative of the summation of the turbulent velocity components can be determined readily from a plot of the turbulent velocity components versus the dimensionless height above the plate (y/δ). The first term in equation (3.3) can also be found from a plot of the distribution of the turbulent velocity components by using a first central difference technique.

$$\frac{d^2 f_i}{dy^2} = \frac{f_{i+1} - 2f_i + f_{i-1}}{(\Delta y)^2} \tag{3.4}$$

Five of the remaining terms of the dissipation component can be determined by other hot-wire anemometer techniques. The values of $\overline{(\partial u/\partial x)^2}$, $\overline{(\partial v/\partial x)^2}$, and $\overline{(\partial w/\partial x)^2}$ can be determined from a space-time transformation as described in Appendix C; for example,

$$\overline{\left(\frac{\partial u}{\partial x}\right)^2} = \frac{1}{U^2}\overline{\left(\frac{\partial u}{\partial t}\right)^2} \tag{3.5}$$

Values for $\overline{(\partial u/\partial y)^2}$ and $\overline{(\partial u/\partial z)^2}$ can be determined from measuring the correlation coefficients R_y and R_z, as described in Appendix D; for example,

$$R_y = \frac{\overline{u(y)\, u(y + \Delta y)}}{u'(y)\, u'(y + \Delta y)} = 1 - \left(\frac{1}{2\overline{u^2}}\right)\overline{\left(\frac{\partial u}{\partial y}\right)^2}(\Delta y)^2 \tag{3.6}$$

where

$$\Delta y \to 0$$

The above measurements that have been described as being possible, as well as the spectrum of turbulence measurements, have been made for both compliant and rigid wall cases. These experimental results are

described in the next chapter. The instrumentation and procedure for obtaining the necessary measurements are described below and in the Appendices.

Instrumentation

All of the measurements to be described were made at the X = 10.5 foot station, except for the pressure gradient measurements mentioned in Chapter II. A hole was drilled through the double ceiling at this station and the probe transversing mechanism (shown in Figure 3.1) was installed. This mechanism had the capability of normal movement only to the test plate, and could be read to 0.005 inches. It was designed to hold the single wire and cross-wire hot-wire anemometer probes.

The main instrumentation consisted of the Flow Corporation Model CCB two-channel hot-wire anemometer system. This system contained a constant current hot-wire anemometer (C in Figure 3.2), a sum and difference control unit (D) and a random signal voltmeter (B), which had a 16 second time constant and a peak factor of 25.

This system was used for velocity measurements as described in Appendix A in the $y < 0.125$ inch range. A hot-wire velocity calibration curve was obtained before each run. The Model CCB was also used for all of the turbulence measurements by utilizing the single wire for u' component and the horizontal and vertical x-array probes for the v' and the w' component, respectively. Tungsten wire, 0.00035 inches in diameter, with an exposed length of 0.04 inches was used on all of the probe tips. A better signal-to-noise ratio would have been possible with a smaller diameter wire but it would have been too delicate for

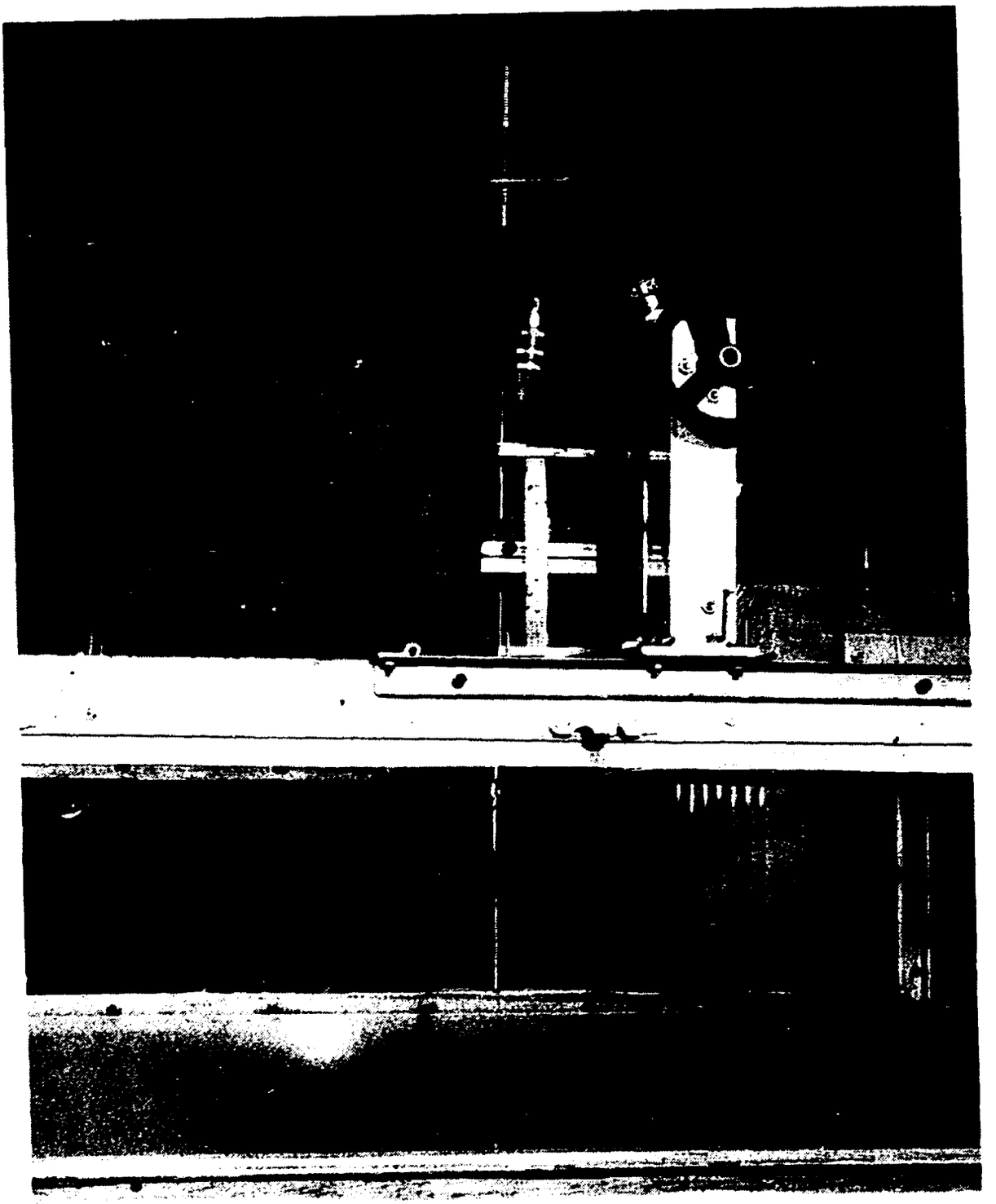

Figure 3.1. Probe traversing mechanism installed on wind tunnel test section.

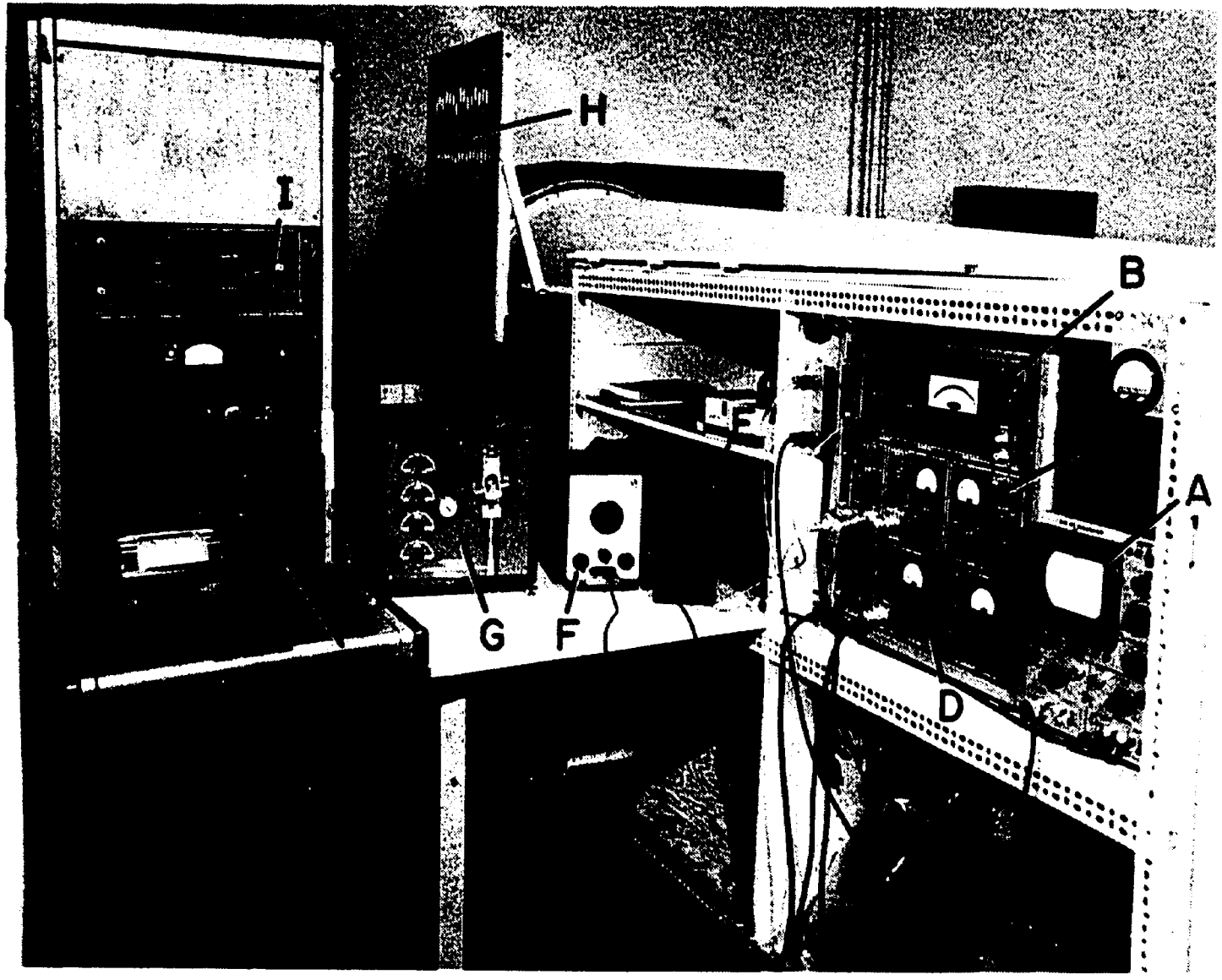

Figure 3.2. View of hot-wire anemometer system and accessory equipment.

shipping and handling. A 7KC low-pass filter was connected to the output of the hot-wire anemometer to eliminate high frequency noise.

An oscilloscope (A) was used to monitor the anemometer output signal and to set the compensation frequency of the anemometer output amplifier by the square-wave calibration method [29]. For sufficient amplification the attenuation switch of the anemometer output was set to (4) while taking single wire turbulence and $\overline{(du/dt)^2}$ measurements as shown on data sheet Form 2B in Appendix E. Measurements for $\overline{(du/dt)^2}$, $\overline{(dv/dt)^2}$ and $\overline{(dw/dt)^2}$ were made with the differentiation system (E) as detailed in Appendix C. As described, the time derivative was converted to the spatial derivative as needed for the energy equation of the turbulent flow, discussed in the previous section of this chapter.

The single wire turbulence equations used for X-array hot-wire measurements of v' and w' were taken from Gessner [30]. He described a technique for taking such measurements with two well-matched hot wires on each x-array probe. The wires used for this investigation had unheated resistances that agreed within 5 per cent and heated resistance agreement within 3 per cent as required by Gessner. The probes were visually aligned with the flow stream for each measurement. Alignment error was checked by rotating the probe slightly and observing any changes in anemometer output readings for both wires. For small angles, well above visual alignment error, no changes in output were recorded. No wire length corrections were made for any of the measurements.

Measurements of the spectra of turbulent energy were made with the General Radio sound and vibration analyzer (I) which had a frequency range from 2.5 cps to 25,000 cps. The method used to obtain the measure-

ment is described in Appendix B. Permanent records of the spectra data were made with the graphic level recorder (J) connected to the sound and vibration analyzer.

Both the differentiation systems (E) and the sound and vibration analyzer were calibrated with the audio oscillator (F). The rough measurements of the pressure gradient were made with the board manometer (H). A pitot tube and the micromanometer (G) were used for most of the velocity measurements, as described in Appendix A. The micromanometer (G) was also used for a fine adjustment of the pressure gradient.

The probability distribution of the u' velocity component was measured with a Bruel and Kjaer Model 161 Probability Density Analyzer. The output was recorded on a Hewlett-Packard XY Plotter. The Model 161, which had a 0.1 sigma window width, was set on a 32-minute sweep time to obtain a good time average of the signal.

Preliminary Tests

After the instrumentation setup was complete and the zero pressure gradient set, measurements of the distribution of the mean velocity were made. For a natural transition of the flow from the leading edge of the B.L.D. plate, a 2.2-inch boundary layer thickness was measured. In order to make comparisons with Klebanoff's work [22], a No. 16 floor-sanding paper was installed as described by Klebanoff and Diehl [31]. After resetting the zero pressure gradient, which was the same as shown in Figure 2.2, the transverse velocity profile across the wind tunnel (z-direction) and a normal profile (y-direction), from test plate to ceiling were made, as indicated in Figures 3.3 and 3.4 re-

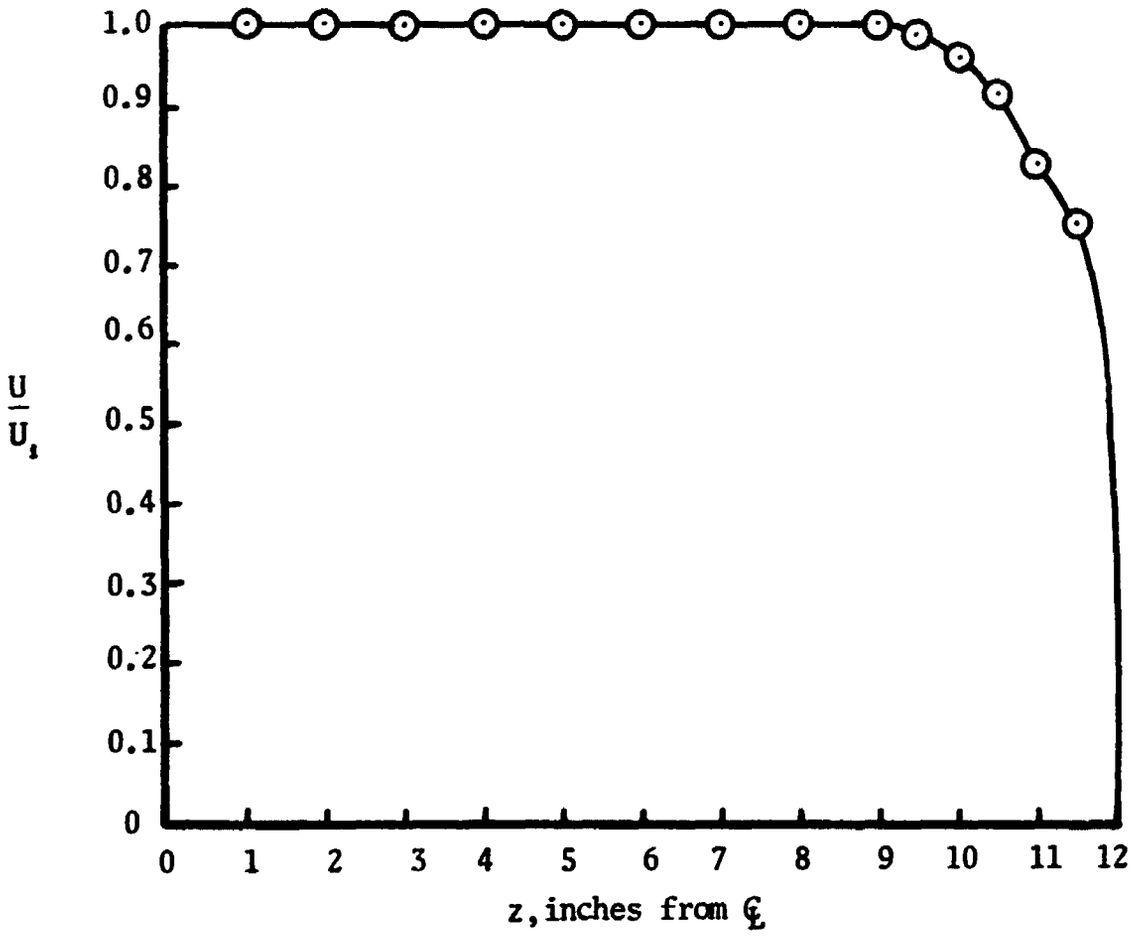

Figure 3.3. Transverse velocity distribution.

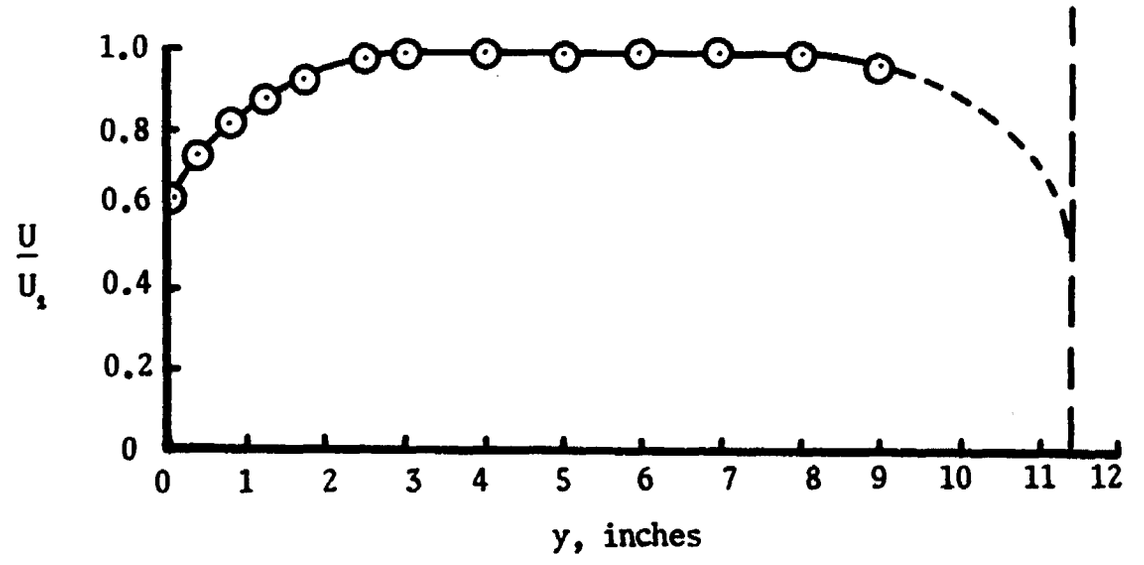

Figure 3.4. Normal velocity profile across test section.

spectively. The transverse (z-direction) velocity profile indicated that a two-dimensional flow assumption was valid. The free stream condition, or an area apparently unaffected by the presence of the walls, was substantiated by the normal velocity profile.

Hard plate tests were then initiated with a careful measurement of mean velocity distribution. As shown in Figure 3.5, the velocity distribution was in excellent agreement with that of Klebanoff [22]. Good agreement also existed for the "1/7 power law."

The values of u' as well as U were obtained as close to the wall as 0.01 inches where Klebanoff obtained values to 0.004 inches. Due to the geometry of the X-array probes, v' and w' measurements were only obtained as close to the wall as 0.0625 and 0.03125 inches, respectively.

A comparison of the hard plate data versus Klebanoff [22] was plotted in Figure 3.6 for the distribution of u', v', and w' turbulent velocities. The turbulent velocity components have been nondimensionalized by dividing by the free stream velocity, U_1. As shown, the u' and v' components had fair agreement. The u' component differed from Klebanoff [22] by about 5 per cent, while the v' component differed by 10-12 per cent. The hard plate values of u' had a peak at $y/\delta = 0.085$, while the comparison curve of Klebanoff [22] peaked at $y/\delta = 0.0075$. In previous works [18], the peak was found at $y/\delta = 0.095$, for $\delta = 1.0$ inches. No explanation for this peak difference was concluded, except for the fact that smaller diameter hot-wires were used in Klebanoff's experiments which might have produced less interference in the region of the wall. The w' turbulence component was recorded to be 18-20 per cent below

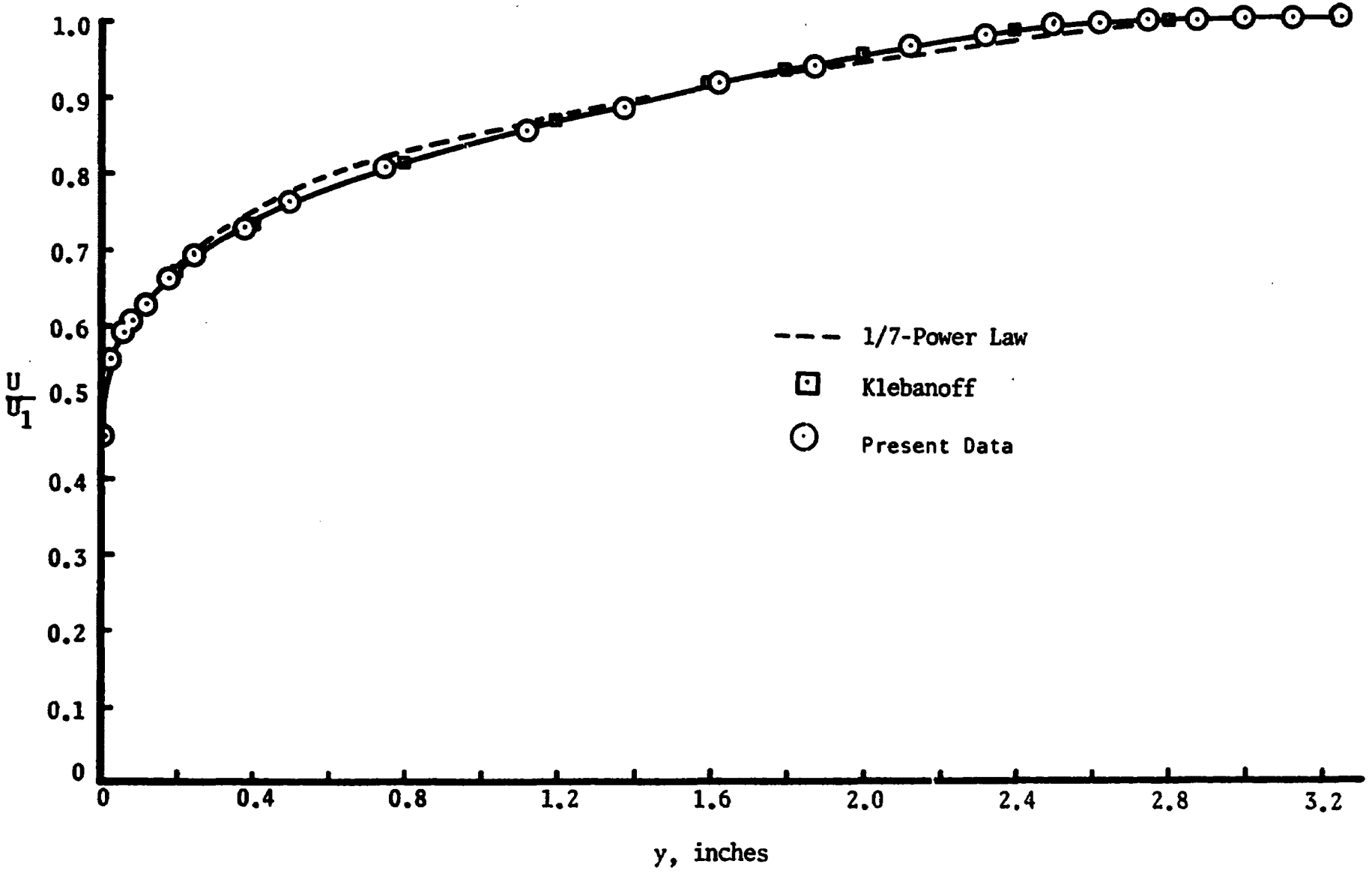

Figure 3.5 . Mean velocity distribution over hard plate.

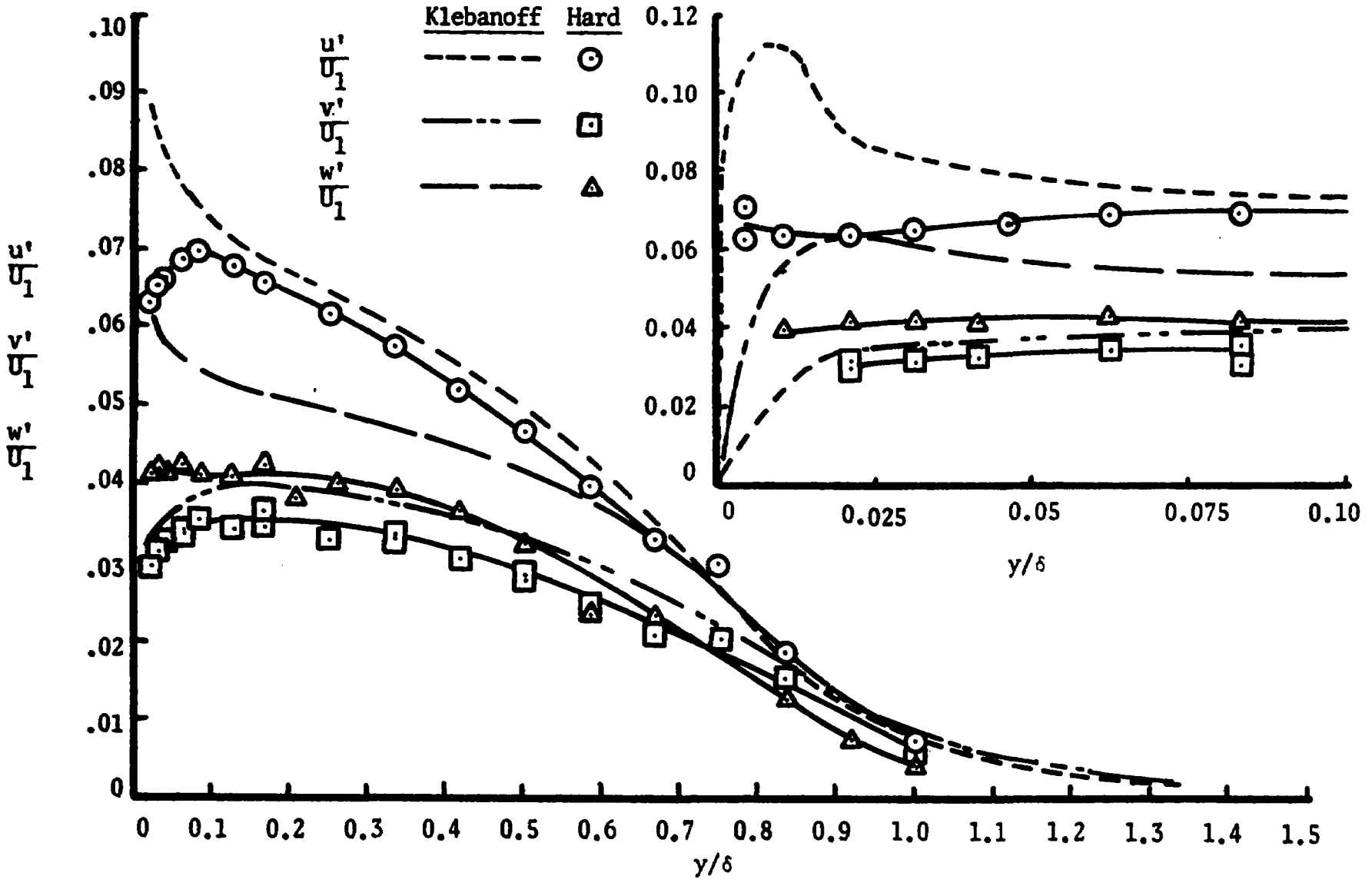

Figure 3.6. Distribution of turbulence intensities, present data compared with Klebanoff [22] for hard plate.

Klebanoff's [22] value.

The values of the turbulent shear stress, or Reynolds stress, were in excellent agreement with those of Klebanoff [22], as shown in Figure 3.7, except for values less than $y/\delta = 0.0625$. An extrapolated wall value of $2\overline{uv}/U_1^2 = c_f = 0.0029$ was obtained. This coincided with a skin friction value given by Squire and Young as described by Klebanoff [22]. This value of c_f at $R_{ex} = 4.2(10)^6$ was also found on a c_f vs. R_{ex} curve given by Dhawan [32]. Fenter [33] has listed a theoretical and experimental curve of c_f vs. R_{ex} for incompressible flow and, at $R_{ex} = 4.24(10)^6$, a value for $c_f = 0.0028$ was found.

The spectrum of turbulence was measured at different y positions in the boundary layer, as shown on Figures 3.8 and 3.9. The data were normalized as indicated in Appendix B. The curves did indicate that as y decreased the wave number increased. They had the same general trend that the curves of Klebanoff displayed. The low wave number, low frequency level region contained the large percentage of energy. The energy decreased with increasing wave number. However, as the plate was approached the energy contained at the high wave numbers increased. The higher wave numbers corresponded to the smaller eddies, the lower numbers to the larger eddies. The magnitude of the $F_u(k_1)$ was lower than Klebanoff's data at the lower wave numbers. This particular variance was partly attributed to differences in the wave analyzer instrumentation. The wave analyzer used for these experiments had a constant percentage (.07f) bandwidth so that at lower frequencies the analyzer averaged the signal over a bandwidth less than one, until about 14 cps. This bandwidth increased to 490 cps at 7000 cps. Klebanoff's wave analyzer had a constant effective

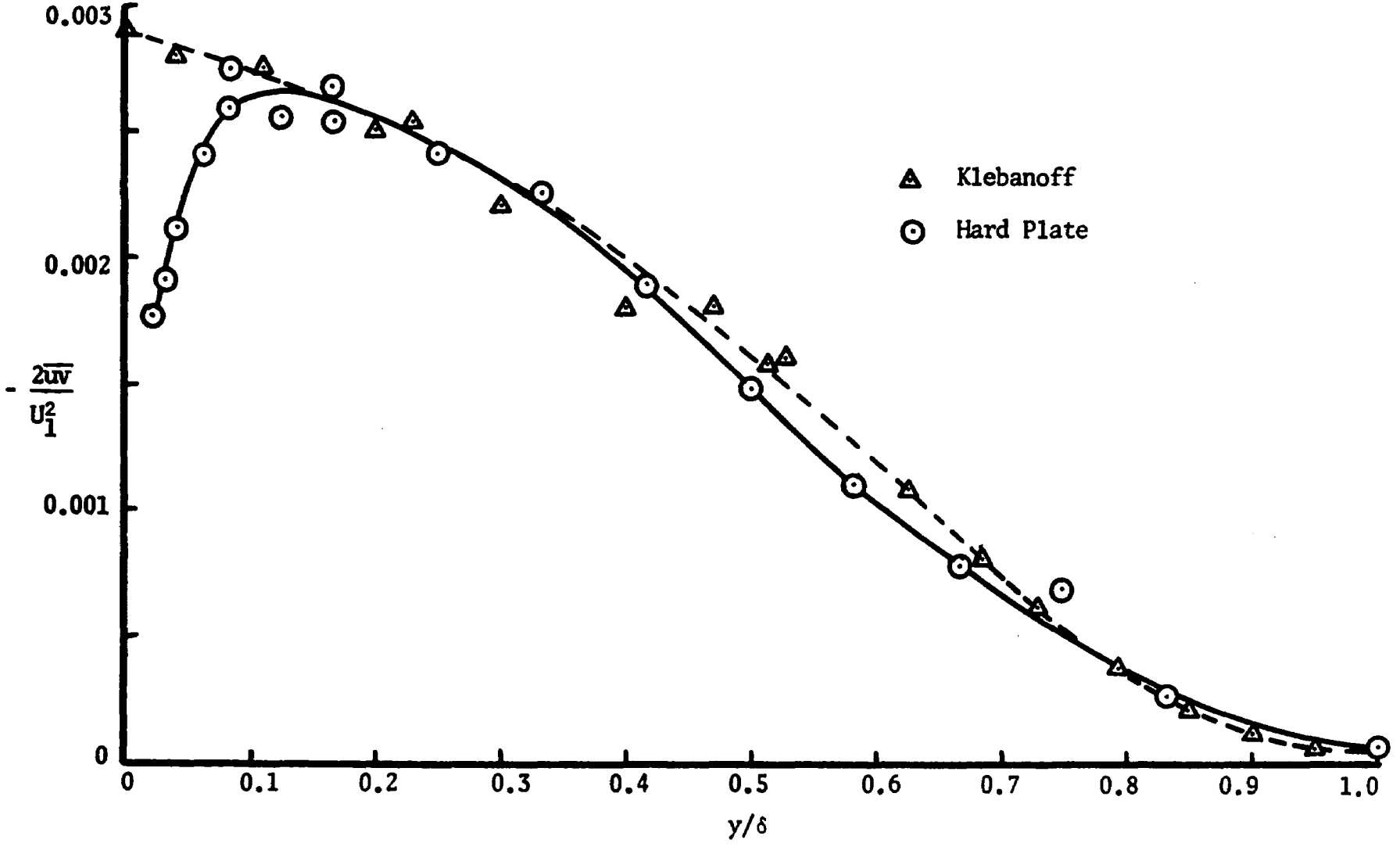

Figure 3.7. Distribution of turbulent shearing stress, present data compared with Klebanoff [22] for hard plate.

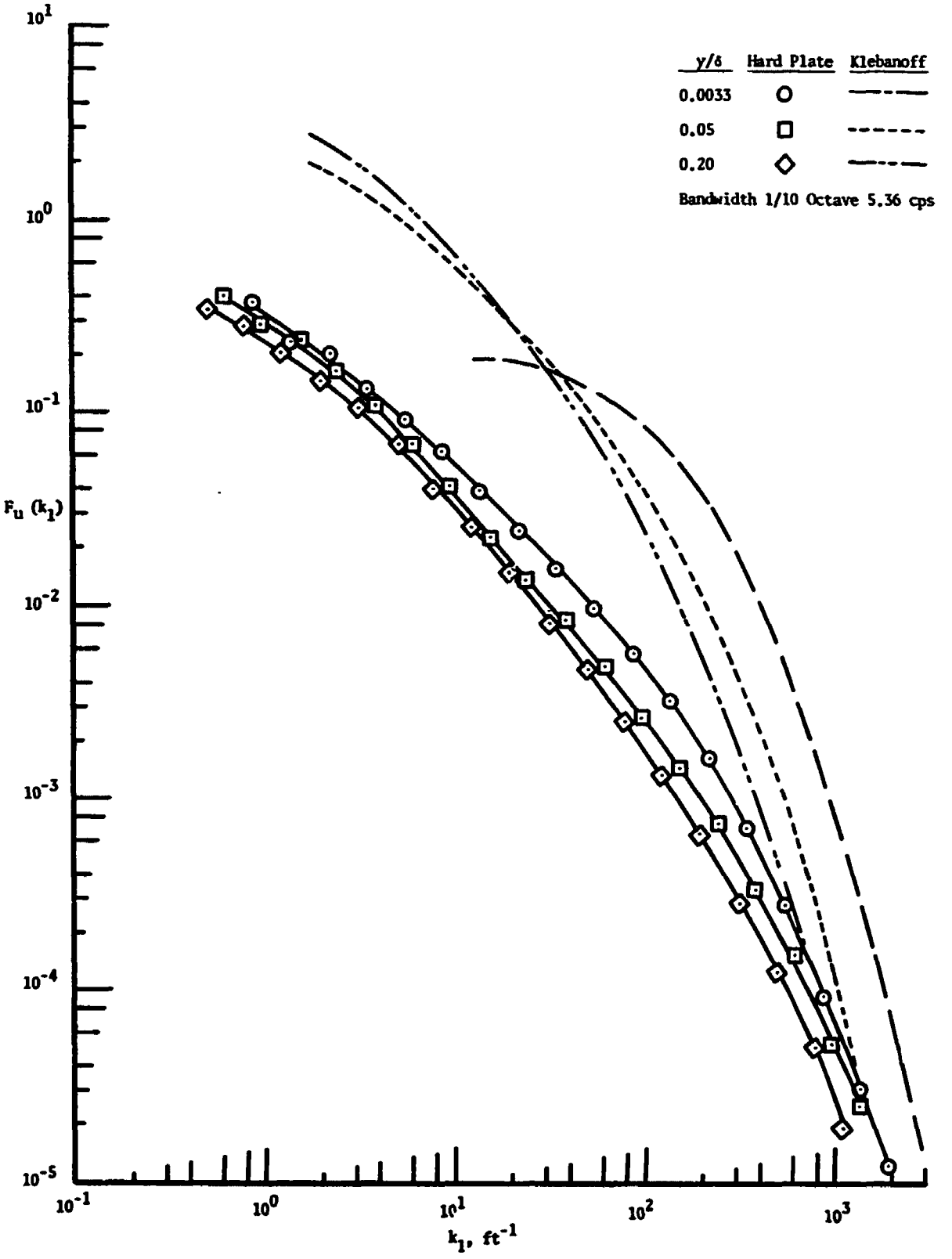

Figure 3.8. Spectra of $\overline{u^2}$ in inner region of boundary layer, hard plate vs. Klebanoff

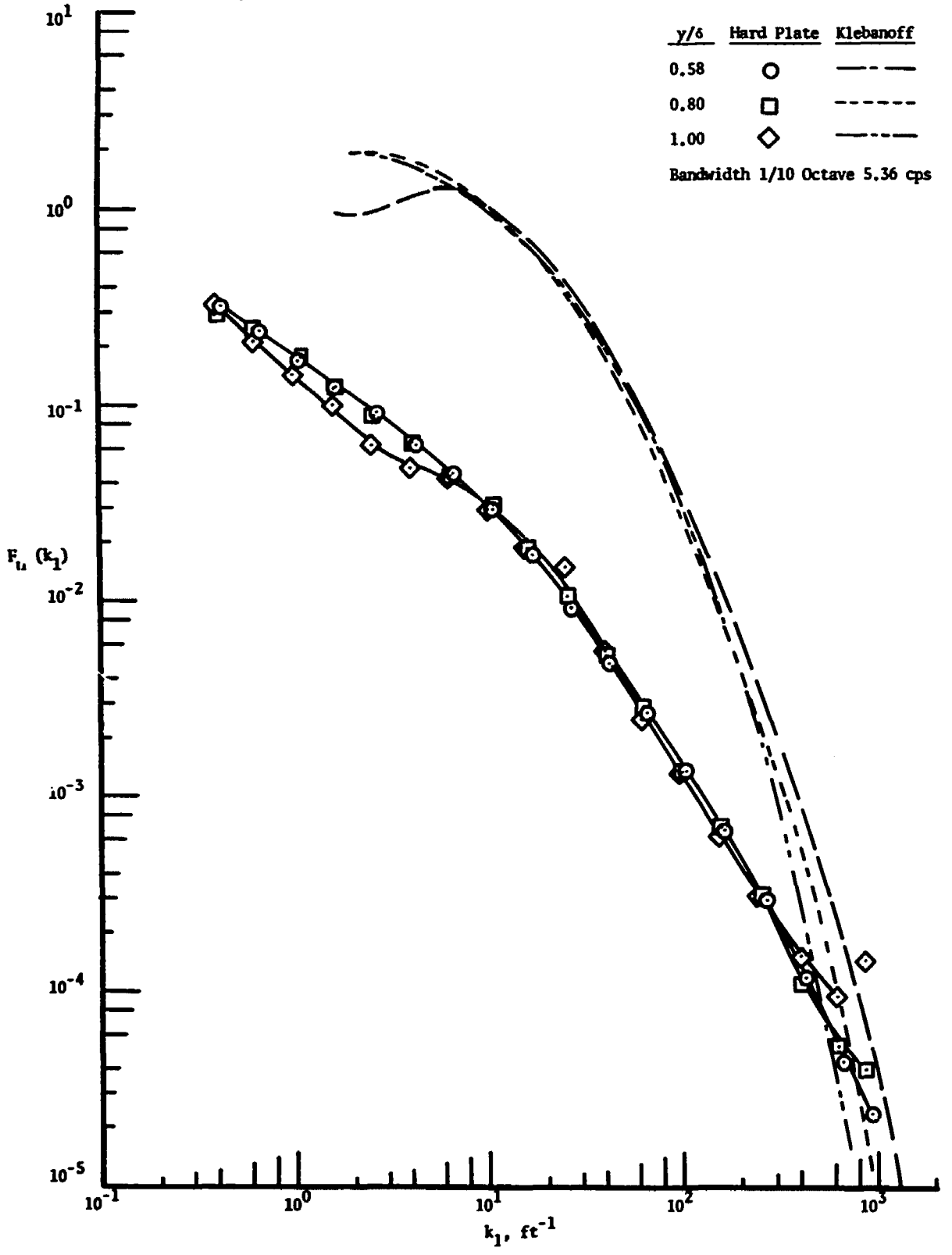

Figure 3.9. Spectra of $\overline{u^2}$ in outer region of boundary layer, hard plate vs. Klebanoff

bandwidth of 5.36 cps throughout the spectrum. The data were repeatable to within 5 per cent over most of the frequency range. The accuracy was less than this value at the two end points due to the large random amplitude fluctuations at frequencies less than 8 cps and the low signal-to-noise ratio at the higher frequencies.

The differentiation circuit had a considerable loss in amplification and also did not compensate for some error caused by assuming q/C to be large compared with R dq/dt, as described in Appendix C. That part of the anemometer signal above 3000 cps was not considered in total due to the non-linear characteristic of the RC differentiation signal above that level (shown in Figure C.2). Klebanoff's data were divided by a factor that would place his curves over the present dissipation derivative curves of $\overline{(\partial u/\partial x)^2}$, $\overline{(\partial v/\partial x)^2}$ and $\overline{(\partial w/\partial x)^2}$ in Figure 3.10. The trend for both curves was generally the same. As found in the distribution of turbulence curves, the peak for the derivatives occurred at a higher value of y than did the comparison data.

Comparisons of Klebanoff's data to other present hard plate measurements are made in the last section of this chapter on the hard plate versus compliant plate curves. Although complete agreement does not exist with the comparison data of Klebanoff's work, the system and procedures used for the work reported in this paper remained identical for both hard plate and compliant plate data. Also, the hard plate data shown previously were the result of not less than two sets of data for most curves. Therefore, these data can be used for a good comparison with the compliant skin data.

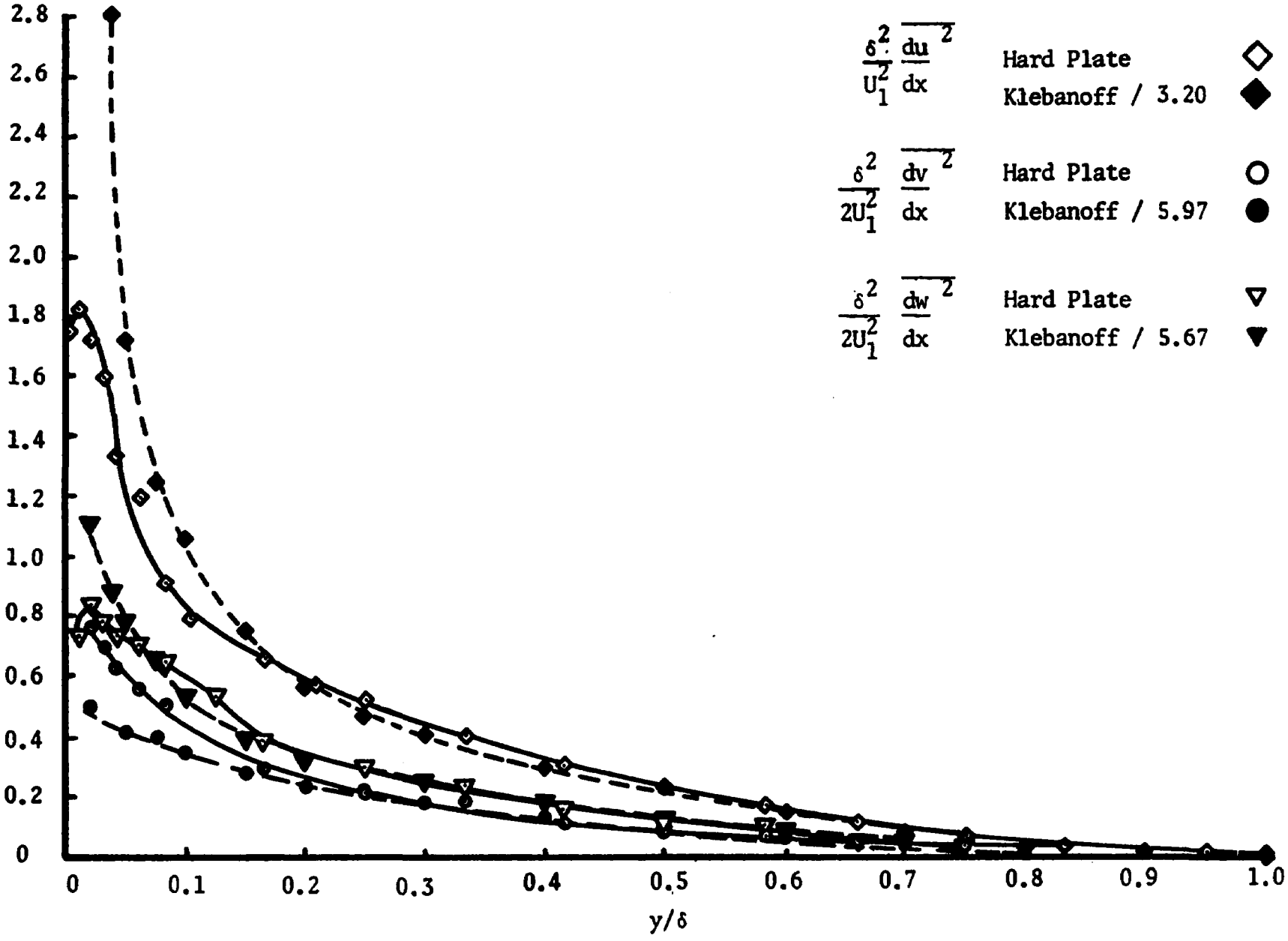

Figure 3.10. Distribution of dissipation derivatives, hard plate vs. Klebanoff [22].

Modification of Tunnel

After the hard plate tests were completed a small compliant surface was constructed from 3/16 inch polyurethane foam (40 P.P.I) and 0.003 inch thick polyvinyl-chloride (PVC) membrane. The polyurethane foam was selected for the substrate on the basis of the promising results of Smith and Blick [34]. They obtained a 25 per cent decrease in the skin friction coefficient at a Reynolds number of approximately one million, using a 0.0030 inch PVC membrane and the thin polyurethane foam.

The foam was bordered by a 3/16 inch high, by 1/2 inch wide balsa wood strip to form a reservoir for the water in the foam. This was placed on the 8 x 26 inch small test plate previously installed in the tunnel and filled with water. The test plate configuration was similar to one used in previous work [18]. The PVC membrane was stretched across the foam with a transverse tension of T_z = 0.1 lb/in and a streamwise tension of T_x = 0.2 lb/in. This tension was selected on the basis of the reference [18] data. The compliant test plate was then inserted flush with the wind tunnel floor. A static tap reservoir was connected to the test plate fluid to equalize pressure above and below the membrane.

A velocity profile and a distribution of the u' component of turbulence were measured. No discernible differences were measured from that of the completely rigid plate.

Therefore, the foam was removed so that only water remained as the substrate. The membrane now seemed to be oscillating slightly, observable in the reflection of a spot light. Slight differences were detectable in initial tests of the velocity profile and u' turbulence

measurements. Therefore the entire series of measurements were run for the small PVC and water compliant plate with the hope that more conclusive differences could be obtained. Only a slight drop in the turbulent shear stress was detected and no differences were observed in the derivative terms. The spectra of turbulence and shear stress revealed no decisive results.

The small compliant plate, 8 inches x 26 inches, apparently did not provide enough length to influence the three-inch thick boundary layer. So a compliant plate was constructed that extended from the trailing edge of the sandpaper, X = 2 ft. to X = 14 foot. This compliant plate provided 8.5 feet of length to influence the flow. The full length compliant plate was constructed from a 3/16 inch sheet of polyurethane foam bonded to the B.L.D. plate with 3M Company "Scotch Grip-44" spray adhesive. A sheet of 0.001 inch PVC membrane was also bonded to the foam with a light coating of the spray adhesive. Static pressure taps from the center of the side wall were inserted into the foam substrate every foot to equalize the pressure differential between the foam substrate and flow region, to insure a flat membrane surface. This provided a seemingly desirable composite membrane-substrate construction. A velocity profile and Reynolds stress measurement were made using the same test conditions and procedures as with the hard plate. No changes were detected.

The same types of material were then used without the spray adhesive bond between the foam and membrane. The membrane was stretched across the foam at a temperature of 90-95°F and clamped to the floor of the tunnel on the sides with 3/16 x 1/2 inch balsa wood strips, visible on the B.L.D. plate in Figure 3.1. Since the tests were run at 80°F, the

membrane was stretched taut in the z-direction. Wrinkles, that were present after installation, were absent at the lower temperature. The initial measurements on the new compliant surface indicated very promising results.

CHAPTER IV

EXPERIMENTAL RESULTS

With the 0.001 inch (PVC) membrane and a 40 P.P.I. polyurethane foam substrate installed, the same data were run as with the hard plates, using the same geometry or configurations. The pressure gradient had to be reset due to apparent changes in the flow. The pressure gradient was set at the same readings as shown in Fig. 2.2.

Presentation of Data

The boundary layer thickness did not have a measurable change but the shape of the mean velocity profile did have a slight measured difference between y = 0.6 and 2.8 inches, as shown in Fig. 4.1. This was the same trend as observed in previous work [18], where an increase in the mean velocity throughout the outer portion or wake region of the boundary layer occurred. At y = 0.01 inches the U/U_1 value was 0.40 for the compliant plate while the hard plate value was 0.455. Part of this difference has been attributed to the difficulty in locating the y = 0.01 inch position on the compliant skin. Since the slope (dU/dy) was at a maximum close to the wall, a slight change in y produced a significant change in velocity. The measurement of y close to the wall has proven to be very critical. During the tests, the measurement of y was made by using the length of a shadow from a spot light positioned at a small

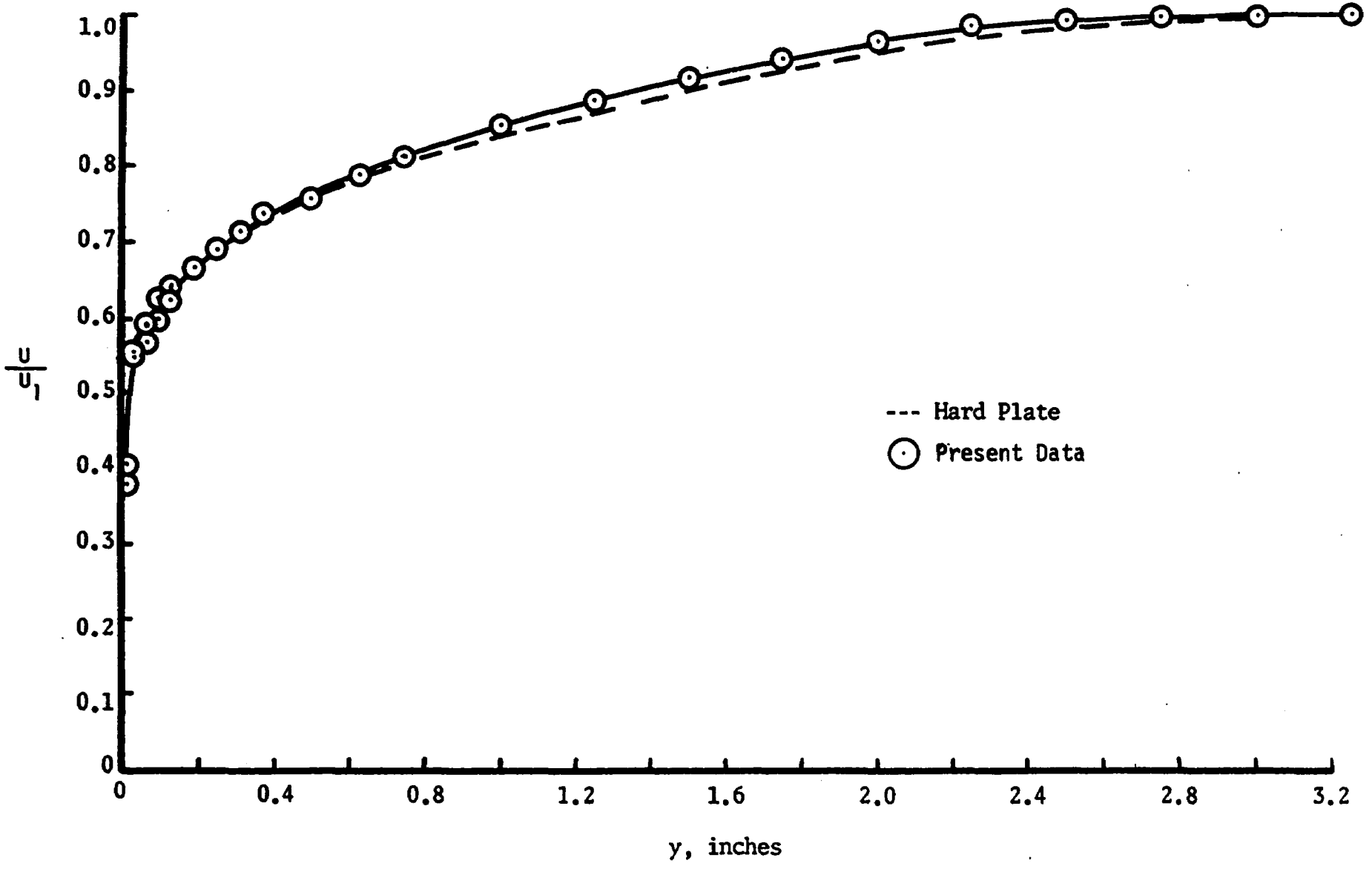

Figure 4.1. Mean velocity distribution for compliant plate with hard plate comparison.

angle from the horizontal. During the compliant plate tests, the y positions in the proximity of the wall had to be determined with the tunnel running since the hot-wire had a slight influence on the compliant displacement of the membrane.

The three components of turbulence measurements for the compliant plate indicated a significant change from hard plate data. The decrease in the u' and v' fluctuating velocities is indicated in Fig. 4.2. The w' component showed a possible decrease for y/δ values greater than 0.08 inches, but increased above hard plate data for y/δ values less than this.

The distribution of the turbulent shearing stress for the compliant plate indicated a very desirable decrease over most of the boundary layer region as compared to the hard plate (see Fig. 4.3). An extrapolated wall value for the local coefficient of friction produced a value for $c_f = 0.00215$ as compared to 0.0029 for the hard plate. This 25 per cent decrease was most significant.

The spectrum of the u' component of turbulence was plotted originally in the same way as the data in Fig. 3.8 and 3.9. To display more vividly the changes that were found, the data have been presented as the difference in energy of hard plate and compliant plate divided by the energy of the hard plate at each frequency. Frequency, rather than wave number, was chosen for the abscissa so that it would not be a function of the mean velocity. As previously discussed, the mean velocity determination was very critical in the region close to the wall. Therefore, this helped to eliminate errors in presenting the spectrum data.

The plot of the percentage change in spectrum energy versus

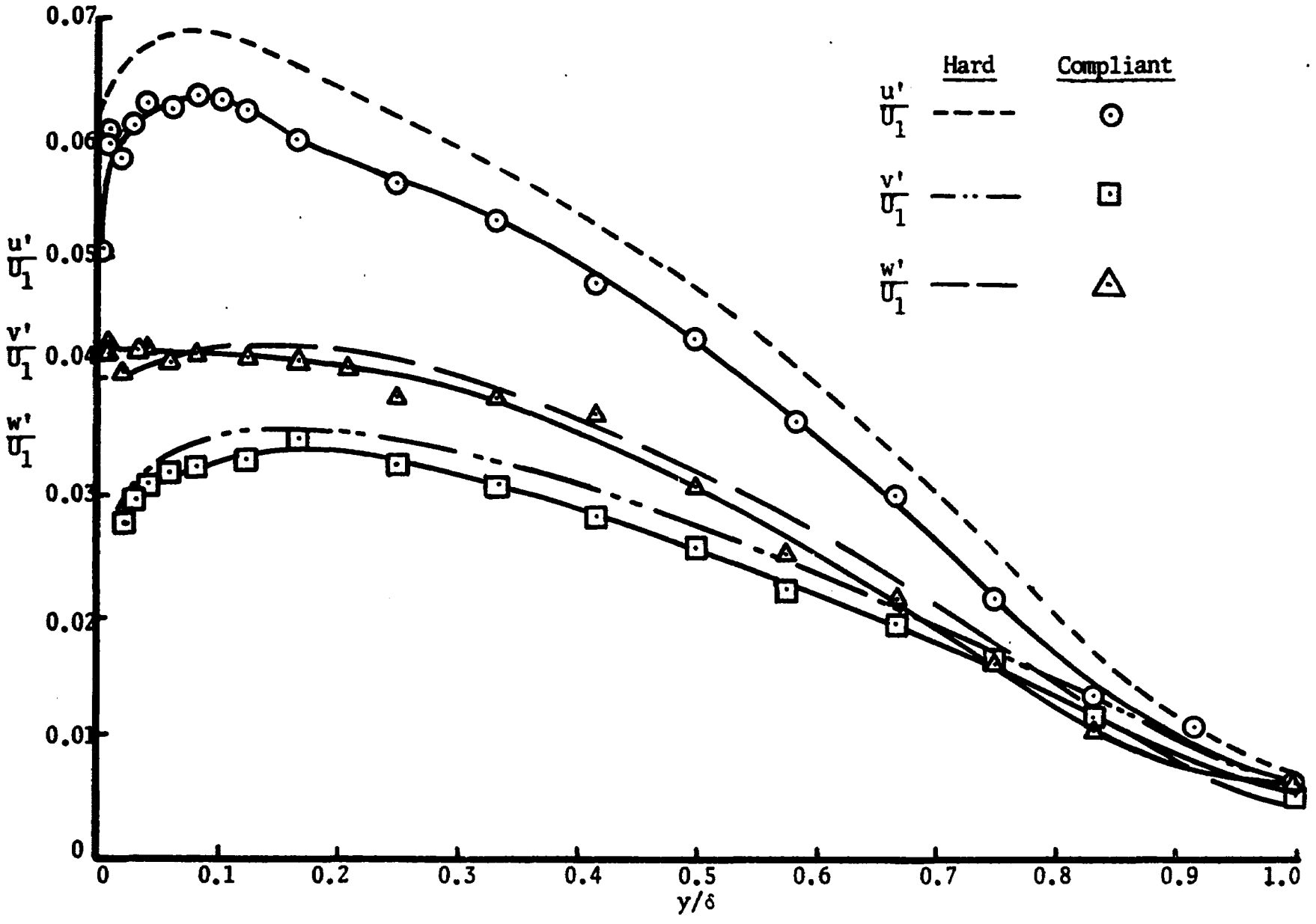

Figure 4.2 . Distribution of turbulence intensities, compliant plate versus hard plate.

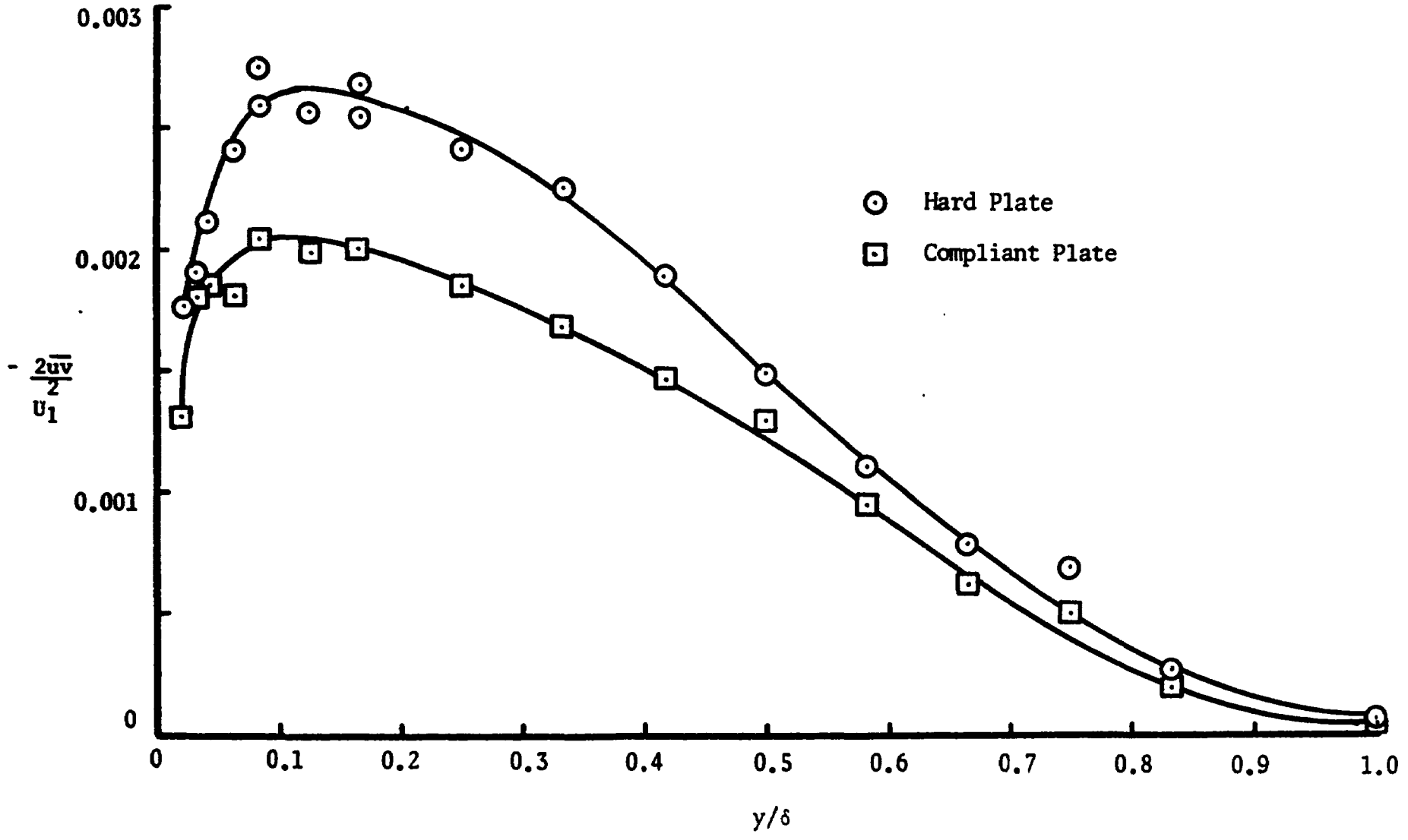

Figure 4.3 . Distribution of turbulent shearing stress, hard plate versus compliant plate.

frequency at the $y/\delta = 0.0033$ position is shown in Fig. 4.4. Considering that the data were repeatable within 5 per cent over most of the frequency range, the change indicated in Fig. 4.4 is significant. As shown, a higher energy level existed for the compliant plate at frequencies less than 60-80 cps and a lower energy level for frequencies greater than 80 cps.

The same type of plot for spectrum at $y/\delta = 0.05$ is somewhat inconclusive but a positive slope of the data is indicated in Fig. 4.5. The data in Fig. 4.6, for $y/\delta = 0.20$, again indicate more energy at lower frequencies, and transitioning from negative to positive around 60-80 cps. The same trend is indicated at $y/\delta = 0.58$ in Fig. 4.7, and more so in Fig. 4.8, at $y/\delta = 0.80$. The data at $y/\delta = 1.0$ in Fig. 4.9 were somewhat vague due to the low signal-to-noise ratio but still indicated a positive slope. Correction for finite length of the wire was not made. This error should increase with the decrease in scale of turbulence at the higher frequencies. However, the data involved here are a comparison of two sets of identically-measured signals.

The distribution of amplitude of the u-fluctuations was recorded with a probability density analyzer as mentioned previously. Unfortunately, the instrument was available for the compliant plate data only, since it was on a trial loan from Barnhill Associates in Dallas, Texas.

Since u denotes the fluctuations of the velocity about some mean velocity, it can be normalized with respect to the time-averaged value of u, that is, $\sqrt{\overline{u^2}} = u'$. If $P(u/u')$ is the probability at any given instant of time of the velocity being between u/u' and $u/u' + du/u'$, the following relationship exists:

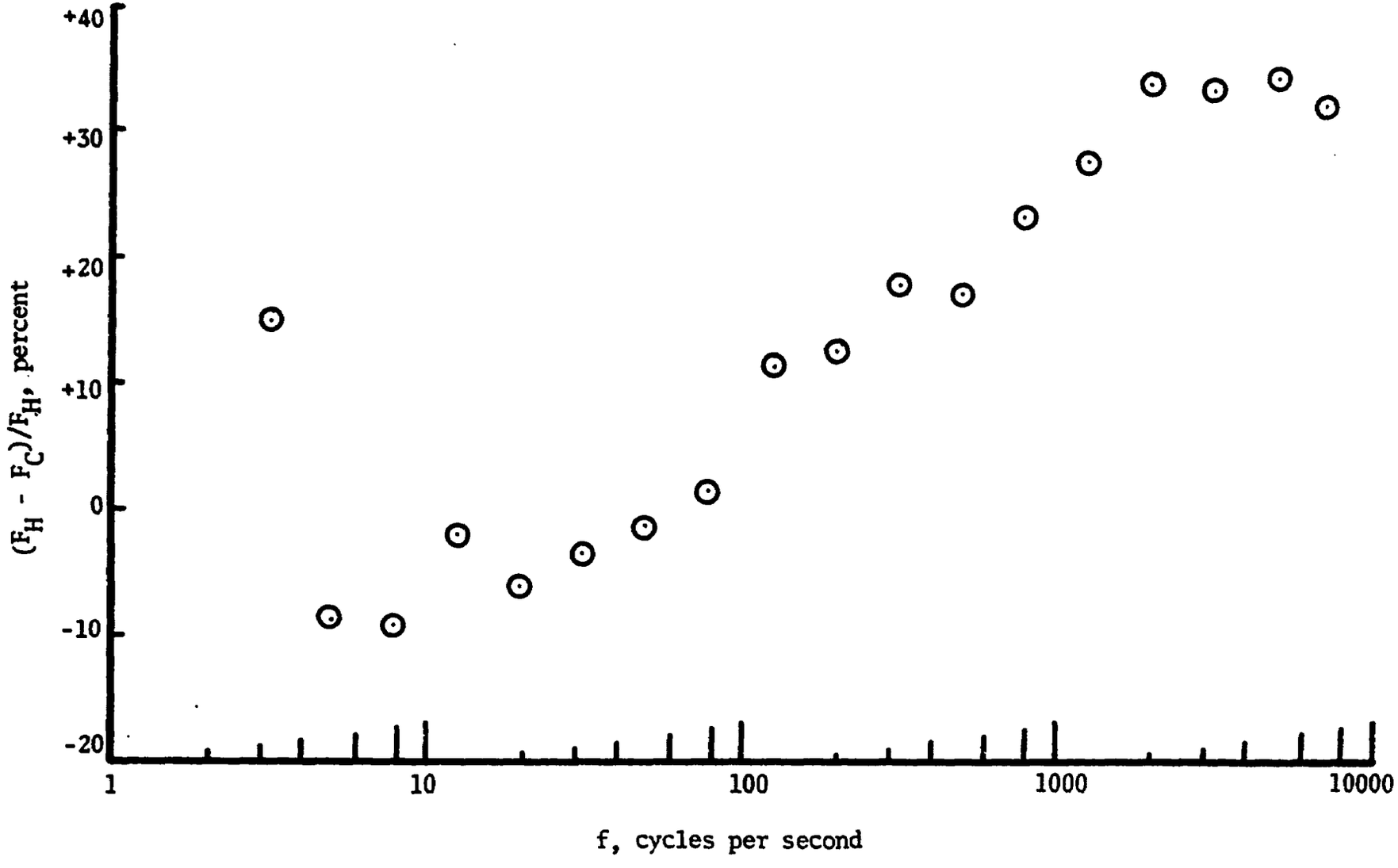

Figure 4.4. Percentage difference between hard plate and compliant plate spectra of turbulent energy at $y/\delta = 0.0033$

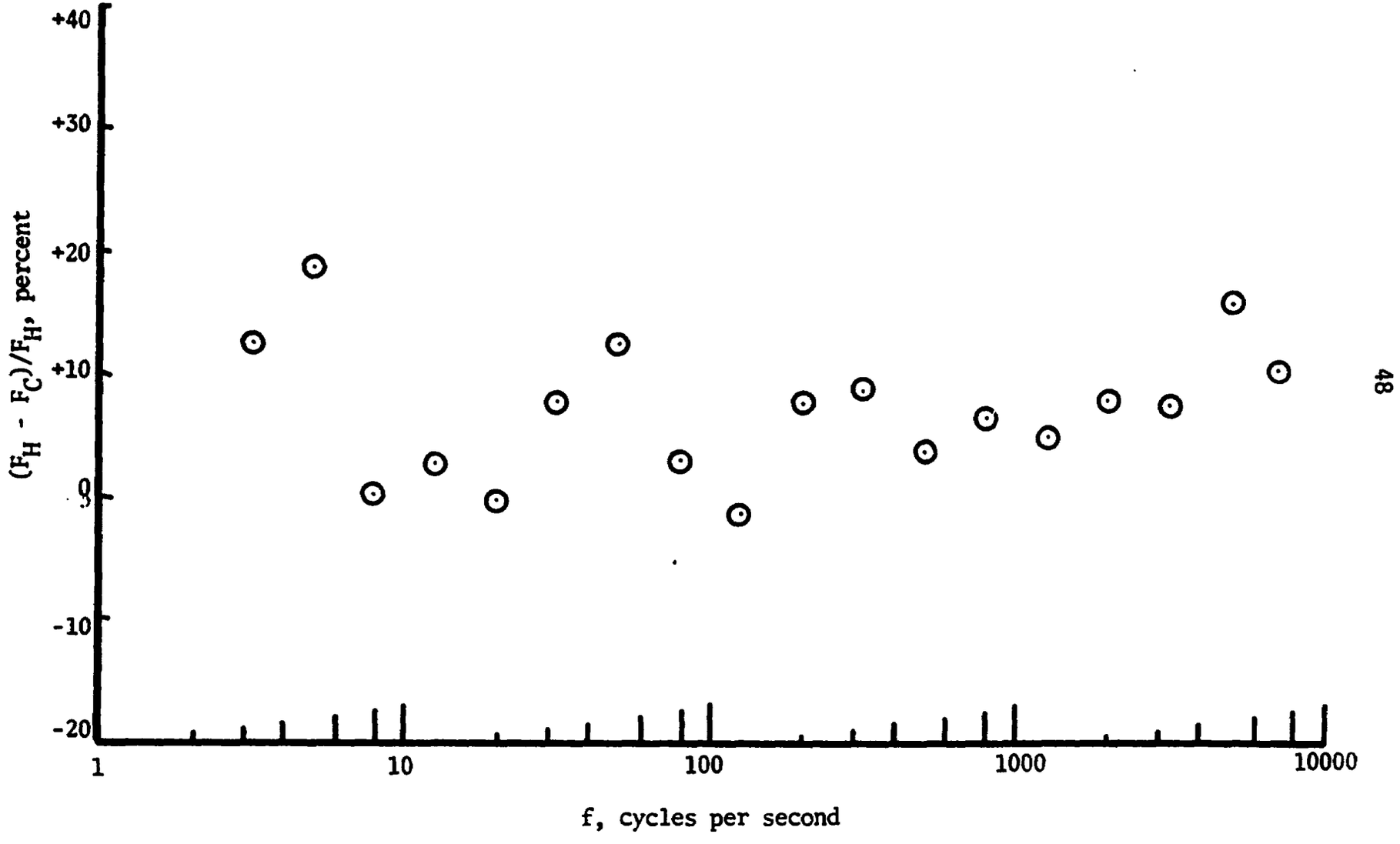

Figure 4.5. Percentage difference between hard plate and compliant plate spectra of turbulent energy at $y/\delta = 0.05$.

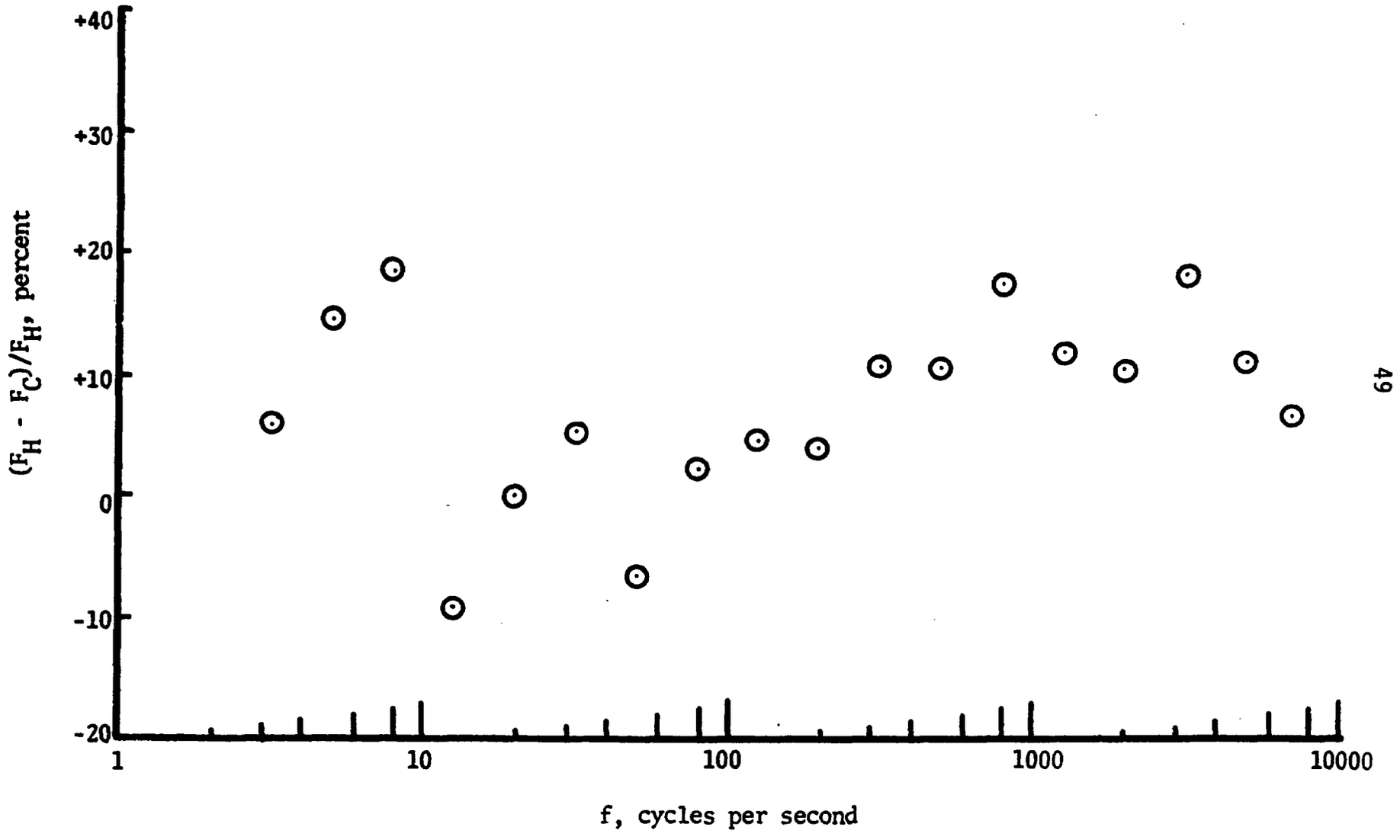

Figure 4.6 . Percentage difference between hard plate and compliant plate spectra of turbulent energy at $y/\delta = 0.20$.

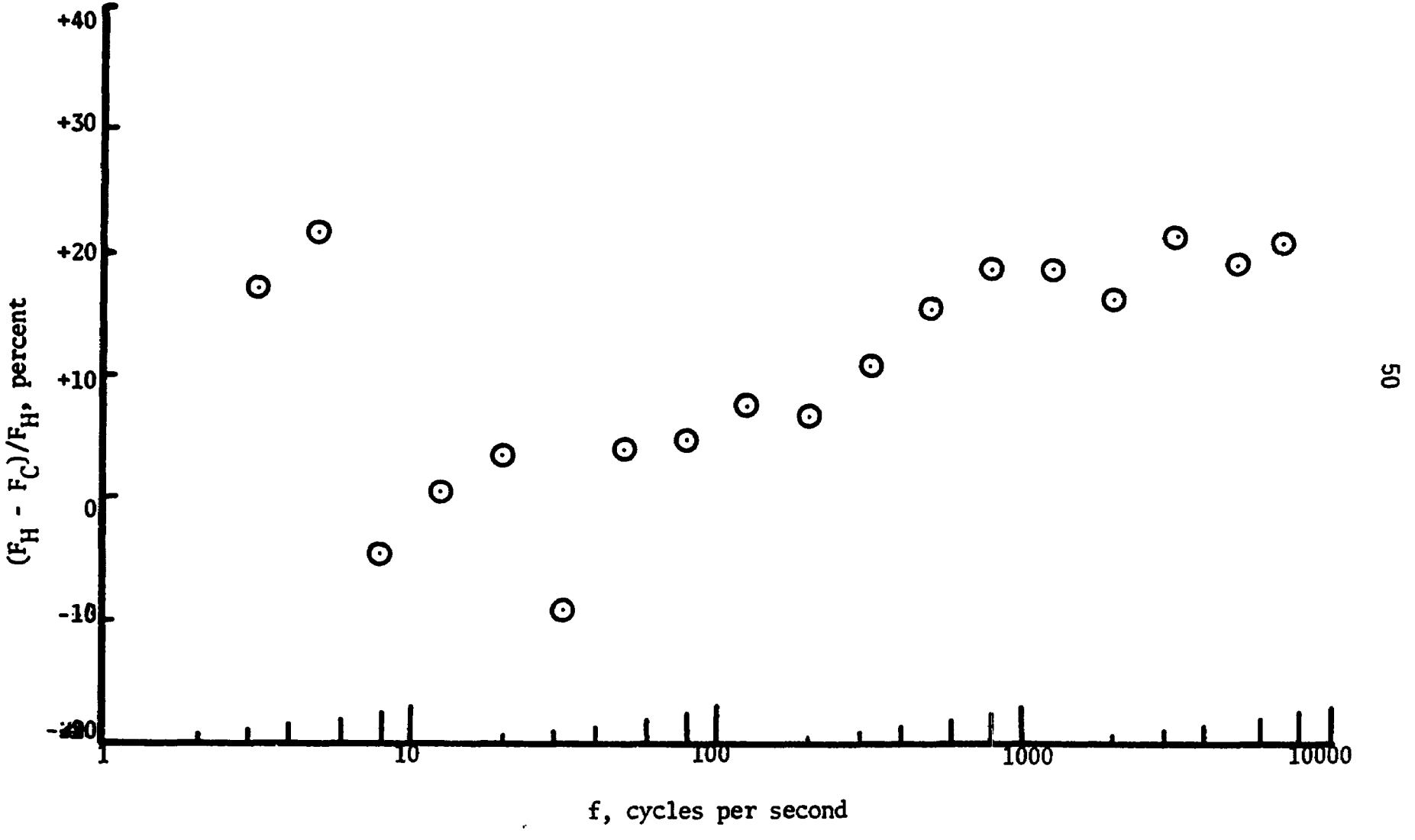

Figure 4.7. Percentage difference between hard plate and compliant plate spectra of turbulent energy at $y/\delta = 0.58$.

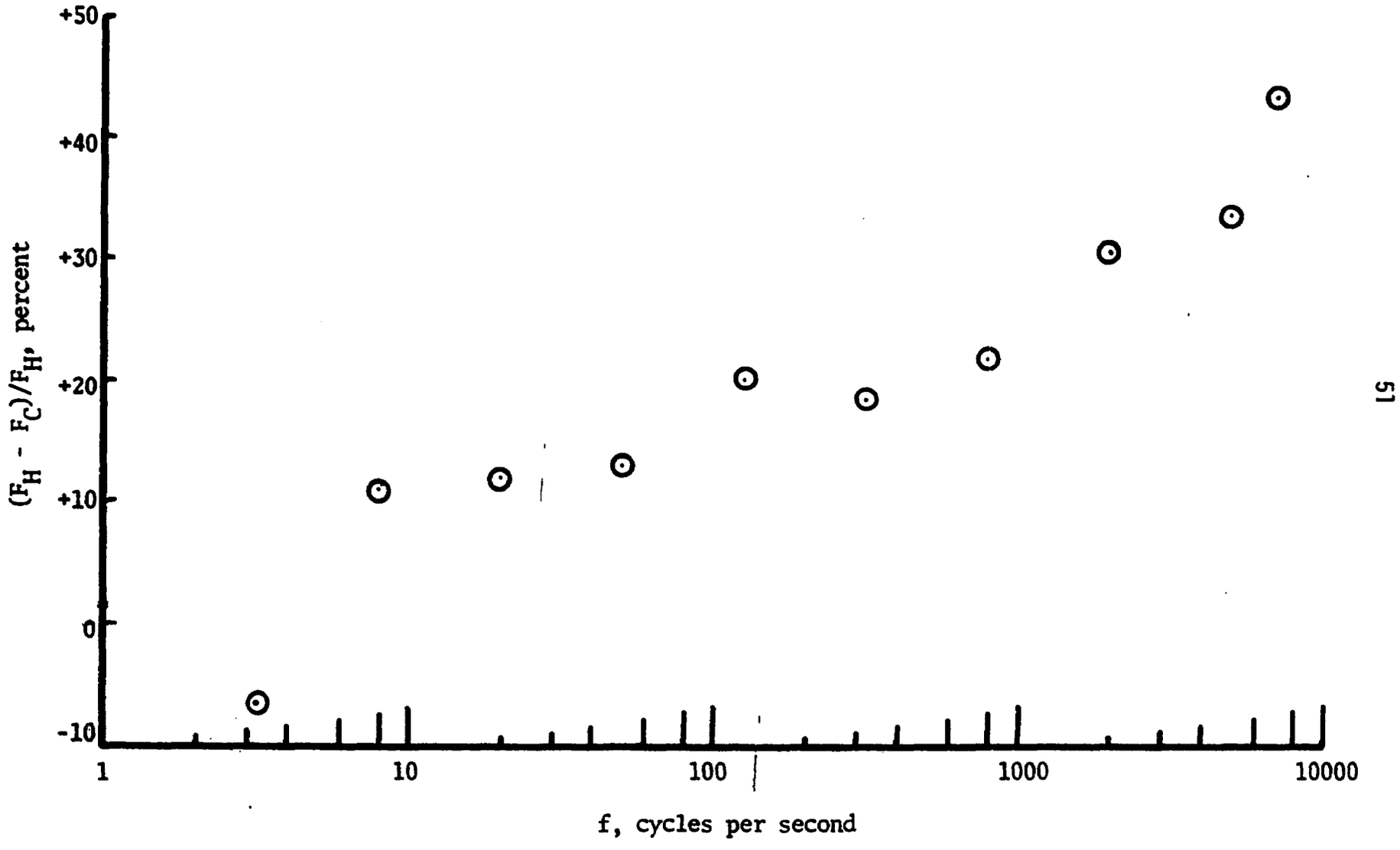

Figure 4.8. Percentage difference between hard plate and compliant plate spectra of turbulent energy at $y/\delta = 0.8$.

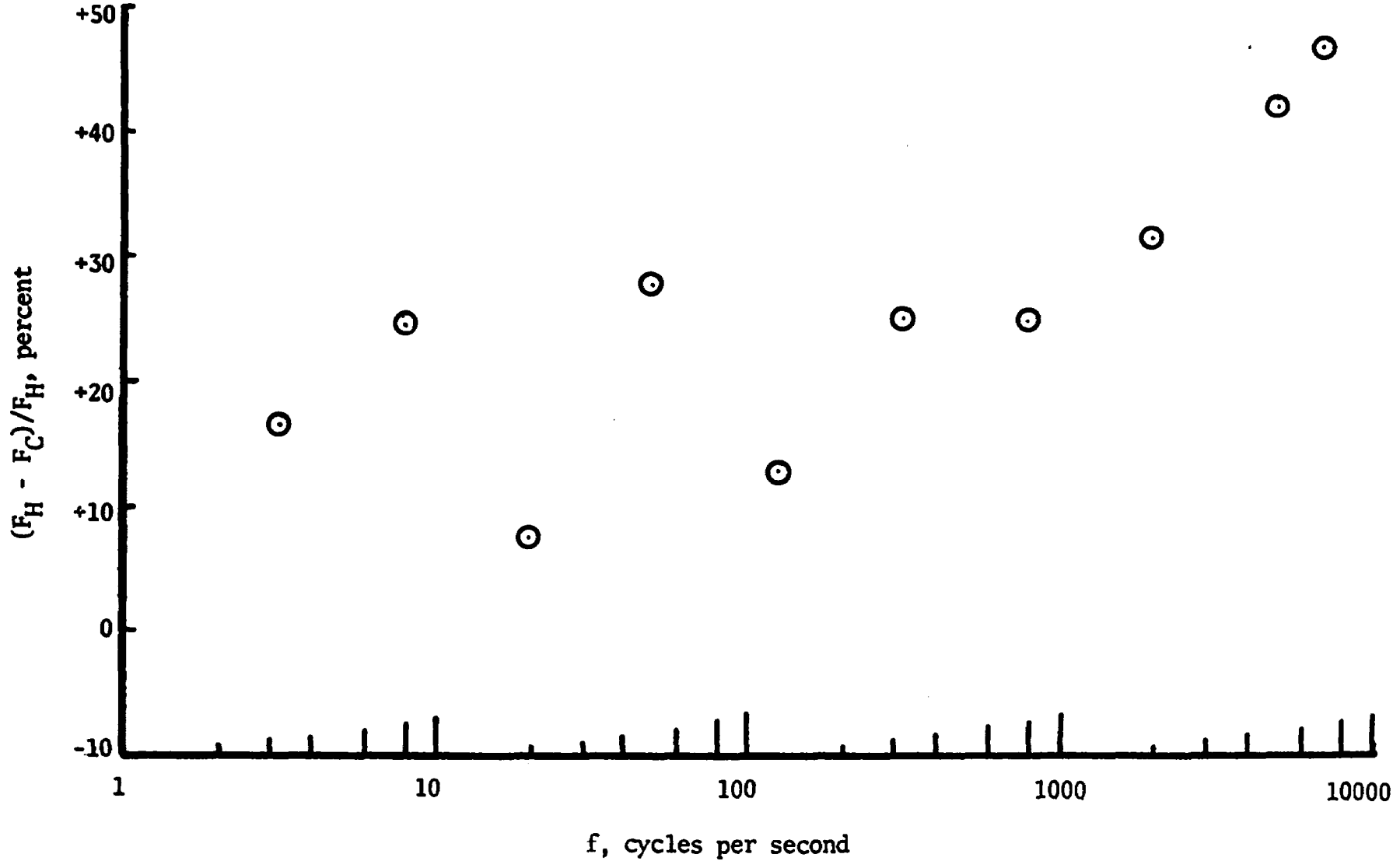

Figure 4.9 . Percentage difference between hard plate and compliant plate spectra of turbulent energy at $y/\delta = 1.0$.

$$\int_{-\infty}^{\infty} P\left(\frac{u}{u'}\right)\, d\left(\frac{u}{u'}\right) = 1 \qquad (4.1)$$

where P(u/u') is usually some number less than one. The probability density for the ideal homogeneous isotropic turbulent flow would then follow a Gaussian or normal distribution curve, since it has no preference for any specific direction.

The nonisotropic boundary layer turbulence dealt with here is compared with the Gaussian distribution curve in Figs. 4.10 to 4.17. Since hard plate probability distributions were not possible, as mentioned, the compliant plate is compared to the hard plate data of Klebanoff [22].

The minimum signal input allowance for the probability density analyzer was 1.25 volts for a probability density of 1. The output signal of the hot-wire anemometer was connected to the random signal voltmeter, which had an internal amplifier. This circuit was used to amplify the input signal to the probability density analyzer so that the signal was large enough to normalize. Two problems existed: that is, in order to amplify the signal sufficiently for normalization, amplitude distortion of the amplifier would appear, as illustrated in Figs. 4.16 and 4.17. Also, if the signal were not normalized,

$$\int_{-\infty}^{\infty} P\left(\frac{u}{u'}\right)\, d\left(\frac{u}{u'}\right) \neq 1 \qquad (4.2)$$

The probability distribution of u for $y/\delta = 0.0033$ is shown in Figs. 4.10 and 4.16. The input for Fig. 4.10 was not normalized and it is evident by comparison with the normal distribution curve. At $y/\delta = 0.05$, as shown in Fig. 4.11, the amplitude is approximately the same as that indicated by Klebanoff [22], but the position of maximum probability seems to have shifted to the right. In Fig. 4.12, at y/δ =

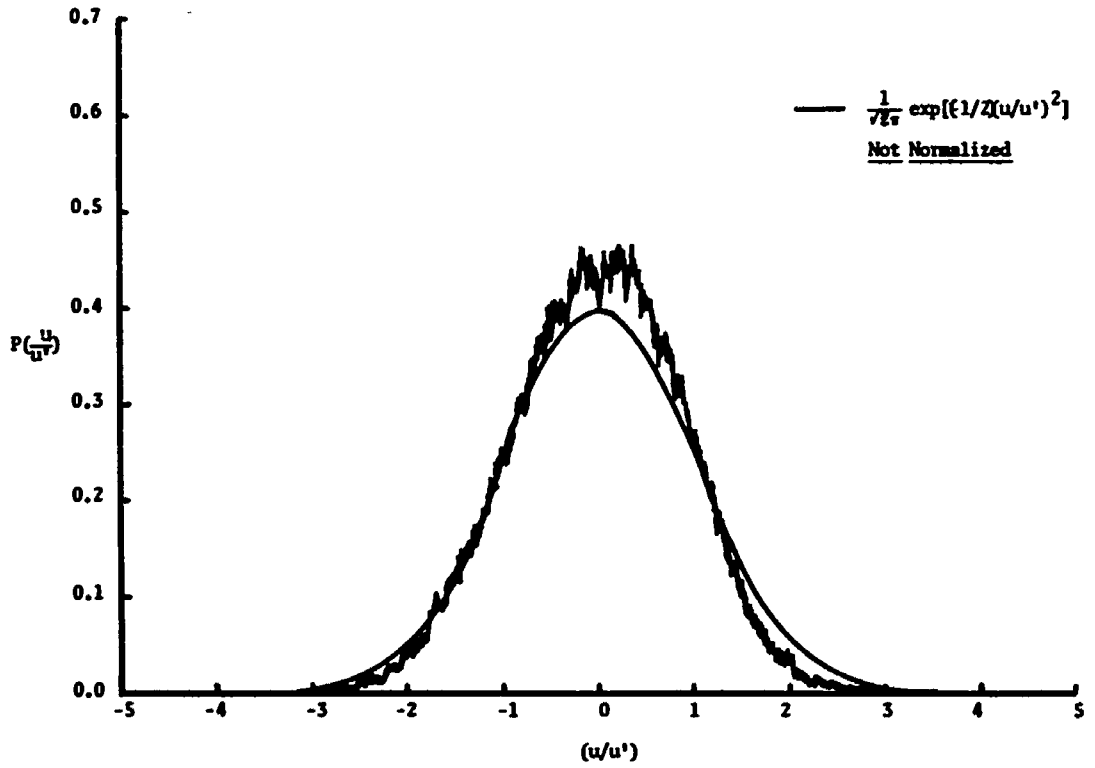

Figure 4.10. Distribution of probability density of u-fluctuation at $y/\delta = 0.0033$.

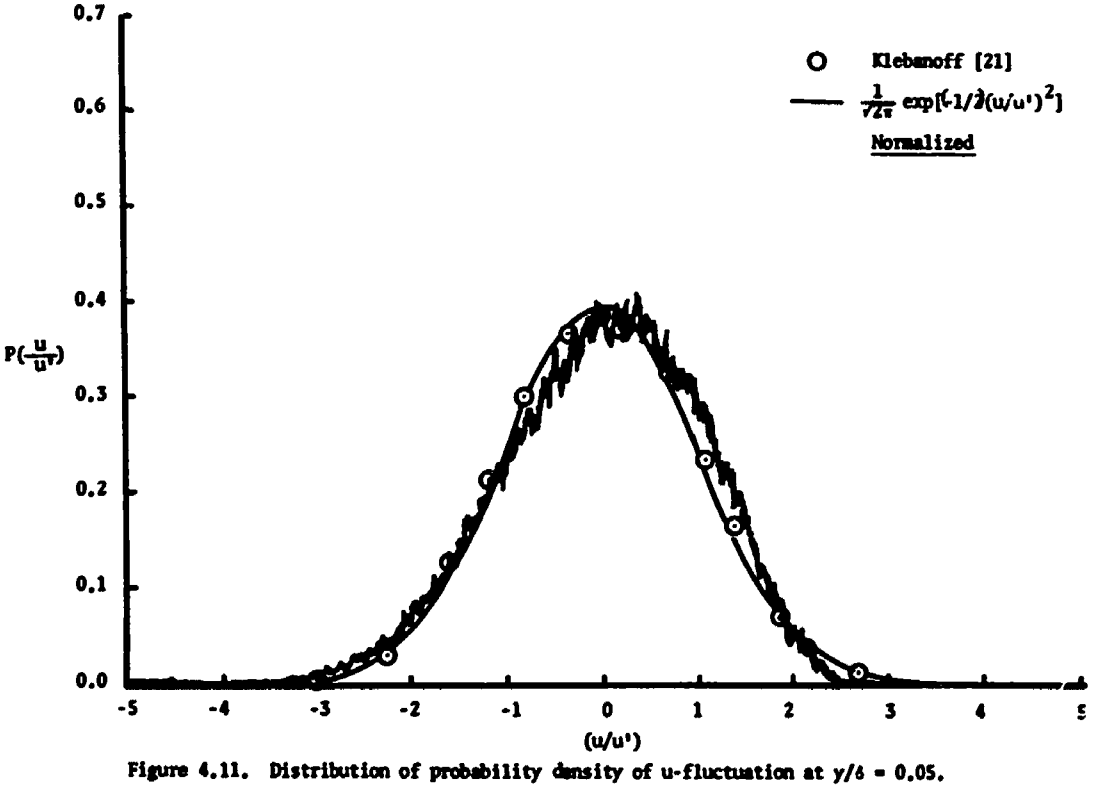

Figure 4.11. Distribution of probability density of u-fluctuation at $y/\delta = 0.05$.

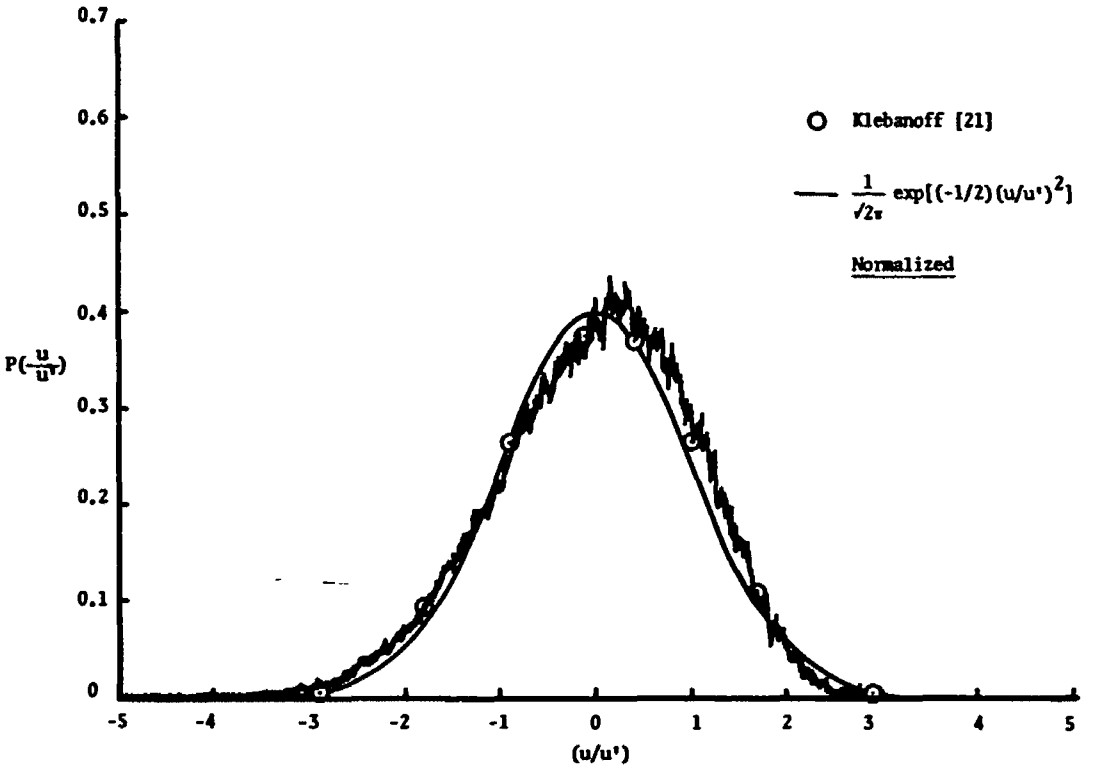

Figure 4.12. Distribution of probability density of u-fluctuations at $y/\delta = 0.20$.

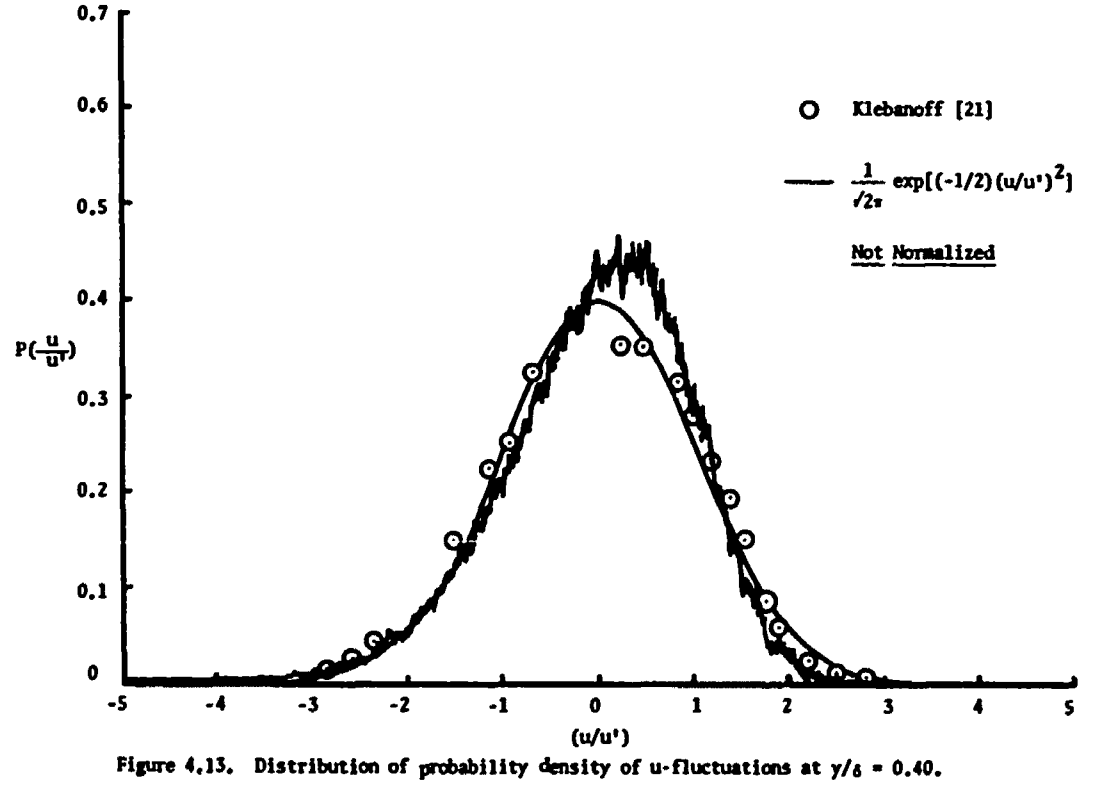

Figure 4.13. Distribution of probability density of u-fluctuations at $y/\delta = 0.40$.

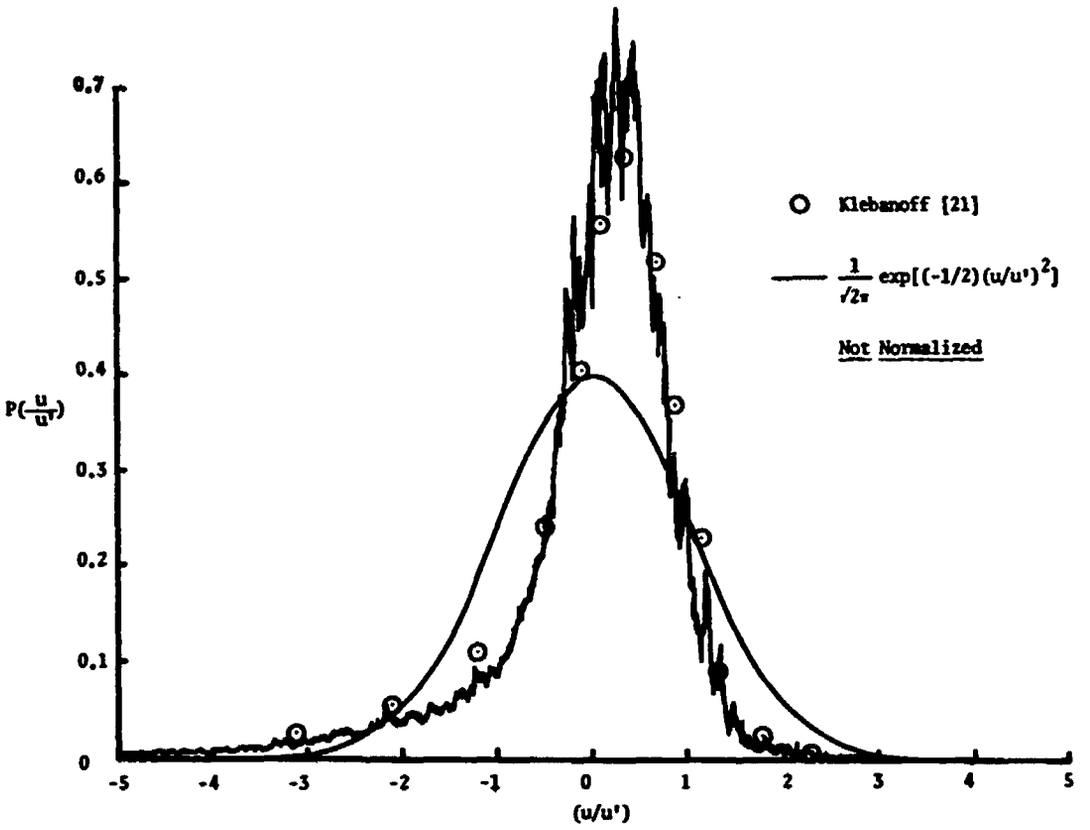

Figure 4.14. Distribution of probability density of u-fluctuation at y/δ = 0.80.

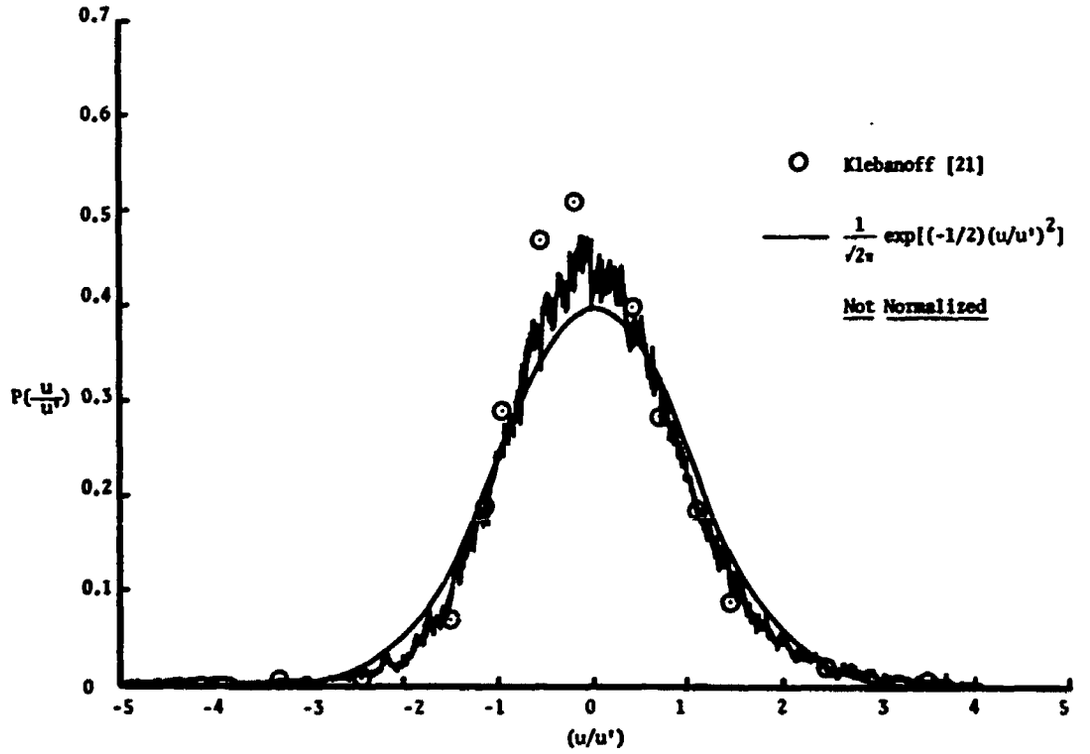

Figure 4.15. Distribution of probability density of u-fluctuation at y/δ = 1.0.

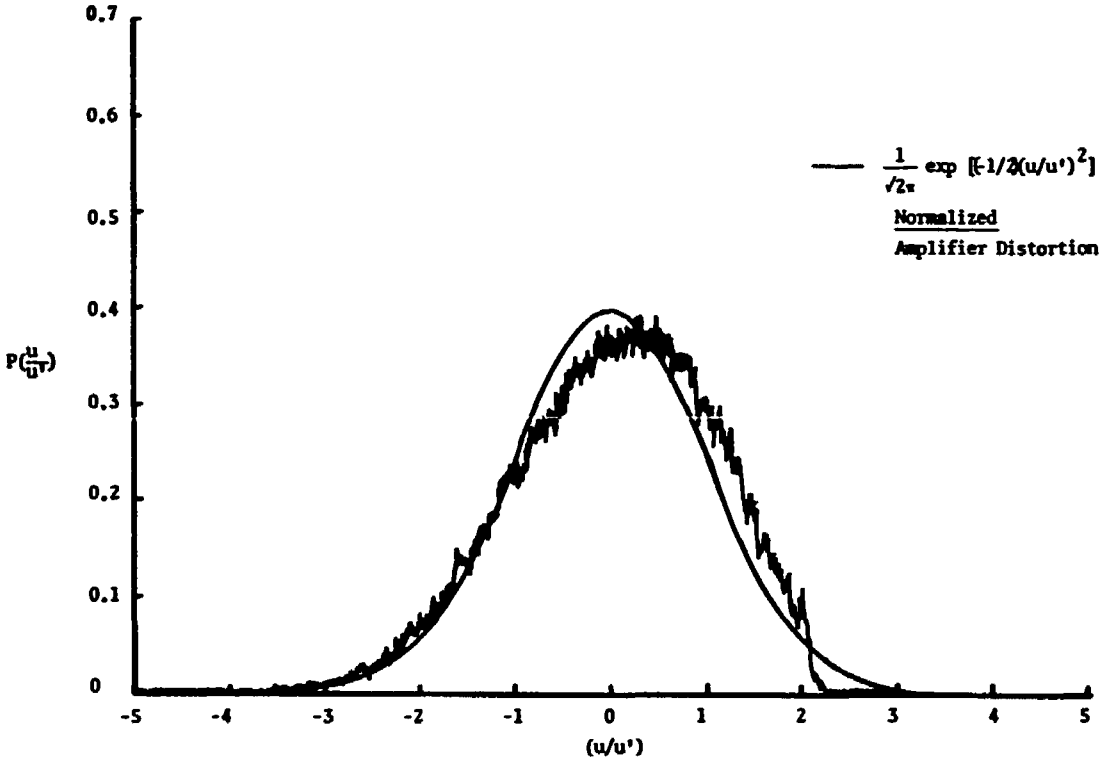

Figure 4.16. Distribution of probability density of u-fluctuation at y/δ = 0.0033.

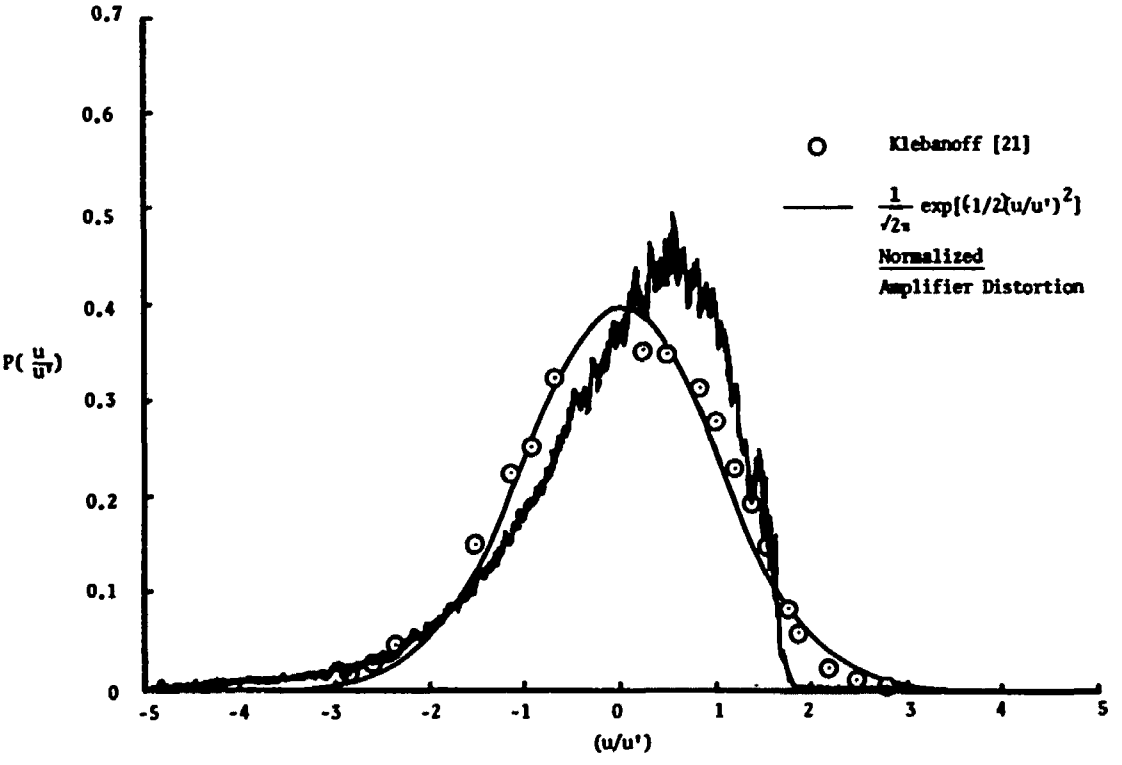

Figure 4.17. Distribution of probability density of u-fluctuation at y/δ = 0.40.

0.2, the amplitude has increased slightly, and the maximum probability point has shifted more to the right. For $y/\delta = 0.4$ (Figs. 4.13 and 4.17) greater amplitude and again a shift of the maximum to the right is indicated as compared to Klebanoff's data [22]. Although not normalized, the curves for $y/\delta = 0.8$ and 1.0 (Figs. 4.14 and 4.15, respectively) are very similar to Klebanoff's comparison points for the two positions. The plot at $y/\delta = 0.8$ appears to indicate more of a concentration of the signal around the midpoint and a decrease at the extreme points. Unfortunately, due to the short period of availability of the probability density analyzer, further experimentation with the instrument was not possible. Nevertheless, this investigator appreciated the opportunity to obtain the data presented here.

The measurement of the dissipation derivative was accomplished by the procedures described in the instrumentation section of this chapter and in Appendices C and D. A decrease in the $\overline{(\partial u/\partial x)^2}$ and $\overline{(\partial v/\partial x)^2}$ derivatives was measured throughout the boundary layer profile. The $\overline{(\partial w/\partial x)^2}$ derivative decreased between $y/\delta = 0.2$ to $y/\delta = 0.0125$, where it measured higher than hard plate data. The hard plate versus compliant plate data for the three derivatives are indicated in Figs. 4.18 and 4.19.

The other two derivatives, $\overline{(\partial u/\partial y)^2}$ and $\overline{(\partial u/\partial z)^2}$, obtained by the correlation coefficients as described in Appendix D, are illustrated in Figs. 4.20 and 4.21 for specific values of Δy and Δz used. Due to the geometry of the experimental arrangement, the minimum Δz distance was 4/64 inches. At this wire separation distance, good correlation was not possible since the scale of turbulence was apparently much smaller. Therefore, a comparison of $\overline{(\partial u/\partial y)^2}$ and $\overline{(\partial u/\partial z)^2}$ is made in Fig. 4.20 for

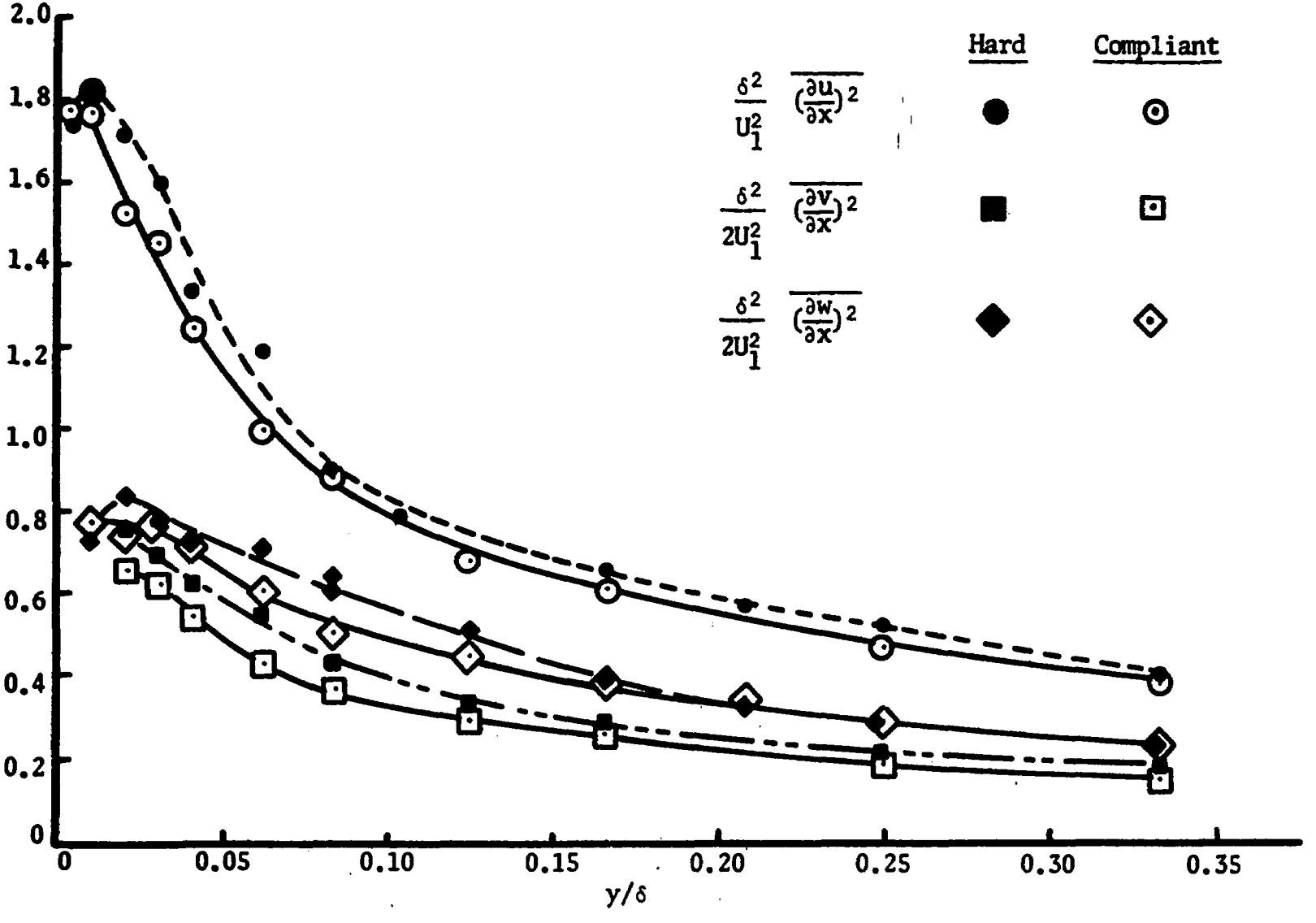

Figure 4.18. Distribution of dissipation derivatives, hard plate versus compliant plate near the wall.

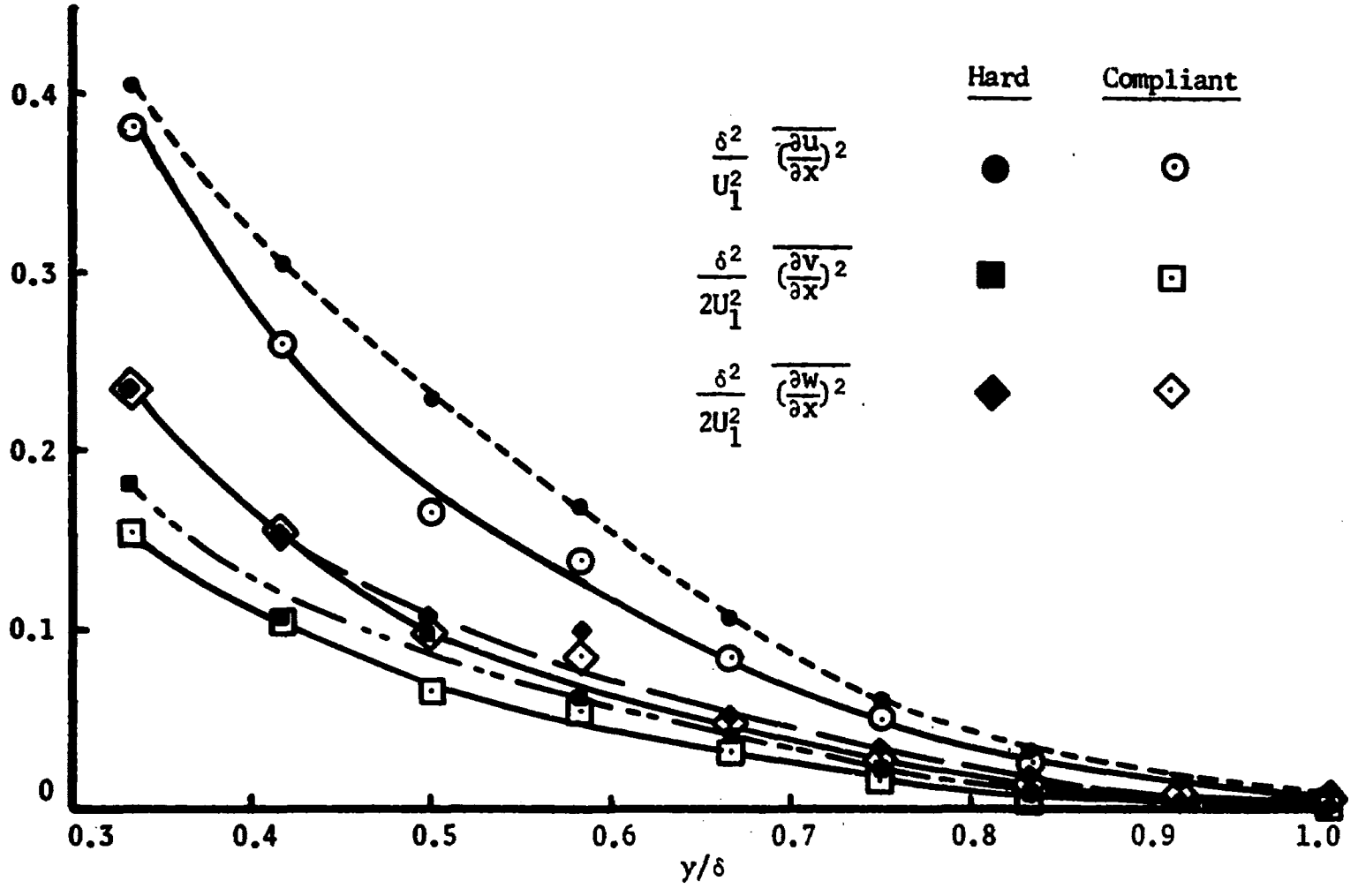

Figure 4.19. Distribution of dissipation derivatives, hard plate versus compliant plate, away from wall.

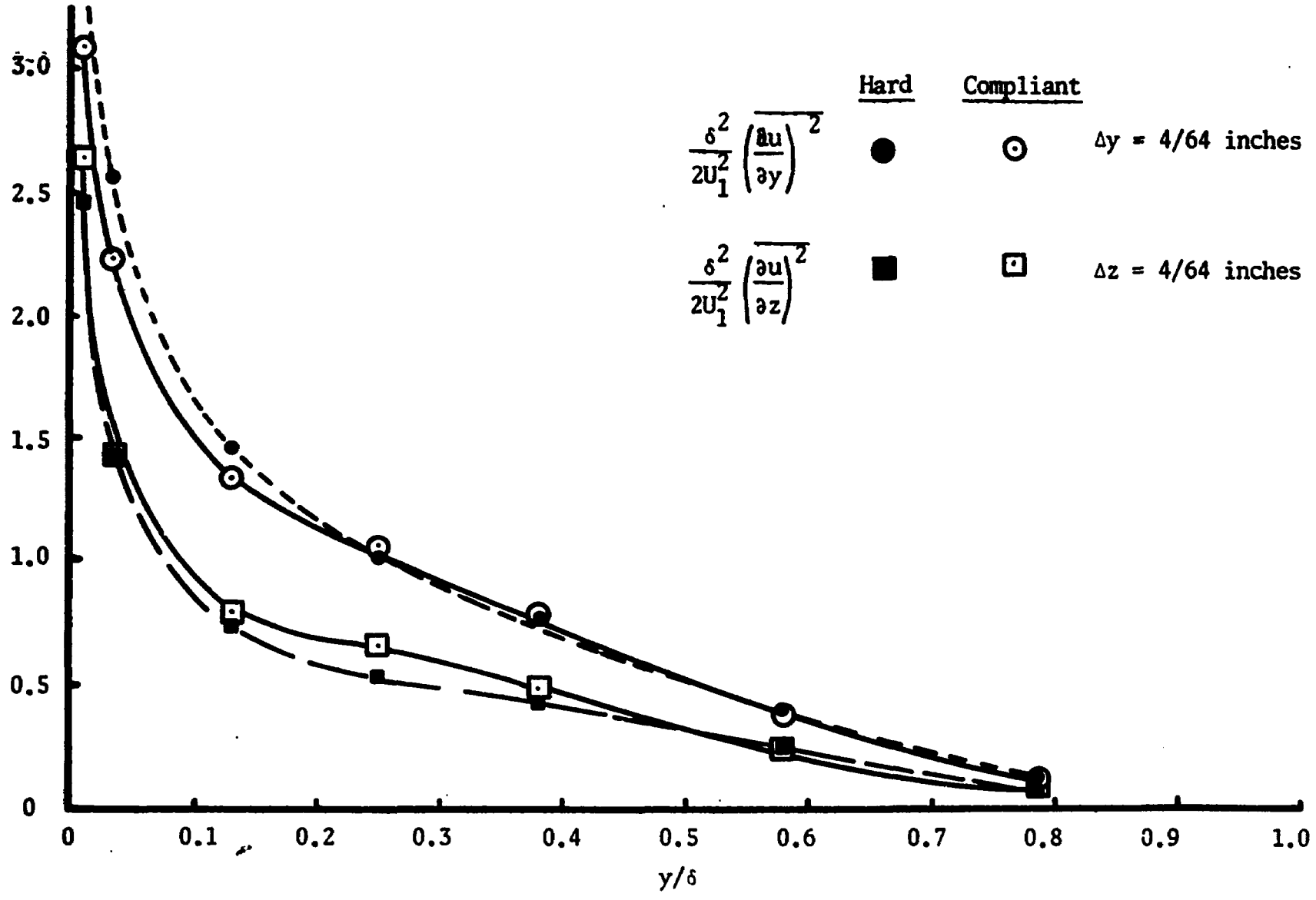

Figure 4.20. Dissipation derivatives for an interval of 0.0625 inches.

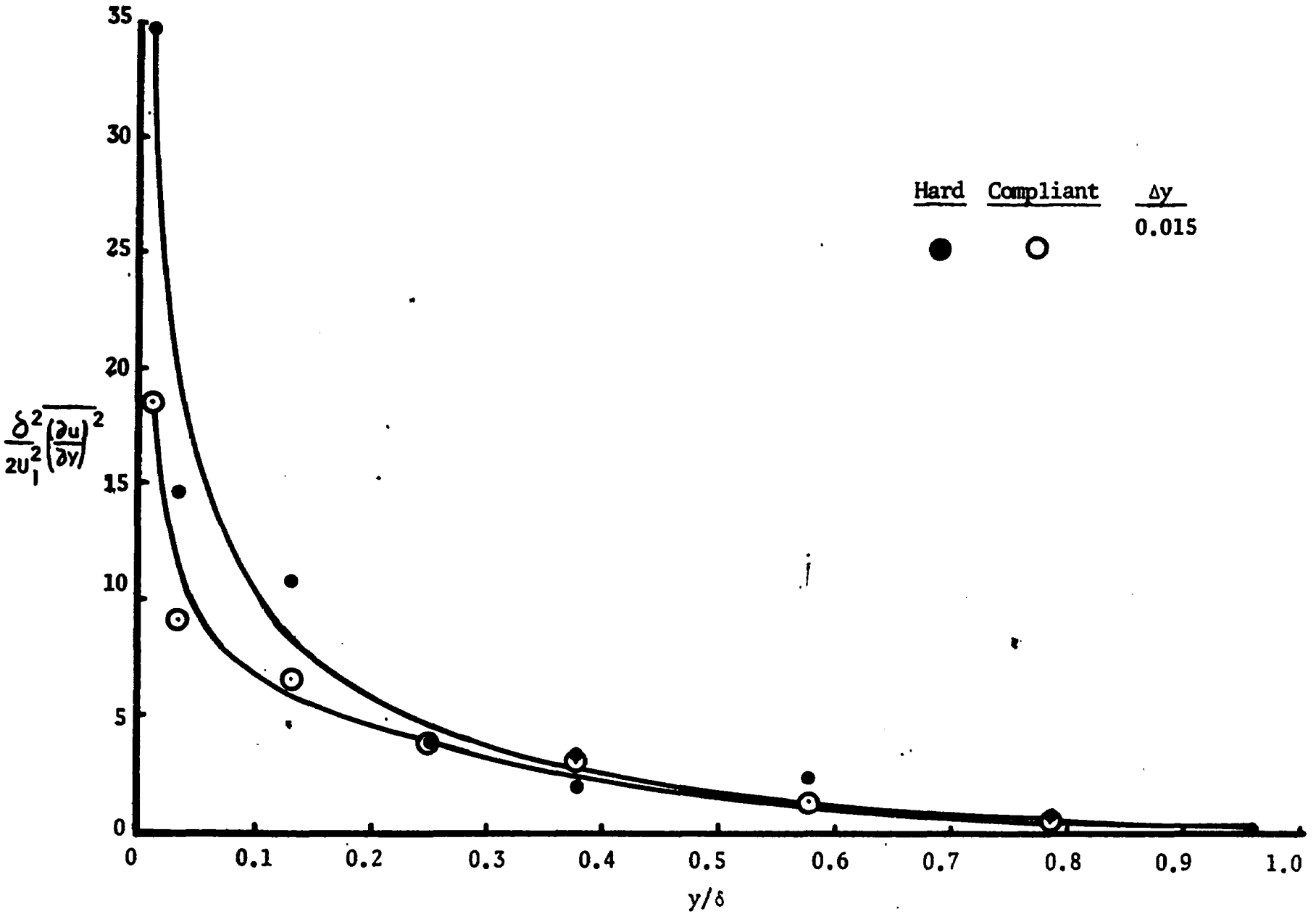

Figure 4.21. Dissipation derivative for an interval of 0.015 inch.

a $\Delta z = \Delta y = 0.0625$ inches to speculate on possible trends for $\overline{(\partial u/\partial z)^2}$ at smaller Δz values. The $\overline{(\partial u/\partial y)^2}$ data indicated a decrease below hard plate data both at the $\Delta y = 0.015$ inch (Fig. 4.21) and $\Delta y = 0.0625$ inch (Fig. 4.20) separation distances. From Fig. 4.20 and previous indications of the z component characteristics, one could speculate that the $\overline{(\partial u/\partial z)^2}$ compliant plate data would not decrease for smaller z values. The only interval distance common to both Δz and Δy was 4/64 inches, so that a better interpolation was not possible. As shown in Fig. 4.22, for most of the larger separation distances, the hard plate values for the dissipation derivative $\overline{(\partial u/\partial z)^2}$ are below the compliant plate values. This is a strong indication that the same could be true for smaller wire separation distances. However, this assumption appears to be somewhat invalid in view of Fig. 4.23 for the $\overline{(\partial u/\partial y)^2}$ values. For large wire separation distances hard plate data were sometimes below the compliant plate values and then well above compliant data from small wire spacing distances. Therefore, the behavior of the $\overline{(\partial u/\partial z)^2}$ term for closer wire spacing is rather inconclusive and only the comparison data obtained at a spacing of 4/64 inches are used for further discussion.

Discussion of Data

The mean velocity profile was replotted in the form of the "universal velocity distribution law" from Prandtl's mixing length hypothesis [35].

$$U^* = A \ln y^* + \beta \qquad (4.3)$$

where $U^* = U/U_\tau$

$y^* = y U_\tau / \nu$

$A = 1/\kappa$

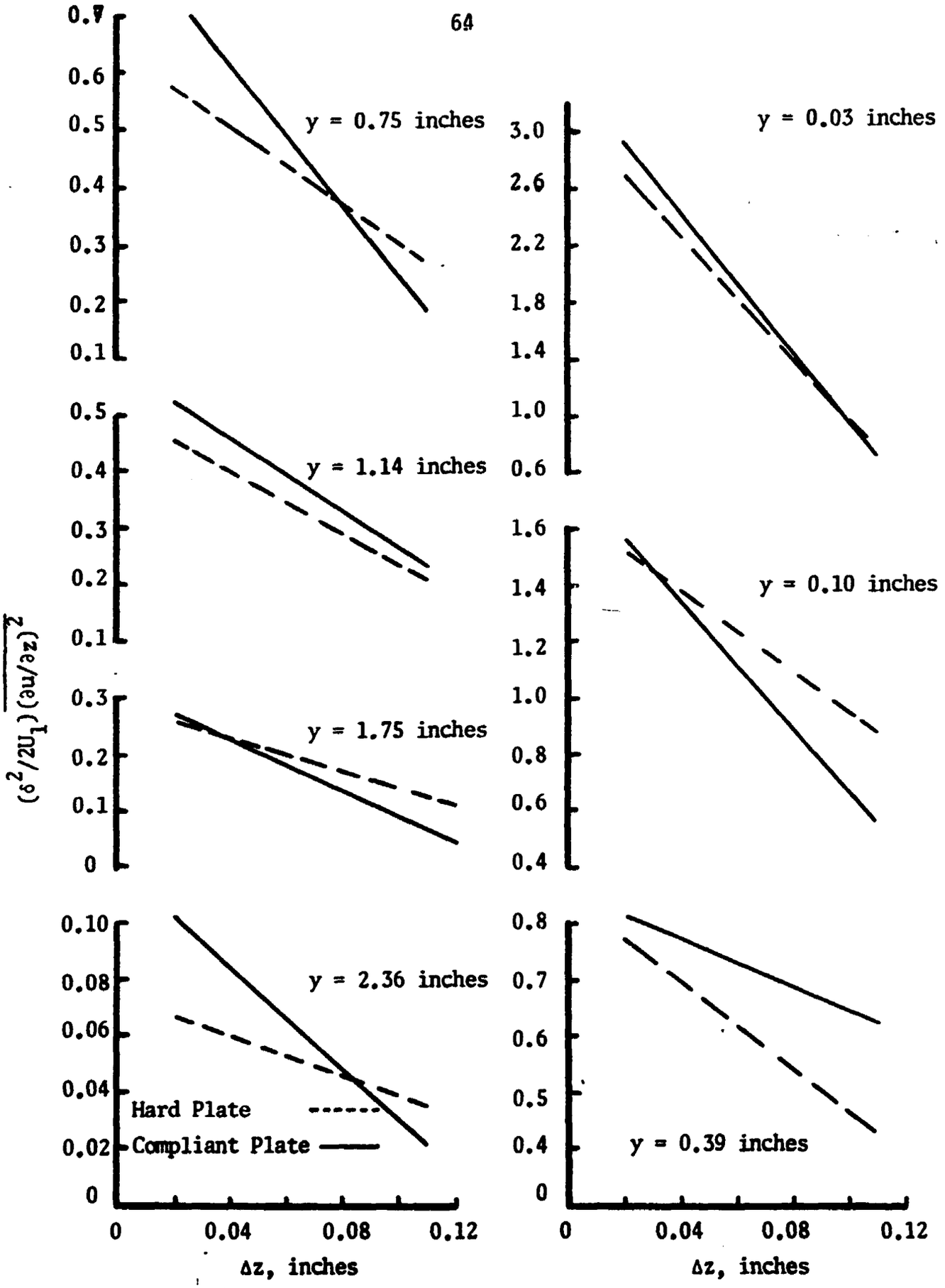

Figure 4.22. Dissipation derivative versus wire separation distance.

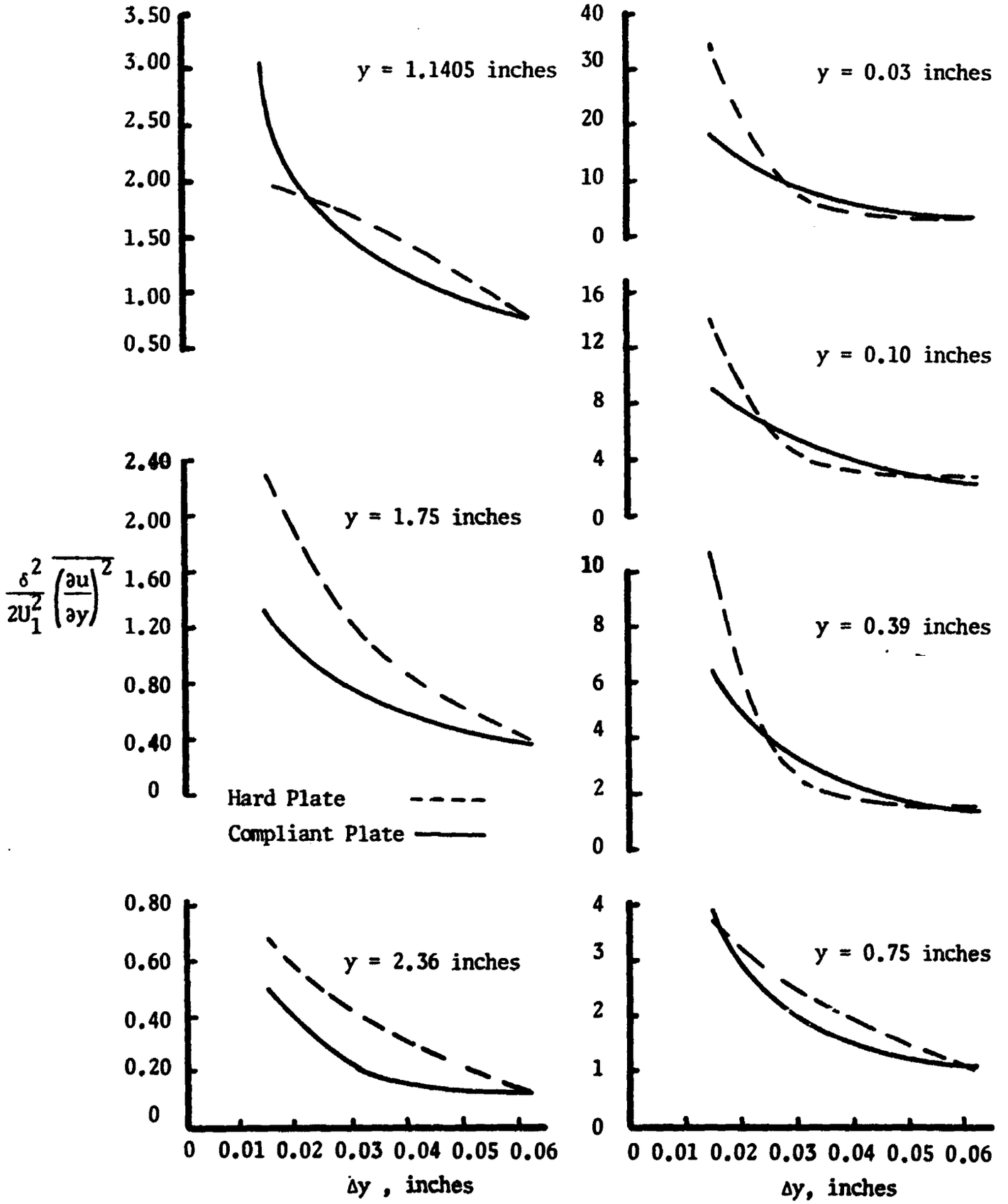

Figure 4.23. Dissipation derivative versus wire separation distance.

β = constant

$l = \kappa y$ = "mixing length"

$$U_\tau = \sqrt{\tau_o/\rho} = \left[\left(\frac{\overline{uv}}{U_1^2}\right)_{wall}\left(\frac{U_1^2}{2}\right)\right]^{1/2}$$

The hard plate data coincide extremely well with the upper logarithmic portion of the profile using the constants suggested by Clauser [36] where A = 2.44 and B = 4.9 in Fig. 4.24. A wake region, which deviates from the logarithmic line, is indicated for y^* values greater than 1000 ($y/\delta > 0.36$). The hard plate data points approaching the wall layer (viscous sublayer) are above the universal velocity profile line of Clauser [36] (eq. 4.3) rather than below. All data points were rechecked and as yet no explanation can be given for this.

The compliant plate data (shown in Fig. 4.24) were offset above the hard plate data as dictated by the universal velocity distribution law for lower wall shear stress. A line drawn through the compliant data was found to be parallel to the hard plate data. The compliant data line corresponded to a value of B = 8.4. Since the lines were parallel, A remained constant and therefore indicated little or no change in the proportionality between mixing length, l, and wall distance. The compliant data indicate a wake region beginning at y^* greater than 500. This corresponds to a y/δ value of 0.21. Therefore, the wake region appears to have increased in size.

Although the mixing length theories have lost some significance, it is interesting to note the changes in l over the height of the boundary layer. In Fig. 4.25, plotted with data from Fenter [33], the mixing length, l, over the entire boundary layer is not the same for the compliant and hard plates, as calculated by Prandtl's mixing length hypothesis

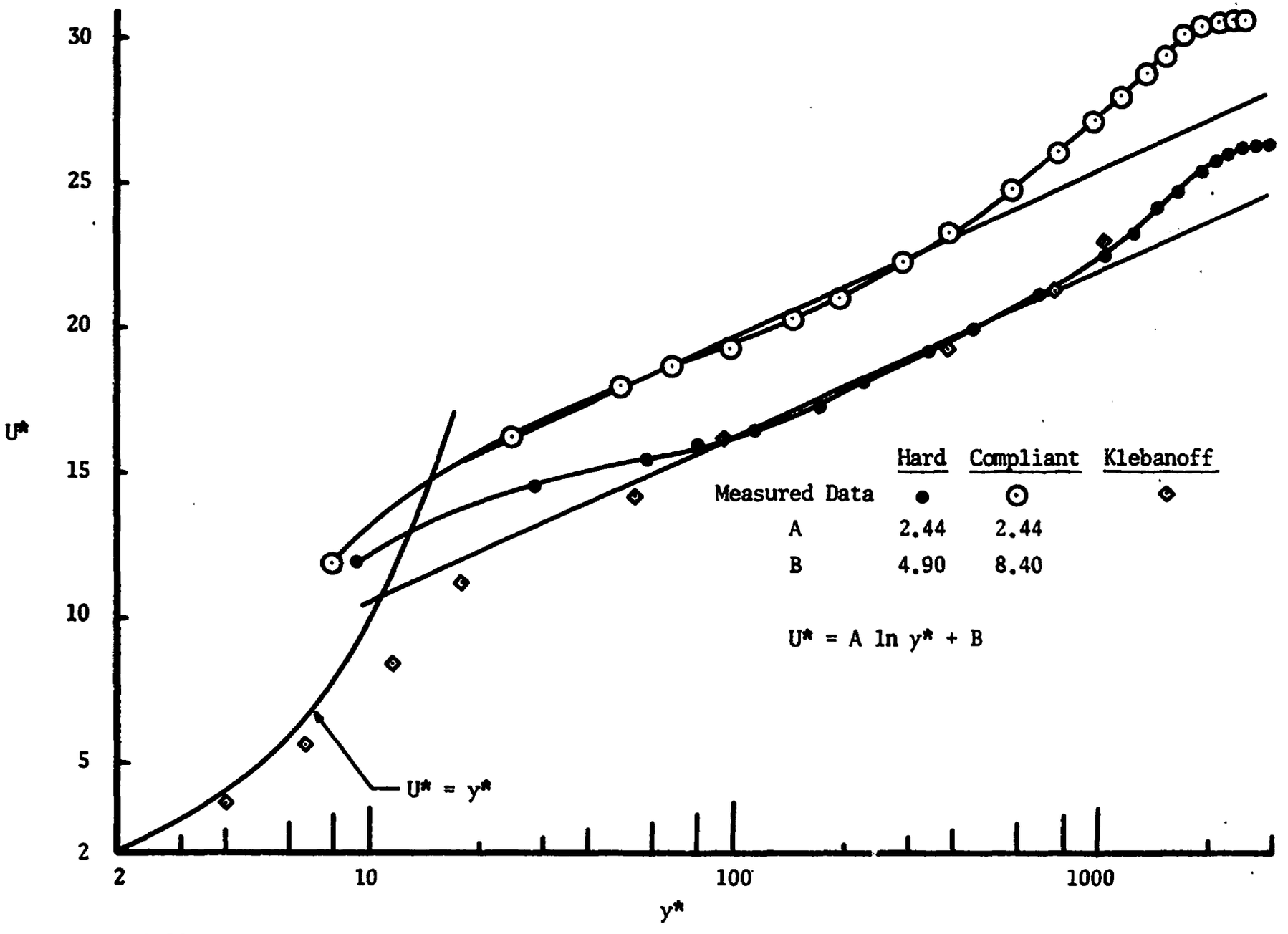

Figure 4.24. Comparison of hard plate and compliant plate by the "Universal Velocity Distribution Law."

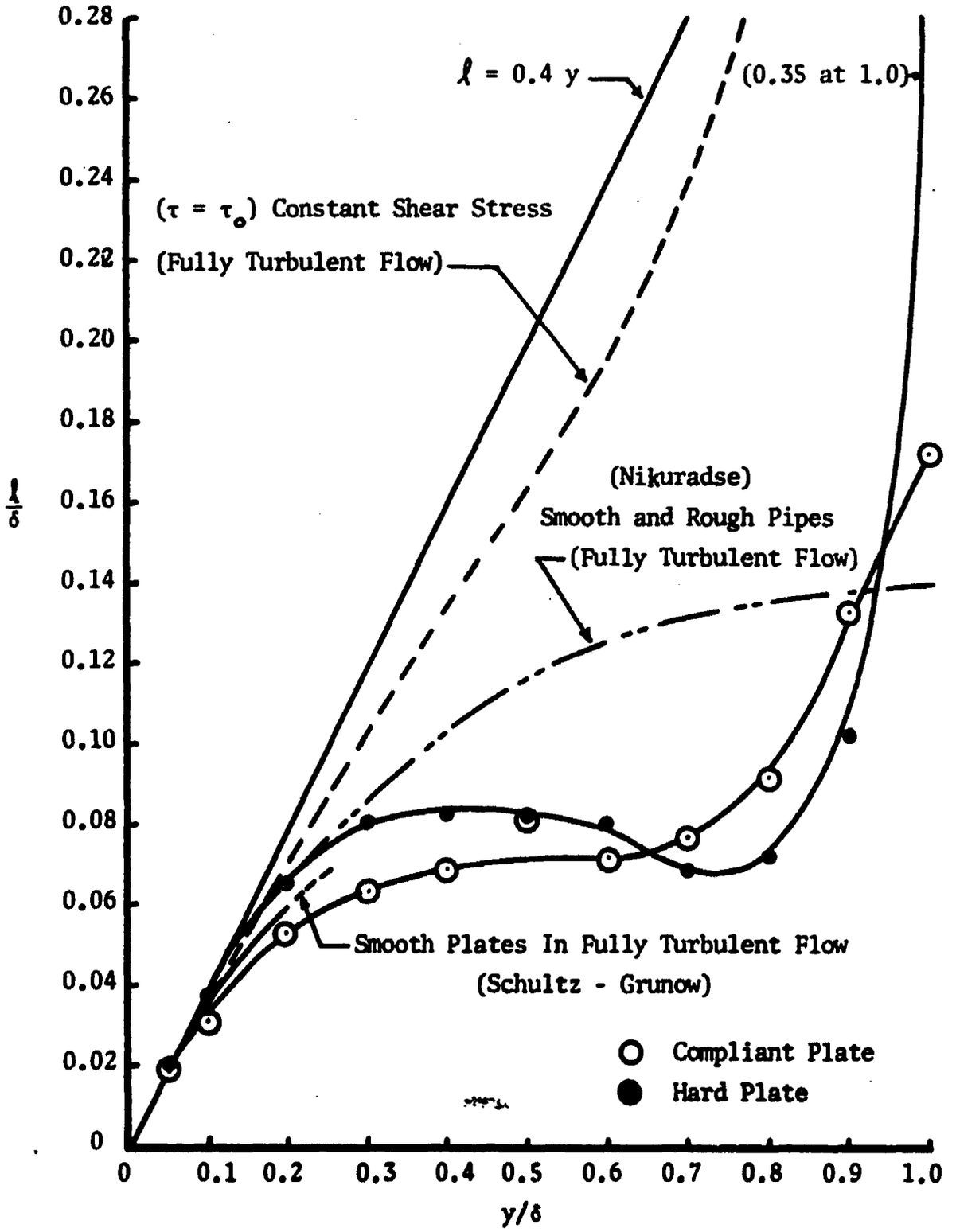

Figure 4.25. Mixing length distribution

[35].

$$l^2 = (dU/dy)^2/(-\overline{uv}) \qquad (4.4)$$

Both compliant plate and hard plate data approach the linear relation for l and y at values less than $y/\delta = 0.1$. In Fig. 4.24, for some values less than $y/\delta = 0.1$, $300 > y^* > 770$, the logarithmic portion of the plot is valid. Therefore, one can conclude from Figs. 4.24 and 4.25, that the proportionality between mixing length and wall distance, in the fully turbulent region, does not appear to change for compliant plate and hard plate.

Von Karman's similarity hypothesis [37] concerning the structure of turbulence requires that a constant ratio exist between the turbulent shear stress distribution and the turbulent kinetic energy distribution. The shear correlation coefficient actually gives this ratio. In Fig. 4.26, the distribution for the shear correlation coefficient is given for compliant and hard plate, with a comparison of Klebanoff's data [22]. Over the range of $y/\delta = 0.05$ to 0.9, the compliant and hard plate data maintain a relatively constant value.

In Fig. 4.27, the ratio of the shear stress to the total turbulent kinetic energy ($\overline{q^2}$) is compared for the hard plate and compliant plate. The ratio for the hard plate more nearly approaches a constant across the range from $y/\delta = 0.1$ to $y/\delta = 0.8$ than does the compliant curve. However, both are acceptable as an indication that the von Karman similarity hypothesis is valid over a large portion of the boundary layer.

The direct viscous dissipation (W_μ) and production (Pr) of turbulent energy are compared in Fig. 4.28. It is evident from Fig. 4.28 that the direct viscous dissipation is negligible for $y/\delta > 0.02$ in com-

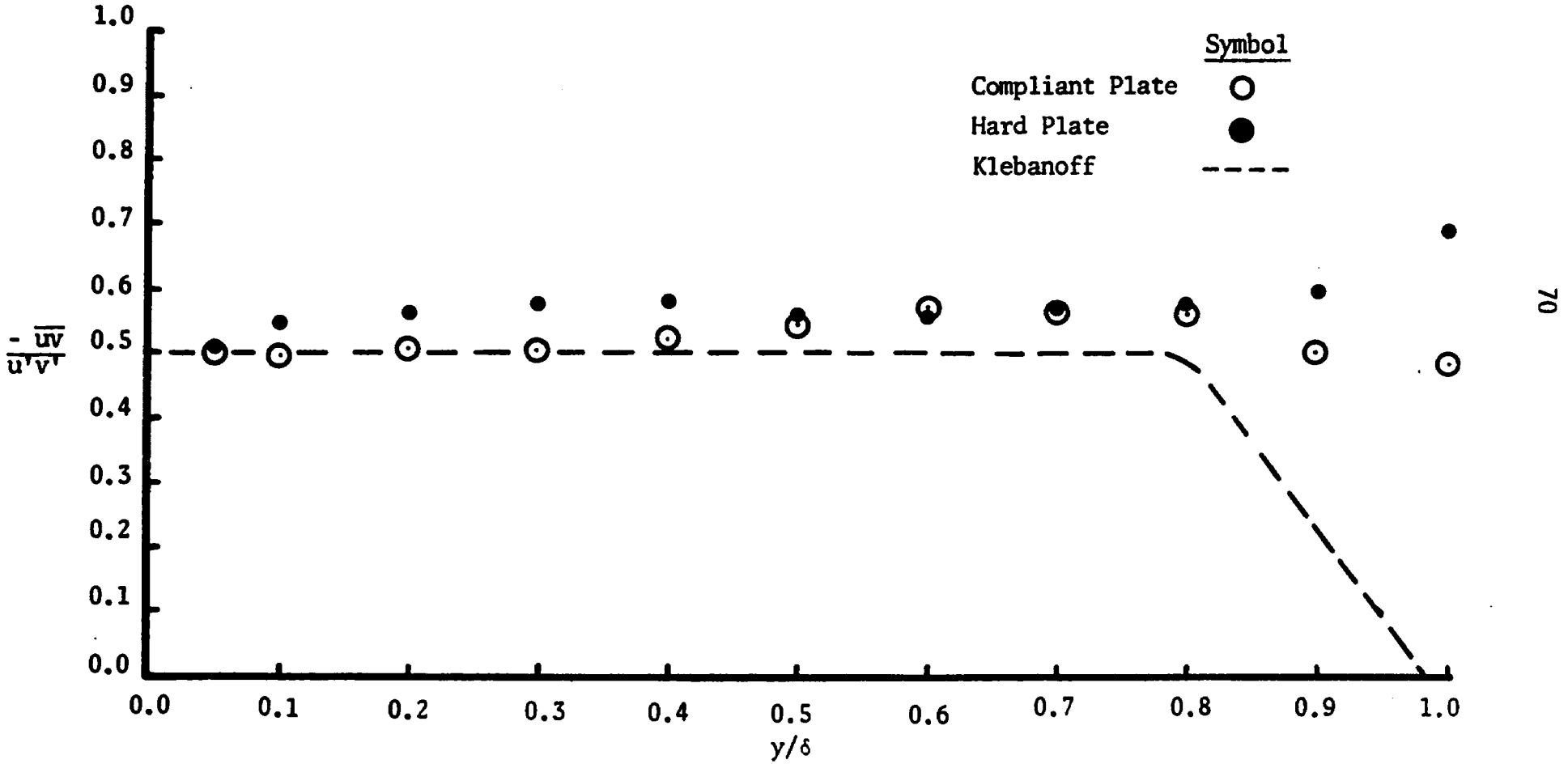

Figure 4.26. Distribution of the shear correlation coefficient.

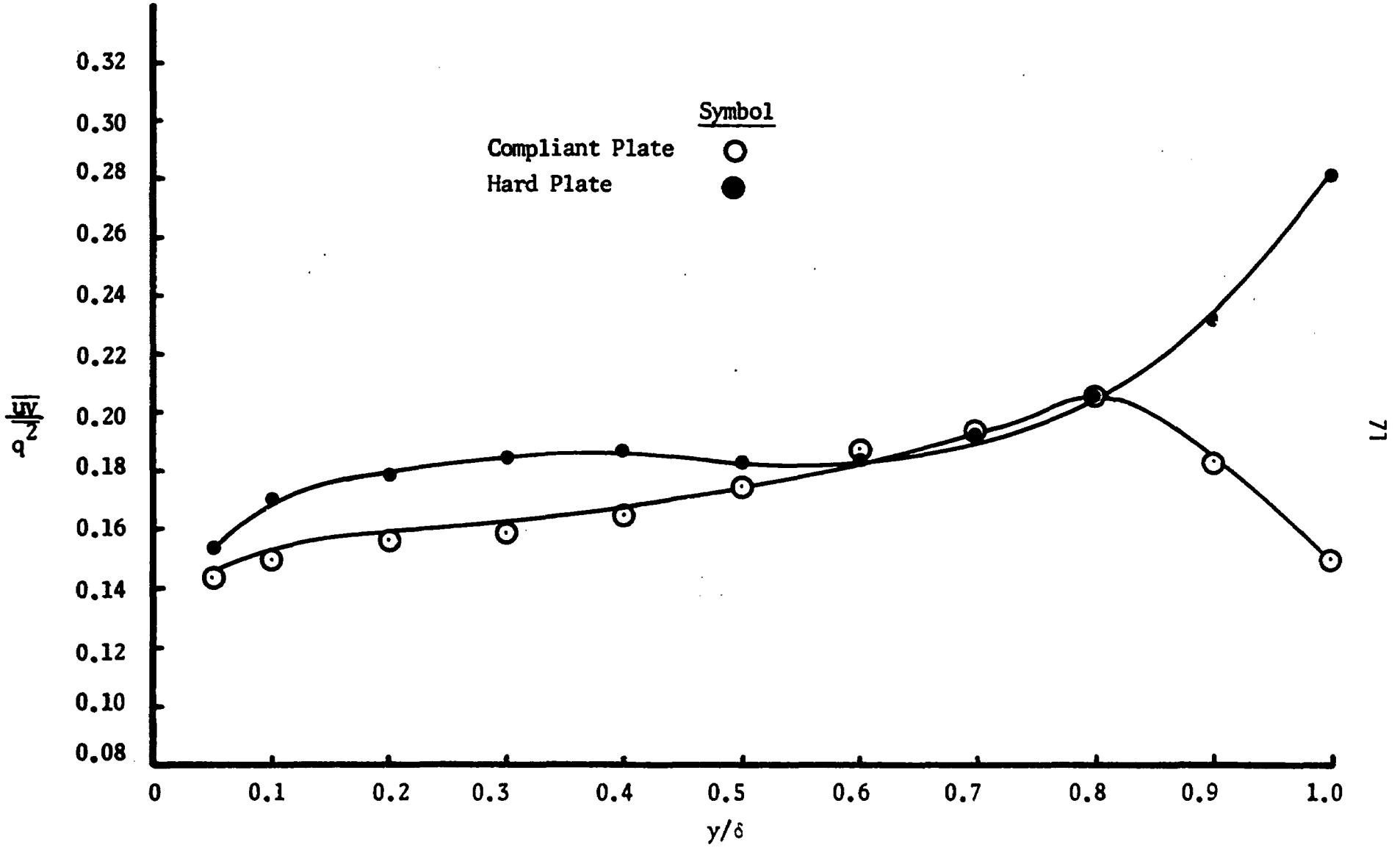

Figure 4.27. Distribution of the ratio of turbulent shear stress and complete turbulent kinetic energy.

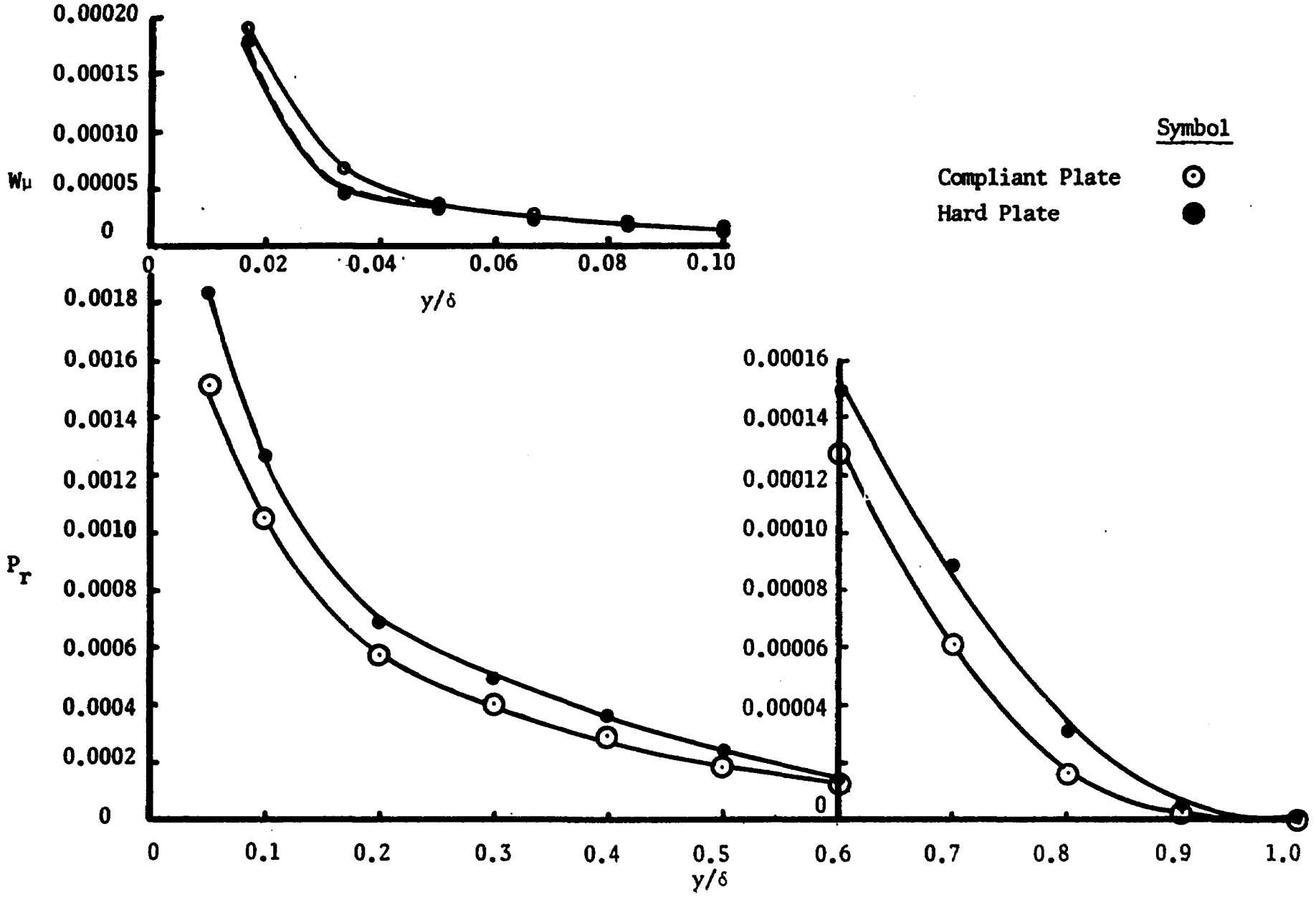

Figure 4.28. Comparison of turbulent energy production and direct viscous dissipation as the wall is approached, for hard plate and compliant plate.

parison with the production term. However, from Klebanoff's same plot [22] in Fig. 4.29, it is possible to show that direct viscous dissipation is negligible for $y/\delta > 0.01$. In Fig. 4.28, it is interesting to note that the direct viscous dissipation for the compliant plate is slightly above the hard plate curve; however, the compliant plate turbulent energy production is considerably less than hard plate.

The turbulent energy production term is compared with the dissipation derivative term in Fig. 4.30. The hard plate production agrees quite well with Klebanoff's curve.

The five measured dissipation derivatives were combined together to form W_2'. The magnitude of W_2' for the compliant plate was less than that for the hard plate over the measurable portion of the boundary layer. The decrease was most pronounced from $y/\delta < 0.2$, as shown in Fig. 4.30.

Klebanoff's term for the dissipation derivatives, W_2, contained all nine derivatives as described in the first section of Chapter III. Since only the first five, $\overline{(\partial u/\partial x)^2}$, $\overline{(\partial u/\partial y)^2}$, $\overline{(\partial u/\partial z)^2}$, $\overline{(\partial v/\partial x)^2}$ and $\overline{(\partial w/\partial x)^2}$, were measurable, Klebanoff approximated the remaining four by the following isotropic relations.

$$\begin{aligned} \overline{(\partial u/\partial y)^2} &= 2\overline{(\partial v/\partial y)^2} = \overline{(\partial w/\partial y)^2} \\ \overline{(\partial u/\partial z)^2} &= \overline{(\partial v/\partial z)^2} = 2\overline{(\partial w/\partial z)^2} \end{aligned} \tag{4.5}$$

The addition of the four remaining terms to W_2 by means of these relations contributed to the major difference between W_2 and W_2' shown in Fig. 4.30. Part of the difference is attributed to the differentiation amplification problems described in Chapter III. Therefore,

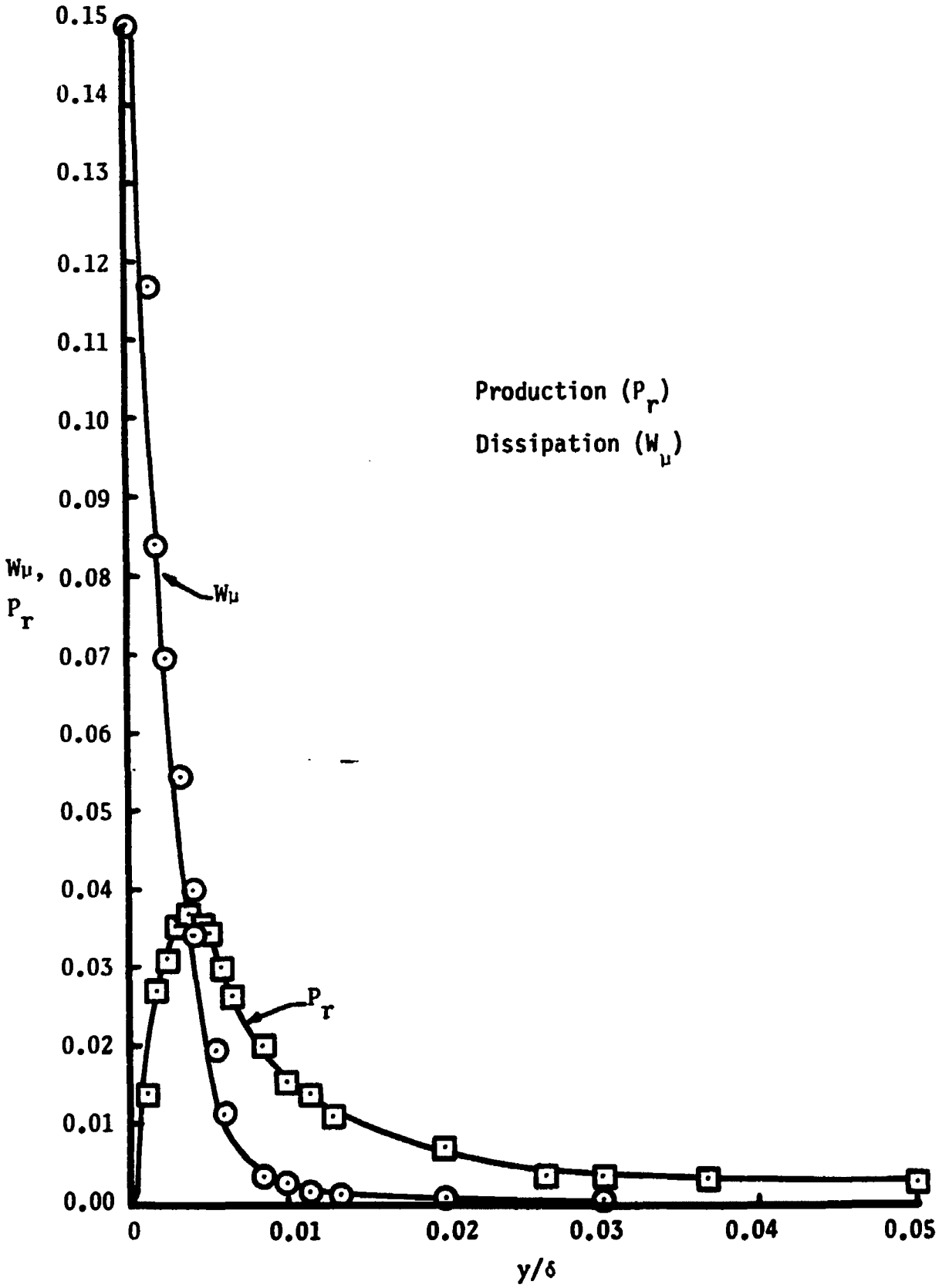

Figure 4.29. Comparison of direct viscous dissipation with production of turbulent energy near the wall (Klebanoff [22]).

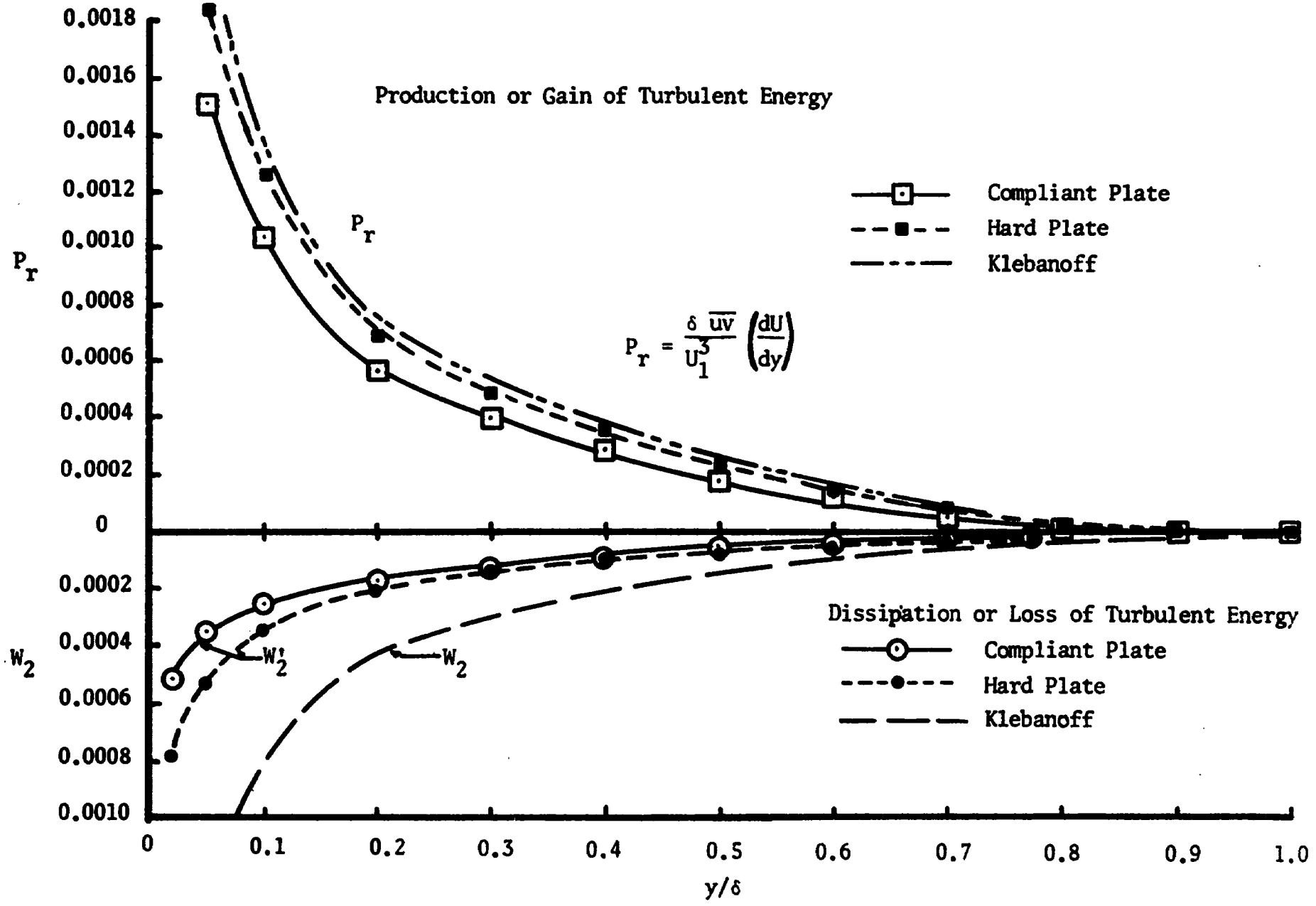

Figure 4.30. Comparison of production and dissipation of turbulent energy for hard plate and compliant plate.

to minimize the errors, only the measured derivatives were compared for hard plate and compliant plate. The second derivative term of the dissipation was found to be negligible for most of the boundary layer except for the region approaching the wall.

The convection of turbulent energy, C_1, is plotted in Fig. 4.31. The hard plate curve shows remarkably good agreement with Klebanoff's plot except at the small y/δ values. In all cases, the magnitude of the convection term from the compliant plate is less than for the hard plate even when the terms are positive. However, in comparison with the production and dissipation terms the convection term is practically negligible over most of the boundary layer.

In discussing the turbulent motion, the transfer of energy is of primary concern. Some insight into the process of the transfer of energy from large eddies to smaller ones can be gained by examining the spectral distribution of turbulent energy. As described by Tchen [38], the flow of energy from larger eddies to smaller eddies corresponds to a dissipation due to three different types of momentum exchanges. The momentum exchanges occur between the molecular motion and the turbulent motion, between the small and large eddies, and between the turbulent and mean motion. The basic concept of this idea is that the energy enters the spectrum through the large eddies from the mean motion and is transferred through the spectrum to the smaller eddies where it is finally dissipated by the molecular motion.

Frequency (f) can be written in terms of the wave number (k_1) by the relation, $k = 2\pi f/U$. The low wave numbers correspond to the large eddies and the higher wave numbers to the smaller eddies, since

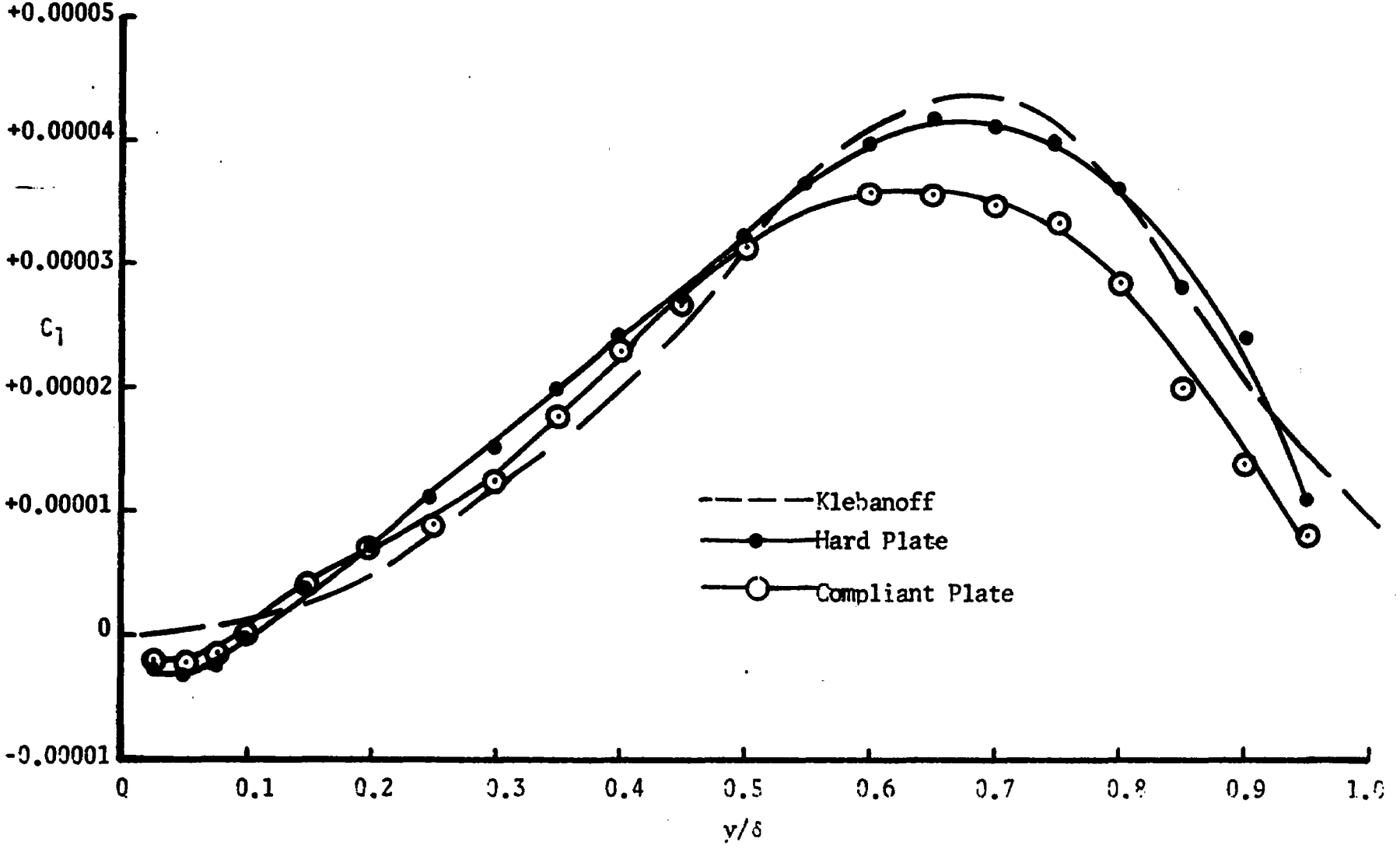

Figure 4.31. Convection of turbulent energy comparison for compliant plate, hard plate and Klebanoff's data.

the eddy size is inversely proportional to the wave number. In Figs. 3.8 and 3.9, it was shown that the trend was for the higher wave numbers to possess a greater percentage of the turbulent energy as the rigid surface was approached.

In Figs. 4.4 to 4.9, it is evident that there is less energy at the higher wave numbers for the compliant plate although the percentage decrease in turbulent energy becomes less as the compliant plate is approached. A strong indication that the energy has increased at the low numbers and greatly decreased at higher wave numbers is given by Figs. 4.4, 4.6, and 4.7. On the basis of the previous discussion, this would indicate that the energy transfer has been hindered and thus a decrease in the momentum exchange has possibly occurred.

Runstadler, Kline, and Reynolds' [23] definition of the turbulent flow could provide the basis for an elementary explanation of the mechanism involved in this apparent reduced turbulent energy transfer. In the last part of Chapter I, a description of the flow mechanism was given according to Runstadler, et al. This description states that turbulence transport to the outer flow regions is maintained by the outwards and downstream convection of small-scale turbulence within large-scale turbulence, or eddies, which originate at the wall. This ejection of eddies, which is in the form of low momentum streaks, has a strong interaction in the fully turbulent region outside the wall layer which results in the production and dissipation of turbulence. The loss of energy via dissipation in and ejections from the wall layer is resupplied by the flow of high momentum fluid toward the rigid wall, which reaches the wall more uniformly than the concentrated ejected eddies.

It is speculated that, with the compliant wall acting as an effective uniform energy absorber, some of the available energy of the high momentum inflow is decreased by the compliant wall-fluid interaction. This would result in a weaker interaction of the injected momentum-deficient fluid in the fully turbulent region where maximum turbulence intensities are measured. As noted in Fig. 4.2, the largest decrease in the turbulence intensity levels for compliant plate were measured at the peak level. The outward v' and downstream u' components of turbulence were noted to have the largest decrease with a possible increase near the wall of the w' component. Accordingly, this would precipitate a reduced shear stress, $-\overline{uv}$, as indicated in Fig. 4.3. Then the decrease in ejected fluid reaction potential would logically reduce the production and dissipation of turbulent energy, as noted in Fig. 4.28, for the compliant wall condition.

Further insight into this mechanism of fluid motion could be gained by the study of the velocity correlation coefficients R_x, R_y, and R_z. The measurements of the correlation coefficients R_y and R_z were not extensive enough to yield conclusive results for a basic eddy flow description.

CONCLUSIONS

The following conclusions and recommendations have been obtained from the experimental study of the turbulent boundary layer characteristics of flow with a zero pressure gradient over a compliant surface.

Concluding Remarks

The compliant surface was found to influence favorably the characteristics of turbulent flow as measured by a hot-wire anemometer system and accessory equipment. After several choices of the membrane-damper configuration, a 0.001 inch thick polyvinyl-chloride membrane with a dry polyurethane foam substrate was used as a compliant plate, extended over the full length of the "boundary layer development" plate.

Turbulence intensity reductions for the u' and v' components of approximately 10 per cent and 6 per cent, respectively, were measured. When compared with the hard plate, the w' component indicated a slight reduction until the wall was approached where an increase was measured.

The Reynolds stress for the compliant plate had a 20-25 per cent decrease over most of the boundary layer compared with the rigid plate condition.

The spectrum of the u' component of turbulence over the compliant surface indicated a significant decrease of energy at the higher frequencies or wave numbers. As the wall was approached, the low fre-

quency, low wave number part of the spectrum contained an increase in energy, while the higher frequencies still had a reduced energy level compared with the hard plate.

The probability density of the u-fluctuation appeared to be the same as the hard plate comparison data of Klebanoff [22]. Results were inconclusive due to lack of extensive measurements.

A reduction in the production, convection, and dissipation of turbulent energy for the compliant surface was indicated when compared with the identically measured hard plate values.

Possibly the above reductions are caused by the compliant wall acting as an effective uniform energy absorber which would reduce the interaction of fluid motion in the fully turbulent region of the boundary layer.

Recommendations for Future Research

In order to gain further insight into the characteristics of turbulent flow over a compliant wall, additional investigations are needed. Extensive measurements of the dissipation derivatives with a more sophisticated differentiation circuit would be helpful. Also, a device needs to be designed for obtaining more precise correlation coefficient measurements, since this is a critical factor in describing the eddy flow structure.

Lower free stream turbulence levels could possibly be obtained in the tunnel used for this investigation if an entrance section were designed to precede the honeycomb system and vibration in the drive unit were eliminated.

LIST OF REFERENCES

1. Kramer, M.O., "Boundary Layer Stabilization by Distributed Damping," Readers Forum, Journal of the Aerospace Sciences, Vol. 27 (1960), p. 68.

2. Kramer, M. O., "Boundary Layer Stabilization by Distributed Damping," Journal of American Society of Naval Engineers, Vol. 72, February, 1960, pp. 25-33.

3. Kramer, M. O., "The Dolphin's Secret," Journal of the American Society of Naval Engineers, Vol. 73, February, 1961, pp. 103-107.

4. Benjamin, T.B., "Effects of a Flexible Boundary on Hydrodynamic Stability," Journal of Fluid Mechanics, Vol. 9 (1960), p. 513.

5. Hains, F.D., "Preliminary Results on Boundary-Layer Stability on a Flexible Plate," AIAA Journal, Vol. 3, No. 4, April, 1965, pp. 775-776.

6. Landahl, M.T., "On the Stability of a Laminar, Incompressible Boundary Layer over a Flexible Surface," Journal of Fluid Mechanics, Vol. 13 (1962), pp. 609-632.

7. Kaplan, R.E., "The Stability of Laminar Incompressible Boundary Layers in the Presence of Compliant Boundaries," ASRL Technical Report No. 116-1, Aeroelastic and Structures Research Lab., Massachusetts Institute of Technology, June, 1964.

8. Laufer, J. and Maestrello, L., "The Turbulent Boundary Layer over a Flexible Surface," Boeing Co., Transport Div., Document D6-9708, December, 1965.

9. Benjamin, T.B., "Fluid Flow with Flexible Boundaries," Paper presented at Eleventh International Congress of Applied Mechanics, Munich, Germany, 1964.

10. Smith, L.L., "An Experiment of Turbulent Flow in a Pipe with a Flexible Wall," Master of Science Thesis, Department of Chemical Engineering, University of Washington, 1963.

11. Gregory, N. and Love, E.M., "Progress Report on an Experiment of the Effect of Surface Flexibility on the Stability of Laminar

Flow," Aeronautical Research Council Current Papers, C.P. No. 602, Ministry of Aviation, London, England, 1962.

12. Karplus, H.B., "Turbulent Flow Transition Near Solid and Flexible Boundaries," IIT Research Institute, Report No. IITRI 1205-4, 1963.

13. Pelt, R., "A Preliminary Investigation of Surface Damping Effects on Fluid Flow Through Flexible Tubes," Ph.D. Dissertation, Dept. of Chemical Engineering, University of Pittsburgh (1964).

14. Von Winkel, W.A. and Barger, J.E., "Evaluation of a Boundary Stabilization Coating," Journal of the Acoustical Society of America, Vol. 33, (1961), p. 836.

15. Fisher, D.H. and Blick, E.F., "Turbulent Damping by Flabby Skins", J. Aircraft, Vol. 3, No. 2, March-April, 1966, pp. 163-164.

16. Looney, R.W. and Blick, E.F., "Skin Friction Coefficients of Compliant Surfaces in Turbulent Flow", Journal of Spacecraft and Rockets, Vol. 3, No. 10, October, 1966, pp. 1562-1564.

17. Blick, E.F. and Walters, R.R., "Turbulent Boundary-Layer Characteristics of Compliant Surfaces," Journal of Aircraft, Vol. 5, No. 1, January-February 1968, pp. 11-16.

18. Walters, R.R., "Experiments on the Aerodynamic Turbulent Damping of a Flat Membrane with Fluid Substrate," Master of Engineering Thesis, School of Aerospace and Mechanical Engineering, University of Oklahoma (1966).

19. Laufer, J., "Investigation of Turbulent Flow in a Two-Dimensional Channel," NACA Report 1053, 1951.

20. Blick, E.F., "The Theory of Skin Friction Reduction By A Compliant Coating in a Turbulent Boundary", Symposium on Viscous Drag Reduction, LTV Research Center, Dallas, Texas, September 24-25, 1968 (Plenum Press, 1969).

21. Gyorgyfalvy, D., "The Possibilities of Drag Reduction by the Use of Flexible Skin," Presented at AIAA 3rd Aerospace Sciences Meeting, Los Angeles, California, June, 1966.

22. Klebanoff, P.S., "Characteristics of Turbulence in a Boundary Layer with Zero Pressure Gradient," NACA Report No. 1247, 1955.

23. Runstadler, P.W., Kline, S.J., and Reynolds, W.C., "An Experimental Investigation of the Flow Structure of the Turbulent Boundary," Thermosciences Division Report No. MD-8, Department of Mechanical Engineering, Stanford University, 1966.

24. Townsend, A.A., "The Structure of the Turbulent Boundary Layer," Proc. of the Cambridge Philosophical Society, Vol. 47, part 2, April, 1951, pp. 375-395.

25. Pankhurst, R.C. and Holder, D.W., Wind-Tunnel Technique, London: Pitman and Sons, Ltd., 1952.

26. Uberoi, M.S., "Effect of Wind-Tunnel Contraction on Free-Stream Turbulence," Journal of Aeronautical Sciences, Vol. 23, August, 1956, pp. 754-764.

27. Dryden, H.L.and Schubauer, G.B., "The Use of Damping Screens for the Reduction of Wind-Tunnel Turbulence," Journal of Aeronautical Sciences, Vol. 14, April, 1947, pp. 221-228.

28. Pope, A., Wind-Tunnel Testing, Ed. 2, New York: John Wiley and Sons, Inc., 1961.

29. Model HWB-3 Hot Wire Anemometer, Theory and Instructions, Flow Corporation Bulletin, No. 37D, Cambridge, Massachusetts, 1963.

30. Gessner, F.B., "A Method of Measuring Reynolds Stresses with a Constant Current, Hot Wire Anemometer," ASME, Page 64-WA/FE-34, 1964.

31. Klebanoff, P.S. and Diehl, Z.W., "Some Features of Artificially Thickened Boundary-Layers With Zero Pressure Gradient," NACA Report No. 1110, 1952.

32. Dhawan, S., "Direct Measurements of Skin Friction," NACA Technical Note No. 2567, 1952.

33. Fenter, F.W., "The Turbulent Boundary Layer on Uniformly Rough Surfaces at Supersonic Speeds," Vought Research Center Report No. RE-E9R-2, Dallas, Texas, 1959.

34. Smith, R. and Blick, E.F., "Experimental Turbulent Skin Friction Coefficients of Compliant Surfaces on Flat Plates," Unpublished paper, University of Oklahoma, Norman, Oklahoma, 1968.

35. Schlichting, H., Boundary Layer Theory, New York: McGraw-Hill Book Company, Inc., 1960.

36. Clausen, F.H., "Turbulent Boundary Layers in Adverse Pressure Gradients," Journal of the Aeronautical Sciences, Vol. 21, February, 1954, pp. 91-108.

37. Hinze, J.O., Turbulence, New York: McGraw-Hill Book Company, Inc., 1959.

38. Tchen, C.M., "On the Spectrum of Energy in Turbulent Shear Flow," Journal of Research, Research Paper Report No. RP2388, National Bureau of Standards, Vol. 50, No. 1, January 1953, pp. 51-62.

39. Peterson, A.P.G., Handbook of Noise Reduction, General Radio Company, West Concord, Mass., 1967.

40. Keast, David N., Measurement in Mechanical Dynamics, New York: McGraw-Hill Book Company, Inc., 1967.

41. Townsend, A.A., "The Measurement of Double and Triple Correlation Derivatives in Isotropic Turbulence", Proc. Cambridge Phil. Soc., Vol. 43, pt. 4, February, 1947, pp. 560-570.

42. Hot-Wire Measurements of Air Velocity, Direction, and Temperature, Flow Corporation Bulletin, No. 94B, Cambridge, Massachusetts, 1964.

43. Taylor, G.I., "Statistical Theory of Turbulence III-Distribution of Dissipation of Energy in a Pipe Over Its Cross-Section", Proceedings of the Royal Society of London, ser. A, Vol. 151, No. 873, Sept. 2, 1935, pp. 455-464.

44. Anonymous, X-Wire Turbulence Measurements, Flow Corporation Bulletin No. 68, Cambridge, Massachusetts, 1962.

APPENDIX A

HOT-WIRE ANEMOMETER VELOCITY CALIBRATION

HOT-WIRE ANEMOMETER VELOCITY CALIBRATION

The velocity profile data listed in this report were obtained with a pitot tube (O.D. = 0.125 in.) and the Flow Corporation Model MM-3 Micromanometer, which has a capability of measuring a Δh of 0.0001 inches of fluid.

Although pitot tube measurements were made at a minimum y value of 0.0625 inches, the hot-wire anemometer velocity data were used for the y = 0.01 to 0.125 inch range.

Therefore, calibration coefficients were obtained for the hot-wire anemometer from the pitot tube measurements for values of y greater than 0.125 inches. Since the coefficients were variable, a straight line was drawn through the points by using the least-squares method. Extrapolated values for the I_v/I_o values in the region of y less than 0.125 inch were read from Figure A.1 for the hard plate, and from Figure A.2 for two sets of velocity data for the compliant plate and one set of hard plate data. Unfortunately, all of the velocity data were not obtained with one wire due to probe A damage after part of the hard plate data were complete. However, excellent agreement was found to exist between the two wire current values. The least-squares technique provided consistency in placing a line through the four sets of data.

The hot-wire anemometer velocity equations and pitot tube equations were similar to those used previously by Walters [18] and Flow Corporation Bulletin No. 25, Cambridge, Massachusetts.

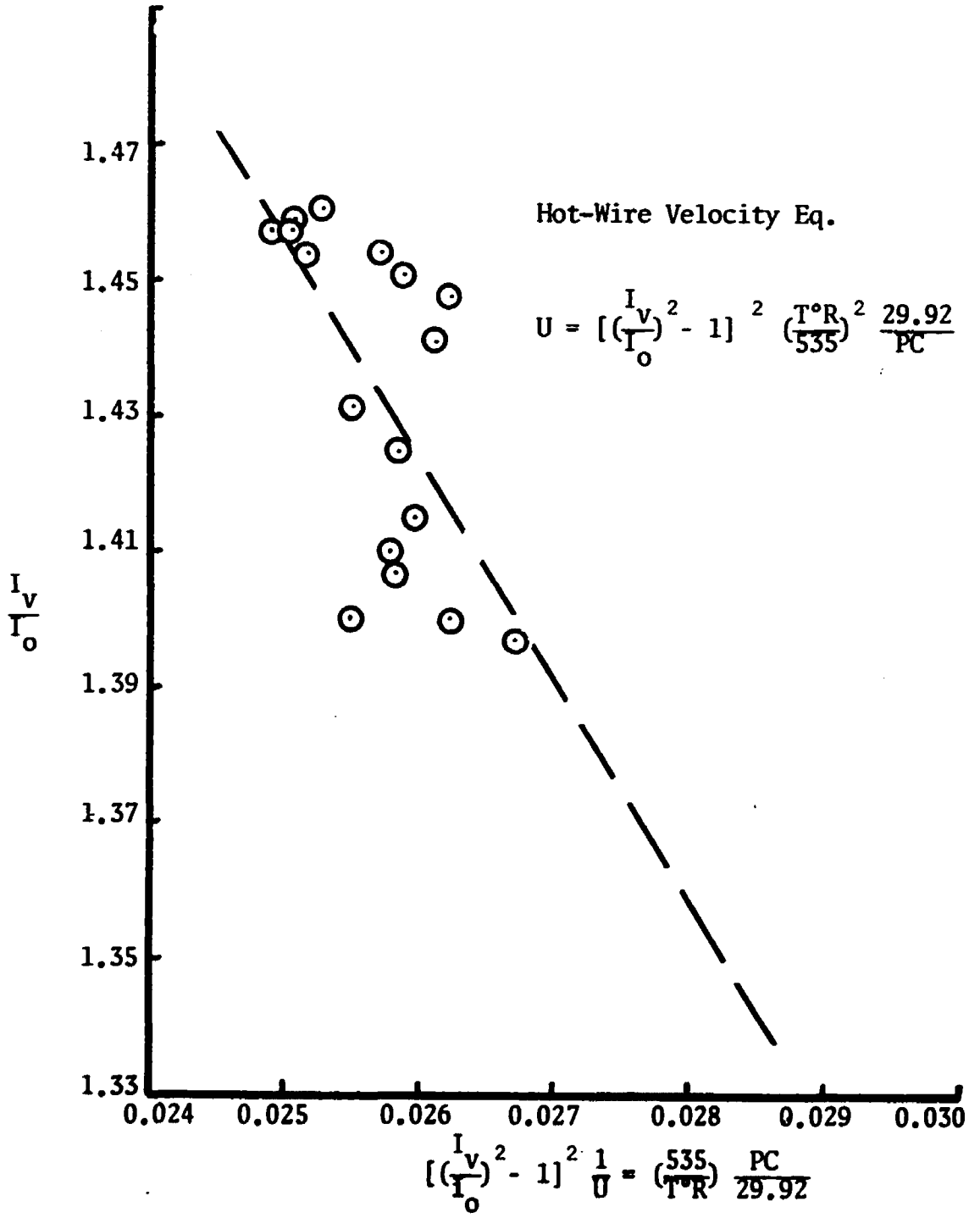

Figure A.1. Hot-wire velocity coefficients for probe A.

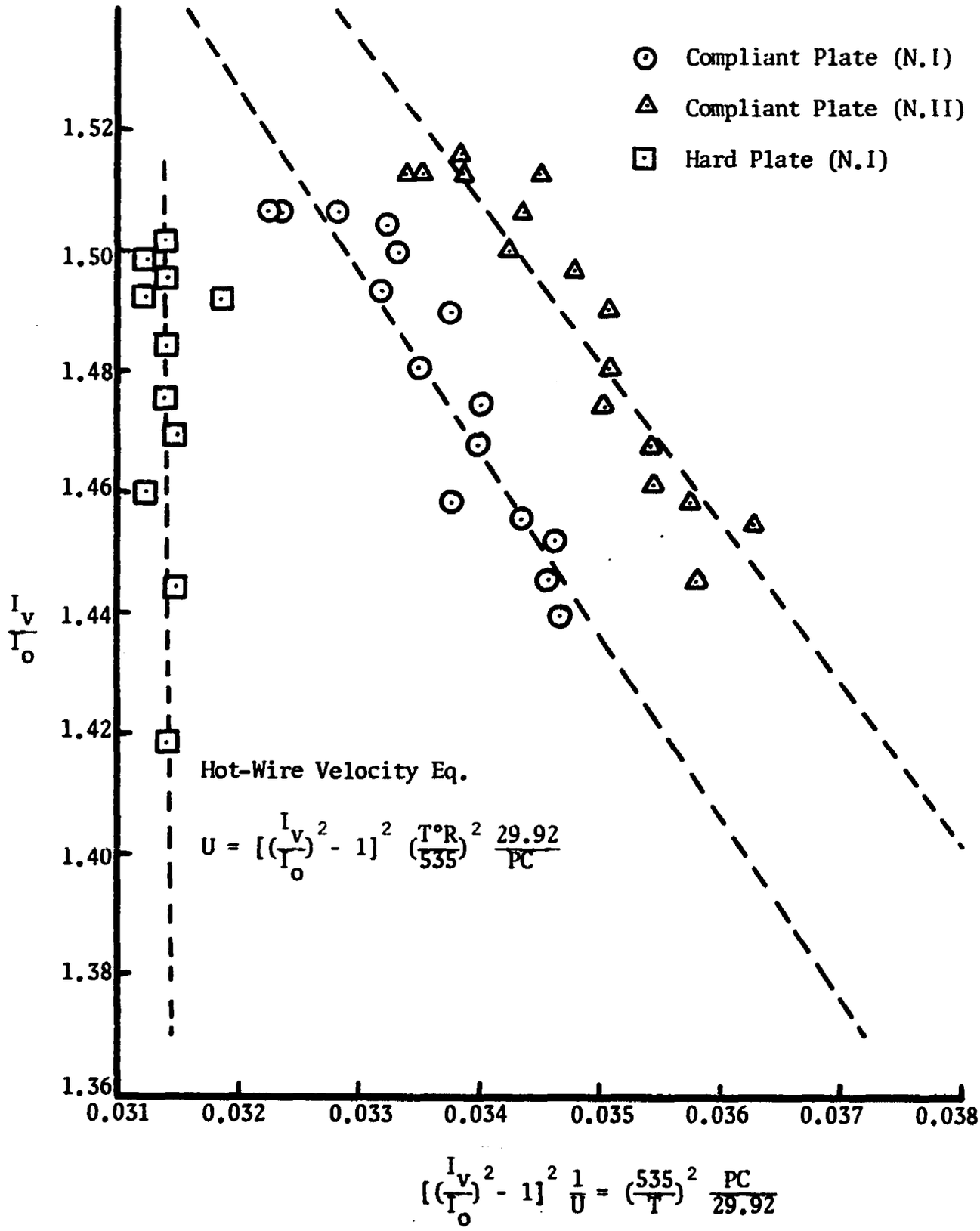

Figure A.2. Hot-wire velocity coefficients for probe B.

APPENDIX B

METHOD FOR SPECTRAL DENSITY ANALYSIS

METHOD FOR SPECTRAL DENSITY ANALYSIS

The spectral distribution or spectral density analysis of the turbulent velocity components was measured with the General Radio Type 1564-A Sound and Vibration Analyzer. The input of the analyzer was connected to the output of the Flow Corporation, Model CCB, Hot-Wire Anemometer System. The output signal of the analyzer was measured with the Flow Corporation Model 12A1 Random Signal Voltmeter for a true rms reading. To check the continuous frequency range from 2.5 cps to 25000 cps, the output signal of the 1564-A analyzer was recorded on the General Radio Type 1521-A Graphic Level Recorder using 1521-9493 chart paper. Only the frequency range from 0-7000 cps was of practical interest, since the anemometer output utilized a 7KC low pass filter.

To obtain a sufficient time average of the 1564-A analyzer output, the signal had to be measured by the 12A1 voltmeter and observed for a period of time not less than one minute. Since, for practical reasons, the continuous frequency range could not be measured by using the 12A1 voltmeter, the range was divided into eighteen different frequency levels from 3.175 cps to 7000 cps, as illustrated on the data sheet, form 5A, in Appendix E.

The required meter readings for finding the percent of energy or turbulence at each frequency level were derived from the following equations. Since

$$\frac{\sqrt{\overline{u^2}}}{U} = \frac{4i}{I_v\left[1 - \left(\frac{I_o}{I_v}\right)^2\right]} \sqrt{\frac{M^2_{n+v} - M^2_n}{M^2_{n+v+s} - M^2_{n+v}}} \qquad \text{(B.1)}$$

is the equation for calculating total turbulence, a percent of turbulence was calculated by

$$\frac{\sqrt{\overline{(u^2)_f}}}{\sqrt{\overline{(u^2)_{total}}}} = \sqrt{\frac{(M^2_{n+v} - M^2_n)_f}{(M^2_{n+v} - M^2_n)_{total}}} \qquad \text{(B.2)}$$

so that the spectra of M^2_{n+v} and M^2_n were required.

To obtain the total turbulence rms meter readings of M_{n+v} and M_n, the 1564-A Analyzer bandwidth control was set on the "All Pass" position. For the $(M^2_{n+v} - M^2_n)_f$ readings the bandwidth selector was set on the 1/10 octave position. The 1/10 octave selection had a constant percentage bandwidth (≈ 7%) such that its bandwidth increased in direct proportion to the increase in the frequency to which the bandwidth was tuned [39].

To calculate a true spectrum level the data were divided by 0.07f, as shown in data sheet form 5A in Appendix E. This met the requirements of the definition of the spectrum level of a signal which Keast [40] stated as, "The spectrum level of a specified signal at a particular frequency is the level of that part of the signal contained within a band one cycle per second wide, centered at the particular frequency."

Using the Hewlett-Packard Model 200AB Audio Oscillator as a signal generator, input and output values for the General Radio 1564-A Analyzer were recorded at the "All Pass" bandwidth position and at

several frequencies from 3.175 to 700 cps for the 1/10 octave position. A constant gain factor was measured for all positions.

M_{n+v} and M_n, for continuous range of frequencies, were recorded by the graphic level recorder for the different y positions of both hard and compliant plate. This was a check on the validity of choosing the 18 different frequencies as a true sampling of data. This insured that irregularities over the entire spectra of turbulence were not deleted from consideration.

APPENDIX C

DERIVATION OF EQUATIONS AND TECHNIQUES USED IN OBTAINING THE TIME DERIVATIVE

DERIVATION OF EQUATIONS AND TECHNIQUES USED IN OBTAINING THE TIME DERIVATIVE

In order to obtain the spatial derivative of the turbulent velocity components u, v and w, in the streamwise direction of flow (x-direction), it is necessary to measure these instantaneous turbulent velocity components at two x-locations simultaneously. This would involve the use of two hot-wire anemometer systems. Separating two probes by some x-interval, while maintaining constant y and z coordinates, would place one probe in the wake region of the other due to the necessary small Δx for proper signal correlation.

Townsend [41], as well as later investigators, has made use of the temporal derivative of the signal from a single hot-wire anemometer system to obtain the spatial derivative in the streamwise direction (x-direction). Making the common assumption that the turbulent velocity components are small with respect to the mean velocity of the stream, the following space-time transformation can be written

$$\frac{\partial u}{\partial x} = -\frac{1}{U}\left(\frac{\partial u}{\partial t}\right) \quad \text{or} \quad \overline{\left(\frac{\partial u}{\partial x}\right)^2} = \frac{1}{U^2}\overline{\left(\frac{\partial u}{\partial t}\right)^2} \tag{C.1}$$

The time derivative can be obtained from a simple resistance-capacitance network, since electrical differentiation depends on the use of the changing current of a capacitor to produce a potential drop in a series resistance proportional to the time derivative of the potential difference across the capacitor.

The equation for the simple RC circuit shown below can be written in two different forms.

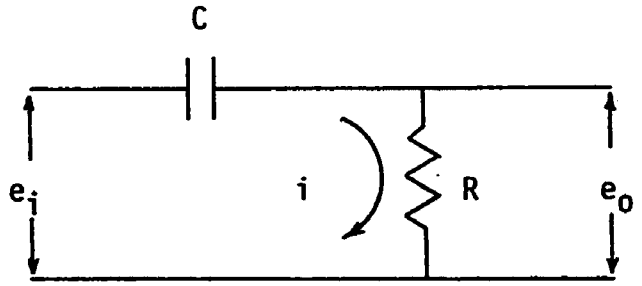

Figure C.1. Simple Differentiation Circuit.

If e_i is the input voltage and q is the charge on the condenser, then

$$e_i = e_R + e_c = R\frac{dq}{dt} + \frac{q}{C} \qquad (C.2)$$

where

$$i = \frac{dq}{dt} = C\frac{de_c}{dt} \qquad (C.3)$$

If $\frac{q}{C} >> R\left(\frac{dq}{dt}\right)$, that is, if the voltage drop e_R across the resistance is small compared with e_i, then one could make the following approximations

$$e_c = \frac{q}{C} \text{ and } R\frac{dq}{dt} = RC\frac{de_i}{dt} = e_o$$

An alternate equation could be written in the following manner, where $\omega = 2\pi f$,

$$e_i = e_o + e_c = Ri - (j/\omega C)i \qquad (C.4)$$

$$e_o/e_i = Ri/i(R - j/\omega C) \qquad (C.5)$$

$$\frac{e_o}{e_i} = \frac{1}{1 - j/\omega RC} = \frac{1}{1 + 1/j\omega RC} \qquad (C.6)$$

$$\frac{e_o}{e_i} = \frac{j\omega RC}{j\omega RC + 1} \qquad (C.7)$$

If $\omega RC << 1$ then the necessary differentiation conditions listed above will hold.

Townsend [41] stated that the required amplification for differentiation can be obtained if $RC = \tau$, where τ is the time constant for the hot wire. τ can be computed from [42]

$$\tau = \frac{1}{2\pi n_c} \qquad (C.8)$$

where n_c is the characteristic frequency of the wire. The time constant is the time required for the wire to complete 63.2% of its adjustment to a sudden step change in velocity. The characteristic frequency depicts a "transition" region. Above this frequency the hot-wire signal decreases linearly with frequency. The characteristic frequency is determined by the approximate formula

$$n_c \simeq \left[\frac{0.04}{100d}\right]^2 \frac{(100I_v)^2}{R/R_E - 1} \text{ cps} \qquad (C.9)$$

where d is the wire diameter in inches and I_v the wire current in amperes.

For the hot wire used, $R/R_E = 1.3$, $d = 0.00035$in., $I_v \simeq 110$ ma. Therefore,

$$n_c \simeq \left(\frac{0.04}{0.035}\right)^2 \frac{(11.0)^2}{0.3} \text{ cps} = 526 \text{ cps}$$

$$\tau(I_v = 110\text{ma}) = 1/2\pi(526\text{cps}) = 0.000303$$

$$\tau(I_v = 100\text{ma}) = 1/2\pi(435) = 0.000367$$

For the hot-wire current range of I_v = 100ma to 110ma, the hot-

wire time constant varies from τ = 0.000303 sec. to 0.000367 sec., which corresponds to the RC range.

Different combinations of R and C are plotted in Figure C.2. As can be seen the RC values that match the wire time constant have a very limited linear frequency response, i.e., 0 to 300 cps.

When the value of $RC \approx 3.3(10)^{-4}$ was used in the differentiation circuit, insufficient amplitude was obtained.

A value of $RC = 3.3(10)^{-5}$ was selected, since this would satisfy the condition of $\omega RC << 1$ or would permit a wider frequency range. The calibration plot of $RC = 3.3(10)^{-5}$ is shown in Figure C.2. As illustrated, the response is linear to approximately 2500 cps.

The differentiation circuit was calibrated by connecting a Hewlett-Packard Model 200AB Audio Oscillator to the input. The input and output voltages were measured on the Flow Corporation 12A1 random signal voltmeter and a Hewlett-Packard Model 3440A Digital Voltmeter.

The quantity $\overline{(de/dt)^2}$ was used for the ordinate of Figure C.2, since this is the desired form in equation (C.1).

From the basic compensated hot-wire turbulence equation, an equation can be derived for the derivative ofthe turbulent velocity component in the streamwise direction with respect to time.

Equation (42) in Flow Corporation Bulletin No. 94b [42] can be written as follows,

$$\frac{c}{C} = -\frac{4i}{I_v}\,\frac{1}{1-(I_o/I_v)^2}\left(\frac{e_f}{e_s}\right) \qquad (C.10)$$

where i is the square wave current, and the amplifier output due to the square wave is

$$e_s = \frac{K\,2i^2\,IR}{A_1 \bar{f}\,\bar{x} - I^2} \qquad (C.11)$$

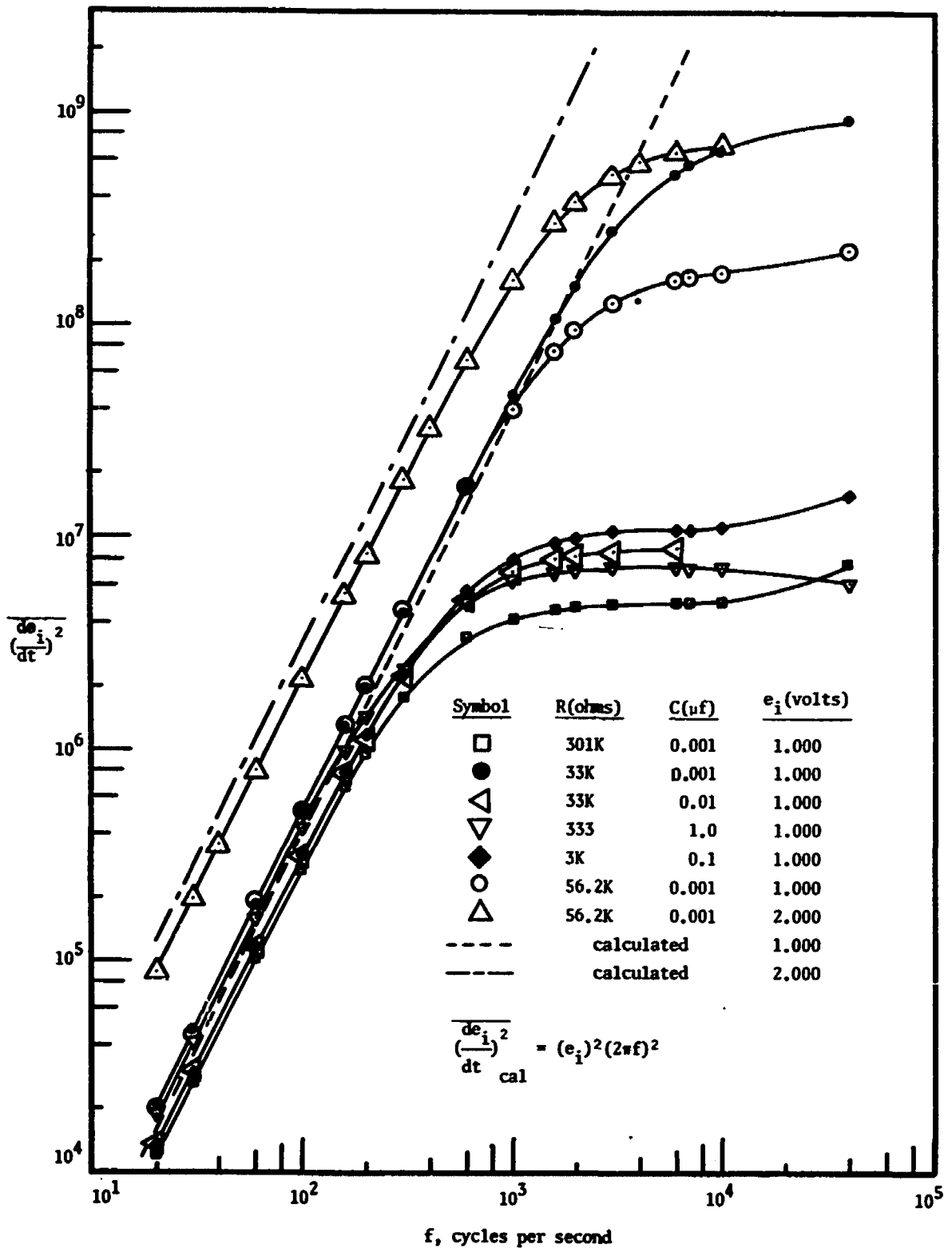

Figure C.2. Calibration of differential circuit.

and $I, K, R, i, A_1, \bar{f}, \bar{x} \neq f(t)$

Let

$$Z = \frac{4i}{I_v[1-(I_o/I_v)^2]} \tag{C.12}$$

Then, taking the time derivative of equation (C.10)

$$\frac{dc}{dt}/C' = -Z\left[\frac{1}{e_s}\frac{de_f}{dt} + e_f\frac{d(e_s^{-1})}{dt}\right] \tag{C.13}$$

where

$$\frac{de_s}{dt} = 0$$

$$\frac{\overline{(\frac{dc}{dt})^2}}{(C')^2} = \frac{(Z)^2}{(e_s)^2}\overline{(\frac{de_f}{dt})^2} \tag{C.14}$$

Now, let

$$M'_{n+v} = K_v K_2 \sqrt{\overline{\left[\frac{d(e_f+e_n)}{dt}\right]^2}} \qquad \text{(a)}$$

$$M'_n = K_v K_2 \sqrt{\overline{(\frac{de_n}{dt})^2}} \qquad \text{(b)}$$

$$M_n = K_v \sqrt{\overline{(e_n)^2}} \qquad \text{(c)} \qquad \text{(C.15)}$$

$$M_{n+v} = K_v \sqrt{\overline{(e_f+e_n)^2}} \qquad \text{(d)}$$

$$M_{n+v+s} = K_v \sqrt{\overline{(e_s+e_f+e_n)^2}} \qquad \text{(e)}$$

K_v is the amplifier gain while K_2 is the gain of the differentiating circuit.

Equations (C.15a) and (C.15b) can be rewritten in the following form

$$\overline{\left(\frac{de_f}{dt}\right)^2} + 2\overline{\left(\frac{de_f}{dt}\right)\left(\frac{de_n}{dt}\right)} + \overline{\left(\frac{de_n}{dt}\right)^2} = \frac{(M'_{n+v})^2}{(K_v K_2)^2} \tag{C.16a}$$

and

$$\overline{\left(\frac{de_n}{dt}\right)^2} = \frac{(M_n)^2}{(K_v K_2)^2} \tag{C.16b}$$

Second term on left side of equation (C.16a) is zero due to lack of correlation of e_f and e_n where e_n is the noise of the circuit and $\bar{e}_f = 0$.

Combining equations (C.16a) and (C.16b)

$$\overline{\left(\frac{de_f}{dt}\right)^2} = \frac{(M'_{n+v})^2 - (M'_n)^2}{(K_v K_2)^2} \tag{C.17}$$

So that equation (C.14) can be stated in terms of the meter readings,

$$\frac{\sqrt{\overline{\left(\frac{dc}{dt}\right)^2}}}{C'} = \frac{Z}{K_2}\sqrt{\frac{(M'_{n+v})^2 - (M'_n)^2}{M^2_{n+v+s} - M^2_{n+v}}} \tag{C.18}$$

or

$$\frac{\sqrt{\overline{\left(\frac{du}{dt}\right)^2}}}{U} = \frac{4i}{I_v\left[1-\left(\frac{I_o}{I_v}\right)^2\right]}\,\frac{1}{K_2}\sqrt{\frac{(M'_{n+v})^2 - (M'_n)^2}{M^2_{n+v+s} - M^2_{n+v}}} \tag{C.19}$$

The value of $RC \simeq K_2 = 3.7(10)^{-5}$ was obtained from a calibration of the differentiation circuit.

Equation (C.19) is the final equation for the time derivative

of the streamwise turbulent velocity component. This equation dictates that only the hot-wire signal plus noise reading and the noise reading alone need be obtained from the differentiation circuit output.

To obtain the time derivatives of the transverse turbulent velocity components normal and parallel to the plate, y and z respectively, the X-array wire probe arrangement has to be employed for the appropriate plane. The necessary equations can be derived from basic hot-wire analysis for the X-array arrangement.

Consider the general coordinate system with axis x_1 and x_2 as illustrated.

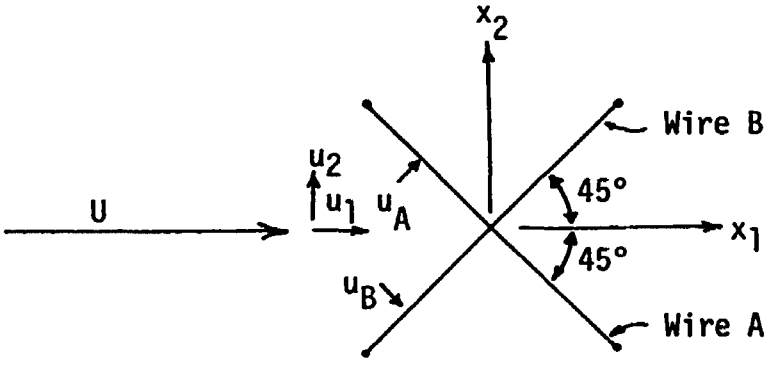

Figure C.3. X-array Hot-Wire Arrangement.

The u_1 and u_2 velocity components can be written in terms of u_A and u_B.

$$u_1 = \frac{u_A}{\sqrt{2}} + \frac{u_B}{\sqrt{2}} \; ; \; u_2 = \frac{u_A}{\sqrt{2}} - \frac{u_B}{\sqrt{2}} \qquad \text{(C.20)}$$

The time derivatives of which are

$$du_1/dt = [(du_A/dt) + (du_B/dt)]/\sqrt{2} \qquad \text{(C.21a)}$$

$$du_2/dt = [(du_A/dt) - (du_B/dt)]/\sqrt{2} \qquad (C.21b)$$

Squaring and taking the time average

$$\overline{(u_{1,t})^2} = 1/2[\overline{(u_{A,t})^2} + 2\,\overline{u_{A,t}u_{B,t}} + \overline{(u_{B,t})^2}] \qquad (C.22a)$$

$$\overline{(u_{2,t})^2} = 1/2[\overline{(u_{A,t})^2} - 2\,\overline{u_{A,t}u_{B,t}} + \overline{(u_{B,t})^2}] \qquad (C.22b)$$

Equation (C.22b) can be written in terms of the Cartesian coordinate system set up for the present experiments, so that the components are

$$\overline{(du/dt)^2} = 1/2[\overline{(u_{A,t})^2} + 2\,\overline{u_{A,t}u_{B,t}} + \overline{(u_{B,t})^2}] \qquad (C.23)$$

$$\overline{(dv/dt)^2} = 1/2[\overline{(u_{A,t})^2} - 2\,\overline{u_{A,t}u_{B,t}} + \overline{(u_{B,t})^2}]_{xy\ plane} \qquad (C.24)$$

$$\overline{(dw/dt)^2} = 1/2[\overline{(u_{A,t})^2} - 2\,\overline{u_{A,t}u_{B,t}} + \overline{(u_{B,t})^2}]_{xz\ plane} \qquad (C.25)$$

$u_{A,t}$ and $u_{B,t}$ can be written in terms of the rms voltmeter readings, so that

$$M'_{A+B} = K_v K_2 \sqrt{\overline{[K_G K_S K(u_{A,t} + u_{B,t}) + e_{n,t}]^2}}$$

$$M'_{A-B} = K_v K_2 \sqrt{\overline{[K_G K_S K(u_{A,t} - u_{B,t}) + e_{n,t}]^2}} \qquad (C.26)$$

$$M'_n = K_v K_2 \sqrt{\overline{(e_{n,t})^2}}$$

or rearranging, where $\overline{(u_{A,t} + u_{B,t})\, e_{n,t}} = 0$

$$\overline{(u_{A,t})^2} + 2\,\overline{u_{A,t}u_{B,t}} + \overline{(u_{B,t})^2} = \frac{(M'_{A+B})^2 - (M'_n)^2}{(K_v K_G K K_S K_2)^2} \qquad (C.27)$$

$$\overline{(u_{A,t})^2} - 2\,\overline{u_{A,t}u_{B,t}} + \overline{(u_{B,t})^2} = \frac{(M'_{A-B})^2 - (M'_n)^2}{(K_v K_G K K_S K_2)^2} \qquad (C.28)$$

Equations (C.24) and (C.25) can be denoted in terms of equation (C.23)

$$\overline{(dv/dt)^2} = \overline{(du/dt)^2}\,\frac{\overline{(u_{A,t})^2} - 2\,\overline{u_{A,t}u_{B,t}} + \overline{(u_{B,t})^2}}{\overline{(u_{A,t})^2} + 2\,\overline{u_{A,t}u_{B,t}} + \overline{(u_{B,t})^2}} \qquad (C.29)$$

xy plane

$$\overline{(dw/dt)^2} = \overline{(du/dt)^2}\,\frac{\overline{(u_{A,t})^2} - 2\,\overline{u_{A,t}u_{B,t}} + \overline{(u_{B,t})^2}}{\overline{(u_{A,t})^2} + 2\,\overline{u_{A,t}u_{B,t}} + \overline{(u_{B,t})^2}} \qquad (C.30)$$

xz plane

Using equations (C.27) and (C.28) in equations (C.29) and (C.30) the final form of the time derivatives can be obtained.

$$\overline{(dv/dt)^2} = \overline{(du/dt)^2}\left[\frac{(M'_{A-B})^2 - (M'_n)^2}{(M'_{A+B})^2 - (M'_n)^2}\right]_{xy\ plane} \qquad (C.31)$$

$$\overline{(dw/dt)^2} = \overline{(du/dt)^2}\left[\frac{(M'_{A-B})^2 - (M'_n)^2}{(M'_{A+B})^2 - (M'_n)^2}\right]_{xz\ plane} \qquad (C.32)$$

Therefore, by obtaining the rms meter readings, M'_{A+B}, M'_{A-B} and M'_n from the output of the differentiation circuit with the xy and the xz X-array probes, the respective $\overline{(dv/dt)^2}$ and $\overline{(dw/dt)^2}$ can be found from the single wire data and equation (C.19). A single wire $\overline{(du/dt)^2}$ measurement is illustrated on sample data sheet Form 2B in Appendix E.

A sample X-array measurement for the xy plane is illustrated on data sheet 3B in Appendix E to obtain the spatial derivative of the

normal transverse velocity (v) from the temporal derivative in equation (C.31).

The equations (C.31) and (C.32) follow the same form for the turbulent velocity component, without the time derivative, as given by Gessner in [31].

APPENDIX D

METHOD OF CORRELATION COEFFICIENT MEASUREMENT FOR $\overline{(du/dy)^2}$ and $\overline{(du/dz)^2}$

METHOD OF CORRELATION COEFFICIENT MEASUREMENT FOR $\overline{(du/dy)^2}$ AND $\overline{(du/dz)^2}$

The dissipation derivatives were calcualted from the relations given by Taylor [43].

$$\overline{\left(\frac{\partial u}{\partial y}\right)^2} = \frac{(1-R_y)\ 2\overline{u^2}}{(\Delta y)^2} \qquad \text{for } \Delta y \to 0 \qquad (D.1)$$

and

$$\overline{\left(\frac{\partial u}{\partial z}\right)^2} = \frac{(1-R_z)\ 2\overline{u^2}}{(\Delta z)^2} \qquad \text{for } \Delta z \to 0 \qquad (D.2)$$

R_y and R_z are the correlation coefficients obtained by comparing the $\overline{u^2}$ values at two different locations in the flow, separated by small intervals, Δy and Δz, respectively.

The relations for R_y and R_z were derived from the work presented in a technical memorandum [44] from Flow Corporation. The relation for R_y, which is identical to R_z except for denoting probe locations, is given on data sheet form 3A in Appendix E.

The correlation coefficients were measured with two single wire probes attached to the two-channel hot-wire anemometer system. One probe was supported at an angle of 30° from the vertical probe so that the probe tips could be placed in a position for small intervals of separation as shown in Figure D.1.

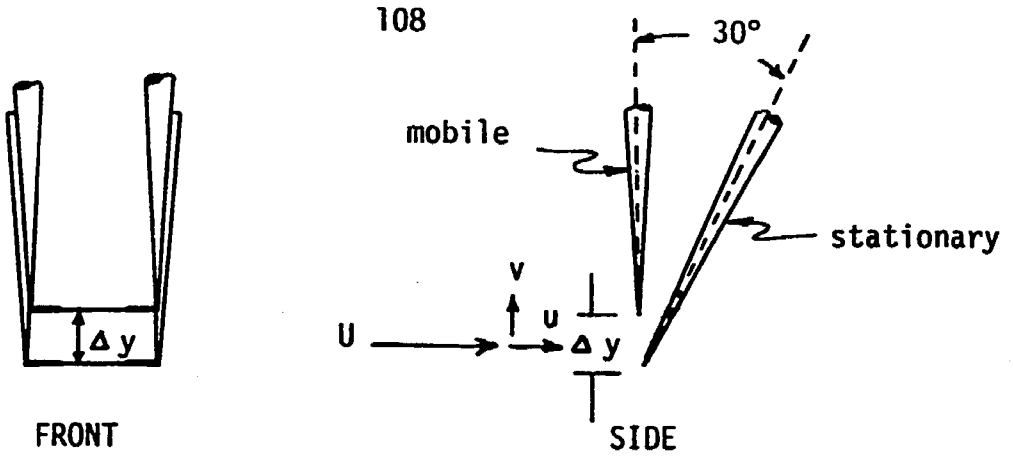

Figure D.1. Front and Side View of Δy Geometry

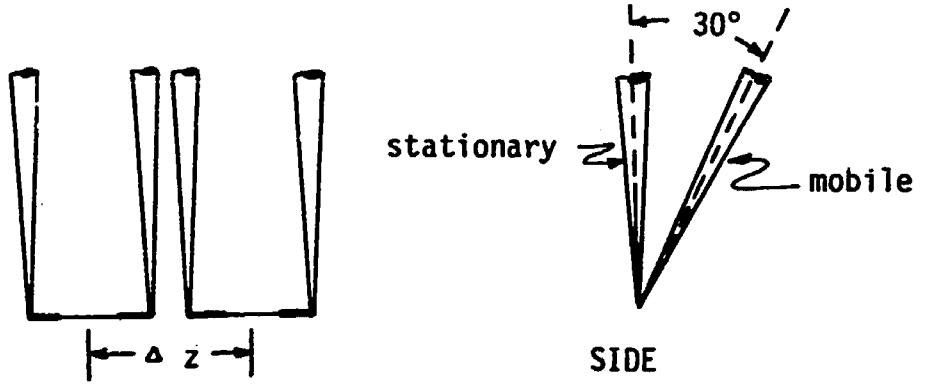

Figure D.2. Front and Side View of Δz Geometry

As illustrated, for the R_y measurements, the slanted probe was used as the stationary probe and the vertical probe was used to vary the interval, Δy. Since the vertical probe could only be positioned normal to the plate and not transverse, the slanted probe was moved for varying Δz during R_z measurements. From the geometry of the system, the practical minimum values of Δy and Δz were 0.015 inches and 0.0625 inches, respectively. Good agreement was found to exist between the two wire current values and the individual turbulence readings of the vertical and slant probes.

APPENDIX E

DATA SHEETS

SINGLE WIRE TURBULENCE AND $(\frac{du}{dt})$ MEASUREMENTS — Data Sheet

OURI Project No. 1499 — Form 2B — Date 8/5/68

Skin Thickness (in.) 0.001 — Sandpaper Installed - (Yes) No

Pressure Gradient - 0

Fluid Substrate-Density = Polyurethane (3/16")

Ambient Pressure (in. Hg) 29.00

Number Screens 1 2 (3) — Square Wave Ampl. 1 (4)

Attenuation (4) 16 — Ambient Temp. 81 °F

X_o = 10.5' — Y = 0.50"

$I_o = \frac{(312)}{4} = 78$; $I_v = \frac{(457)}{4} = 114.25$; B.N. = 146.5; Vel. = 38fps = U

$M_n = 2.5$ $M_n^2 = 6.25$

$M_{n+v} = 76.5$ $M_{n+v}^2 = 5852$ $A = M_{n+v}^2 - M_n^2 = 5846$

$M_{n+v+s} = 403$ $M_{n+v+s}^2 = 162409$ $B = M_{n+v+s}^2 - M_{n+v}^2 = 156557$

$4^* \times 4i = \frac{10.0}{1 + \frac{B.N.(6.2)}{1600}} = 25.6$ $I = \frac{(4)(4i)}{I_v\left[1 - (\frac{I_o}{I_v})^2\right]}\sqrt{\frac{A}{B}}$

U_1 = 50fps $\frac{\sqrt{\overline{u^2}}}{U} = I = .419 \times .1932 = .0810$

$M_n' = 0.15$ $(M_n')^2 = 0.0225$ $A' = (M_{n+v}')^2 - (M_n')^2 = 30.01$

$M_{n+v}' = 5.48$ $(M_{n+v}')^2 = 30.03$

R (ohms) = 33000 $RC_{meas} = 3.7(10)^{-5}$

C (farads) = 10 $(RC)^{-1}_{meas} = 2.7(10)^4$

$$\frac{\overline{(\frac{du}{dt})^2}}{U} = I' = \frac{4i}{Iv}\frac{(RC)^{-1}}{\left[1 - (\frac{I_o}{I_v})^2\right]}\sqrt{\frac{A'}{B}} = 1.131(10)^4 \times 0.01382 = 156.3$$

$$\overline{(\frac{du}{dx})^2} = \frac{\overline{(\frac{du}{dt})^2}}{U^2} = (I')^2 = 2.45(10)^4; \quad \frac{\delta^2}{U_1^2}\overline{(\frac{du}{dx})^2} = 2.5(10)^{-5}(I')^2 = 0.611$$

*Multiply square wave current equation by 4 when square wave amplitude switch set on (4).

CORRELATION COEFFICIENT MEASUREMENTS — Data Sheet
OURI Project No. 1499 — Form 3A — Date 8/11/68

Skin Thickness (in.) 0.001 — Sandpaper Installed - (Yes) No
Pressure Gradient - 0
Fluid Substrate Density = Polyurethane (3/16")
Ambient Pressure (in. Hg) 28.98
Number Screens 3 — Square Wave Ampl. 1 ④
Attenuator 16 — Ambient Temp. 80 °F
Δz = - Δy = 0.0015 in. y = 0.39 in

Wire #1 $I_o = \frac{(312)}{4} = 78$ma; $I_v = \frac{(461)}{4} = 115.25$ma; B.N. = 119

Wire #2 $I_o = \frac{(\ -\ )}{4} =$ -; $I_v = \frac{(461)}{4} = 115.25$ma; B.N. = -

M_a = 15.9mv	M_a^2 = 252.8	$M_{a+b}^2 - M_n^2$ = 909.0	$= E_3^2$
M_b = 17.0mv	M_b^2 = 289.0	$M_{a-b}^2 - M_n^2$ = 22.0	$= E_4^2$
M_{a+b} = 30.2mv	M_{a+b}^2 = 912.04	$M_a^2 - M_n^2$ = 249.8	$= E_1^2$
M_{a-b} = 5.0mv	M_{a-b}^2 = 25.0	$M_b^2 - M_n^2$ = 286.0	$= E_2^2$
M_n = 1.7mv	M_n^2 = 2.89		

$$R_{y \text{ or } z} = \frac{C_1\ C_2}{\sqrt{C_1^2}\ \sqrt{C_2^2}} = 1/2\ \frac{(E_1^2 + E_2^2)(E_3^2 - E_4^2)}{(E_3^2 + E_4^2)(E_1 E_2)} = 0.95$$

$$\frac{\delta^2}{2U_\infty^2}\ \overline{\left(\frac{du}{dy}\right)^2} = \frac{(1 - R_{12})(\bar{u}^2)(\delta^2)}{(\Delta y)^2\ U_1^2} = 6.55$$

$$\frac{\delta^2}{2U_\infty^2}\ \overline{\left(\frac{du}{dz}\right)^2} = \frac{(1 - R_{13})(\bar{u}^2)\ \delta^2}{(\Delta z)^2\ U_1^2} = -$$

TURBULENCE & REYNOLDS STRESS MEASUREMENTS — Data Sheet
OURI Project No. 1499 — Form 3B — Date 8/4/68

Skin Thickness (in.) 0.001 — Sandpaper Installed - (Yes) No
Pressure Gradient - 0
Fluid Substrate Density = Polyurethane (3/16")
Ambient Pressure (in. Hg 28.88
Number Screens 3 — Square Wave Ampl. 1 ④
Attenuator 4 16 — Ambient Temp. 82 °F
Vel.=38fps X_o=10.5' y=0.50"

Wire #1 $I_o = \frac{(312)}{4} = 78$; $I_v = \frac{(397)}{4} = 99.25$; B.N. = 161; Vel. = 38fps

Wire #2 $I_o = \frac{-}{4} = -$; $I_v = \frac{(397)}{4} = 99.25$; B.N. = -;

M'_{a+b}= 15.2mv — $(M'_{a+b})^2$= 231.04 — $M'^2_{a+b} - M'^2_n$= 230.95

M'_{a-b}= 14.2mv — $(M'_{a-b})^2$= 201.64 — $M'^2_{a-b} - M'^2_n$= 201.55

M_a= 17.2mv — M_a^2= 295.84 — $M_a^2 - M_n^2$= 291.8 = E_1^2

M_b= 11.3mv — M_b^2= 127.69 — $M_b^2 - M_n^2$= 123.7 = E_2^2

M_{a+b}= 23.2mv — M_{a+b}^2= 583.24 — $M_{a+b}^2 - M_n^2$= 534.2 = E_3^2

M_{a-b}= 13.2mv — M_{a-b}^2= 174.24 — $M_{a-b}^2 - M_n^2$= 170.2 = E_4^2

M_n= 2mv — M_n^2= 4 — M'_n= 0.3 — M'^2_n= 0.09

$$\frac{\overline{u_3^2}}{U_1^2} \text{ or } \frac{\overline{u_2^2}}{U_1^2} = \frac{\overline{u_1^2}}{U_1^2}\left[\frac{M_{a-b}^2 - M_n^2}{M_{a+b}^2 - M_n^2}\right] = (0.0618^2)(0.3185) = 0.001218 \qquad \sqrt{\overline{v^2}}/U_1 = 0.0349$$

$$\frac{\overline{u_1 u_2}}{U_1^2} = \frac{\overline{u_1^2}}{U_1^2}\left[\frac{(M_a^2 - M_b^2)(M_{a+b}^2 + M_{a-b}^2 - 2M_n^2)}{(M_a^2 - M_b^2 - 2M_n^2)(M_{a+b}^2 - M_n^2)}\right] = 0.00200$$

$$\frac{\delta^2}{2U_1^2}\overline{\left[\frac{d(v \text{ or } w)}{dx}\right]^2} = \frac{\delta^2}{2U_1^2}\left(\overline{\frac{du}{dx}}\right)^2\left[\frac{M'^2_{a-b} - M'^2_n}{M'^2_{a+b} - M'^2_n}\right] = (0.611)\left(\frac{0.87}{2}\right) = 0.266$$

Compliant or Hard Plate SPECTRUM OF TURBULENCE Data Sheet Form 5A

y=_____ y/δ=_____ Date_____

I_o = /4=_____ Substrate_____ Skin_____

I_v = /4=_____ M_{n+v+s} = M^2_{n+v+s} =

C.F.= B.N.= All-Pass M_{n+v} = M^2_{n+v} =

T= °F Rel.Hum.= % M_n = M^2_n =

P= in. Hg. $Z_{A.P.} = M^2_{n+v} - M^2_n$ =

1/10 Octave 1/3 Octave Band Level=_____

	f	A	B	C	D	E	F	G	H
#	freq.	M_{n+v}	M^2_{n+v}	M_n	M^2_n	B-D	$\frac{E}{Z_{A.P.}}$	$\sqrt{F}$	$\frac{G}{.07f}$
1	3.175								
2	5								
3	8								
4	12.6								
5	20								
6	31.75								
7	50								
8	80								
9	126								
10	200								
11	317.5								
12	500								
13	800								
14	1260								
15	2000								
16	3175								
17	5000								
18	7000								

APPENDIX F

LIST OF INSTRUMENTS USED

LIST OF INSTRUMENTS USED

The following instruments were used for the work reported herein:

1. Bruel and Kjaer Model 161 Probability Density Analyzer
2. Flow Corporation Model CCB Two Channel Hot-Wire Anemometer System
   a. Model HWB-3 Hot-Wire Anemometer
   b. Model HWI-3 Hot-Wire Sum-Difference Control Unit
   c. Model 12A1 Random Signal Voltmeter
3. Flow Corporation Model MM-3 Micromanometer
4. Fluke Model 931A RMS Differential Voltmeter
5. General Radio Type 1564-A Sound and Vibration Analyzer
6. General Radio Type 1521-B Graphic Level Recorder
7. Hewlett-Packard Model 200AB Audio Oscillator
8. Hewlett-Packard Moseley Model 7005B XY Recorder
9. Hewlett-Packard Model 3440A Digital Voltmeter
10. Tektronix Type 503 Oscilloscope